Università degli Studi di Padova

Department of Industrial Engineering

Master Degree in Materials Engineering

THE EFFECT OF CHROMIUM CONCENTRATION ON THE OXIDATION BEHAVIOUR OF MODEL NICKEL-BASE SUPERALLOYS

Supervisors:

Prof. Franco Bonollo, *Department of Engineering and Managment*

Dr. Howard Stone, *Department of Material Science and Metallurgy, University of Cambridge*

Student:

Francesco Monni

Academic Year 2015/2016

Contents

Compendio **7**

Superleghe a base nickel 7

Procedura sperimentale 8

Risultati 9

Composizione chimica 9

Variazioni di massa 10

Misure di spessori e profondità della penetrazione interna 12

Mappe EDX degli elementi 15

Discussione 18

Variazione di massa 18

Morfologia degli ossidi esterni 19

Morfologia di ossidi interni e strato di impoverimento 19

Conclusioni 21

Introduction **23**

1 Superalloys: microstructure and properties **25**

1.1 Superalloys as high temperature materials 25

1.1.1 Materials for gas turbine engines 25

1.1.2 Nickel as high temperature material 27

1.2 Microstructure of polycrystalline nickel based alloys 29

1.2.1 The γ phase 29

1.2.2 The γ' phase 32

1.2.3 The TCP phases 36

1.3 Turbine disc alloys 37

1.3.1 Criterion I: γ' phase . . . 37
1.3.2 Criterion II: grain size . . . 40
1.3.3 Criterion III: grain boundary elements . . . 41
1.3.4 The Udimet 720Li . . . 42

2 Oxidation of superalloys 43
2.1 External oxidation . . . 43
2.2 Internal oxidation . . . 44
2.2.1 Conditions and mechanism . . . 44
2.2.2 Kinetics . . . 45
2.2.3 Precipitate morphology . . . 46
2.3 Transition from internal to external oxidation . . . 48
2.4 Oxidation of Ni-Cr alloys . . . 51
2.4.1 Transient oxidation . . . 51
2.4.2 Chromium depleted region . . . 52
2.5 Alumina forming alloys . . . 53
2.5.1 Oxidation of Ni-Al alloys . . . 53
2.5.2 Oxidation of Ni-Cr-Al alloys . . . 53
2.6 Alloying with cobalt and titanium . . . 56

3 Experimental procedure 59
3.1 Initial samples preparation and characterization . . . 59
3.2 Isothermal oxidation tests and analysis . . . 60

4 Results 63
4.1 Characterization of the alloys . . . 63
4.2 Mass change per unit area . . . 67
4.3 Outermost oxide scales . . . 68
4.4 Cross sections . . . 71
4.5 External oxide thickness and internal damage penetration . . . 74
4.6 Characterization after oxidation for 42 days . . . 75
4.7 EDX mapping and elements distribution on the cross sections . . . 79
4.8 Chromium depletion layer . . . 83

5 Discussion **89**

5.1 External oxide scale and microstructural evolution 89

5.2 Mass gains per unit area 90

5.3 Classification of the alloys on the oxidation mechanism 91

5.4 Internal damage 92

5.5 Chromium depletion layer 93

6 Conclusions **95**

Compendio

Lo scopo di questo lavoro di tesi è quello di indagare il comportamento ad ossidazione di cinque diversi tipi di superlega a base nickel a 800℃ in aria. Le cinque diverse leghe considerate sono state realizzate prendendo come riferimento la composizione nominale della lega policristalllina Udimet 720Li, ma variando il tenore di Cr tra 10-25 at.%.

Superleghe a base nickel

Le superleghe a base nickel sono materiali ideali per essere impiegati nella realizzazione dei dischi delle turbine dei motori nell'industria aerospaziale in quanto riescono a combinare in maniera eccellente elevate proprietà meccaniche alle alte temperature e buona resistenza ad ossidazione e corrosione. La microstruttura tipica di una lega di questo tipo è composta da una fase γ ricca in nickel che costituisce la matrice metallica e una fase γ' composta da precipitati ricchi in altri elementi. L'entità, la distribuzione e la forma dei grani della fase γ' può essere regolata agendo sulla composizione della lega o prevedendo determinati trattamenti termici al materiale in modo da poter ottenere le proprietà meccaniche desiderate per il pezzo.

Al fine di poter svilupare nuove leghe o migliorare quelle esistenti è perciò di fondamentale importanza conoscere il ruolo che ogni elemento in soluzione gioca in funzione di una determinata proprietà finale che il materiale deve avere. In generale, per quanto riguarda la reistenza ad ossidazione, si è classicamente sempre pensato che tanto più Cr è presente in soluzione e tanto più protettivo sarà lo strato di Cr_2O_3 che si verrà a formare sulla superficie del materiale. D'altrocanto una maggiore concentrazione di Cr favorisce la formazione di fasi intermetalliche, chiamate TCP (topologically close packed), particolarmente dannose per le proprietà meccaniche.

Un elemento solitamente presente in leghe a base nickel è l'alluminio. Questo da un

lato favorisce la formazione di fase γ', dall'altro aiuta la formazione dello strato protettivo di ossido di Cr migliorando la resistenza ad ossidazione. Per un generico sistema Ni-Cr-Al sono stati individuati i tre seguenti modelli di comportamento ad ossidazione: Il processo complessivamente è costituito da quattro fasi:

Tipo I: comportamento caratterizzato dalla formazione di uno strato esterno di NiO e ossidi interni composti da allumina e cromia. E' il caso tipico di leghe contenenti basse concentrazioni sia di Al che di Cr;

Tipo II: ossidazione caratterizzata dalla formazione di uno strato esterno continuo di ossido di Cr e uno starto di ossidi interni a base di allumina. E' tipico di leghe contenenti concentrazioni di Cr superiori al 10 wt.%;

Tipo III: ossidazione caratterizzata dalla formazione di uno strato esterno di allumina continuo. E' tipico dei sistemi aventi elevati tenori di Al, più del 5 wt.%.

Questa classificazione del comportamento ad ossidazione è però modificata nel momento in cui sono presenti ulteriori elementi in lega. La presneza di cobalto promuove la formazione di uno strato esterno di NiO e riduce la resistenza ad ossidazione in quanto favorisce lo scrostamento dell'ossido esterno. Il titanio favorisce la formazione di ossidi interni in quanto agevola la formazione di allumina e ossido di titanio, che si comporta in maniera analoga, pertanto può essere considerato anch'esso nocivo per la resistenza ad ossidazione.

Nello specifico la lega Udimet 720Li è una lega policristallina molto utilizzata per la realizzazione di dischi per le zone soggette ad elevate pressioni nei motori a turbina. E' una lega rinforzata per precipitazione di fase γ', in modo da garantire buone proprietà meccaniche alle elevate temperature, e particolarmente resistente all'ossidazione.

Procedura sperimentale

Per questa ricerca sono state realizzate cinque leghe aventi tenore di Cr pari rispettivamente a 10, 15, 17.5, 20 e 25 at.%. Le cinque leghe sono poi state trattate termicamente così da ottenere una precipitazione fine di fase γ' uniformemente distribuita. Queste sono poi state analizzate al microscopio a scansione elettronica (SEM) sia mediante immag-

ini dovute ad elettroni secondari, così da analizzare la struttura interna, sia mediante spettroscopia EDX (energy dispersive X-ray), per analizzarne la composizione chimica.

at.%	Ni	Co	Cr	Mo	W	Al	Ti
Udimet 720Li	Bal.	15	17.5	2	0.5	5	6

Table 1: Composizione nominale della lega Udimet 720Li utilizzata in questo studio.

Per ogni lega sono stati realizzati 7 campioni di dimensioni pari a 17 x 9 x 1.5 mm i cui angoli sono stati smussati a 45° e le superfici lucidate meccanicamente fino al panno P4000. Successivamente i campioni sono stati puliti in etanolo e ultrasuoni.

I campioni sono poi stati posizionati su crogioli in allumina e introdotti in forno ad 800℃. Questi sono stati successiavamente estratti dal forno dopo 1, 2, 3, 4, 10, 21 e 42 giorni di esposizione in atmosfera ossidante. Dopo ogni estrazione sono stati pesati i campioni, i crogioli e la somma campione + crogiolo. In questo modo è stato possibile calcolare la massa guadagnata dai campioni dopo ossidazione come:

$$\Delta m = \frac{m_f - m_i}{s} \tag{1}$$

Dove m_i e m_f rappresentano le masse dei campioni prima e dopo ossidazione rispettivamente e s è la superficie totale di questi.

I campioni ossidati sono poi stati sezionati a metà rispetto al lato più lungo, inglobati in bachelite conduttiva e lucidati ad una finitura pari a 1μm. Successivamente sono stati analizzati al SEM in modo da ricavare lo sviluppo dello strato di ossido esterno e le variazioni di composizione chimica di questo.

Risultati

Composizione chimica

Dalle misurazioni EDX si sono ricavate le cmposizioni esatte delle cinque leghe create. I valori di composizione sono risultati pari a quelli nominali della lega Udimet720Li con una tolleranza del ±0.6 at.%.

at.%	Ni	Co	Cr	Mo	W	Al	Ti
10 % Cr	Bal.	14.6	10.3	2.17	0.53	5.08	6.48
15 % Cr	Bal.	14.5	15.3	2.22	0.57	5.25	6.49
17.5 % Cr	Bal.	14.6	17.7	2.08	0.59	4.85	6.47
20 % Cr	Bal.	14.7	20.3	2.10	0.49	4.61	6.22
25 % Cr	Bal.	14.4	25.5	2.18	0.56	4.95	6.50

Table 2: Composizione delle cinque leghe studiate in at.%.

Variazioni di massa

Le variazioni di massa dei materiali a seguito dell'ossidazione sono state calcolate e rappresentate graficamente in funzione dell'intervallo di esposizone a 800℃. I campioni con 10 e 15 at.% di Cr hanno mostrato un andamento lineare con valori massimi pari a 9 mg/cm^2 e 6.5 mg/cm^2 dopo 42 giorni di esposizione rispettivamente. I campioni con 17.5 e 20 at.% di Cr hanno msotrato un andamento parabolico e molto simile. La variazione di massa dopo 42 giorni è di circa 2 mg/cm^2 per entrambi. Anche nel caso della lega con il 25 at.% di Cr si è osservata una curva parabolica per l'ossidazione, ma in questo caso la variazione di massa dopo 42 giorni è risultata essere circa doppia rispetto alle leghe con 17.5 e 20 at.% di Cr.

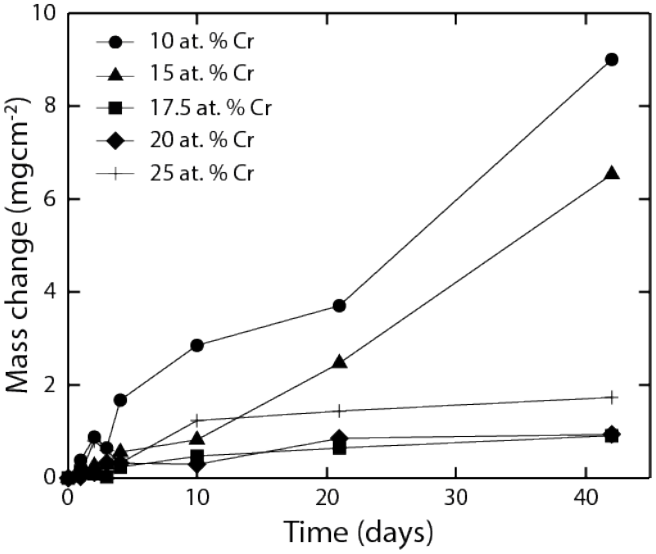

Figure 1: Variazione di massa per unità di superficie nelle cinque leghe studiate dopo ossidazione isoterma a 800℃in aria fino a 42 giorni di esposizione.

Dalle micrografie al SEM con elettroni secondari è stato possibile fare un confronto tra gli strati di ossido che si sono sviluppati nei campioni al variare del tempo di ossidazione (Fig. 2). Si può notare come il materiale con il 10 at.% di Cr abbia formato uno strato continuo di ossido esterno di spessore sempre crescente fino ai 21 giorni di esposizione. Dopo 42 giorni lo strato di ossido esterno per questa lega è risultato essere completamente scrostato e quindi assente sul campione. Nella lega con il 10 at.% di Cr è stato possibile osservare un parziale scrostamento superficiale già a partire dai 10 giorni di esposizione a 800°Cin poi. Anche da un punto di vista strutturale sono presenti delle differenze nello strato di ossido dipendenti dalla durata dell'ossidazione. Risulta netta la variazione della crosta esterna tra 3 e 4 giorni. Dai 4 giorni di esposizione in poi la struttura assume una morfologia a strati caratterizzata da una fascia esterna costituita da grani a crescita verticale, uno strato intermedio compatto al di sotto del quale è presente una regione di crescita di ossidi interni allungati.

La microstruttura della lega con il 15 at.% di Cr è molto simile a quella osservata nel campione con il 10 at.% di Cr. In questo caso però il netto cambio di microstruttura si osserva solo dopo i 10 giorni di ossidazione e lo spessore complessivo dello strato di ossido è generalmente inferiore a quello mostrato dai campioni con il 10 at.% di Cr. La microstruttura dopo il decimo giorno di esposizone presenta anche in questo caso uno strato esterno composto da grani a crescita colonnare ed una regione sottostante caraterizzata da un ossido compatto. La differneza più importante in questo caso è rappresentata dal differente aspetto della regione di ossidazione interna. Rispetto ai campioni con il 10 at.% di Cr, il materiale con il 15 at.% di Cr mostra grani di ossido interno dall'aspetto globulare e meno allungati. Va sottolineato però che il campione ossidato per 4 giorni ha mostrato uno strato di ossido di spessore anomalo e superiore a quello mostrato dal campione ossidato per 10 giorni.

I campioni contenenti il 17.5 at.% di Cr hanno invece mostrato uno strato di ossido esterno sottile fino ai 4 giorni di ossidazione. A partire da 10 giorni in poi si è osservato invece un aumento di spessore nell'ossido esterno e un significativo aumento del danneggiamento interno. La penetrazione di ossido in questo caso infatti è inizialmente poco marcata, ma aumenta significamente di entità tra i 4 e i 10 giorni di ossidazione. Dopo 21 e 42 giorni si osserva un andamento costante del danneggiamento interno che non mostra alcuna ulteriore crescita longitudinale dei grani di ossido.

La lega contenente il 20 at.% di Cr ha mostrato inizialmente, tra 1 e 4 giorni di ossidazione, uno strato sottile e compatto di ossido esterno al di sotto del quale si è osservata la presenza di un ossido interno misto. Dopo 10 giorni di prova e a seguire si è osservato un netto cambio di microstruttura e spessore dello strato di ossido complessivo. Inizialmente la struttura è apparsa simile a quella osservata nella lega contenente il 17.5 at.% di Cr, per tempi di esposizione maggiori invece la morfologia ha mostrato un aspetto differente. Si è osservata la presenza di uno strato esterno composto da grani a crescita colonnare e un ossidazione interna costituita da ossidi di forma globulare aventi lunghezza inferiore a quelli osservati nella lega con il 17.5 at.% di Cr per gli stessi tempi di esposizione.

La lega con il maggior tenore di Cr, 25 at.%, ha sviluppato un ossido apparentemente simile a quello osservato nei campioni contenenti il 20 at.% di Cr, ma lo spessore complessivo dello strato è risultato complessiavmente superiore. Fino a 4 giorni di ossidazione la lega ha mostrato un sottile tìstrato di ossido esterno al di sotto del quale si può distinguere un lieve sviluppo di danneggiamento interno. Dopo 10 giorni la crosta di ossido ha subito un consistente aumento di spessore che si è successivamente mantenuto costante anche dopo 21 e 42 giorni di trattamento ad 800℃. Contemporaneamente all'aumento di spessore si è osservtao anche un cambio di morfologia interna. L'ossido ha complessivamente assunto una struttura a strati composta da una regione esterna a crescita colonnare combinata con un ossido misto sottostante ed infine uno strato di ossido interno appiattito a diretto contatto con il substrato metallico.

Misure di spessori e profondità della penetrazione interna

Dalle misure effettuate sugli spessori degli strati di ossido nei vari campioni si è osservata una certa corrispondenza con quanto ricavato dal calcolo della massa guadagnata dopo ossidazione. La lega contenente il 10 at.% di Cr è risultata quella ad aver sviluppato lo strato di ossido più spesso. La crosta esterna ha infatti raggiunto complessivamente i 32μm di spessore mentre il danneggiamente interno ha una lunghezza media di circa 17μm dopo 21 giorni di esposizione. Per questo materiale non è stato possibile stimare una media dello spessore dopo 42 giorni essendo il campione completamente scrostato. I campioni relativi alla lega contenente il 15 at.% di Cr hanno mostrato un andamento analogo a quello osservato nella lega contenente il 10 at.% di Cr, ma con valori di spes-

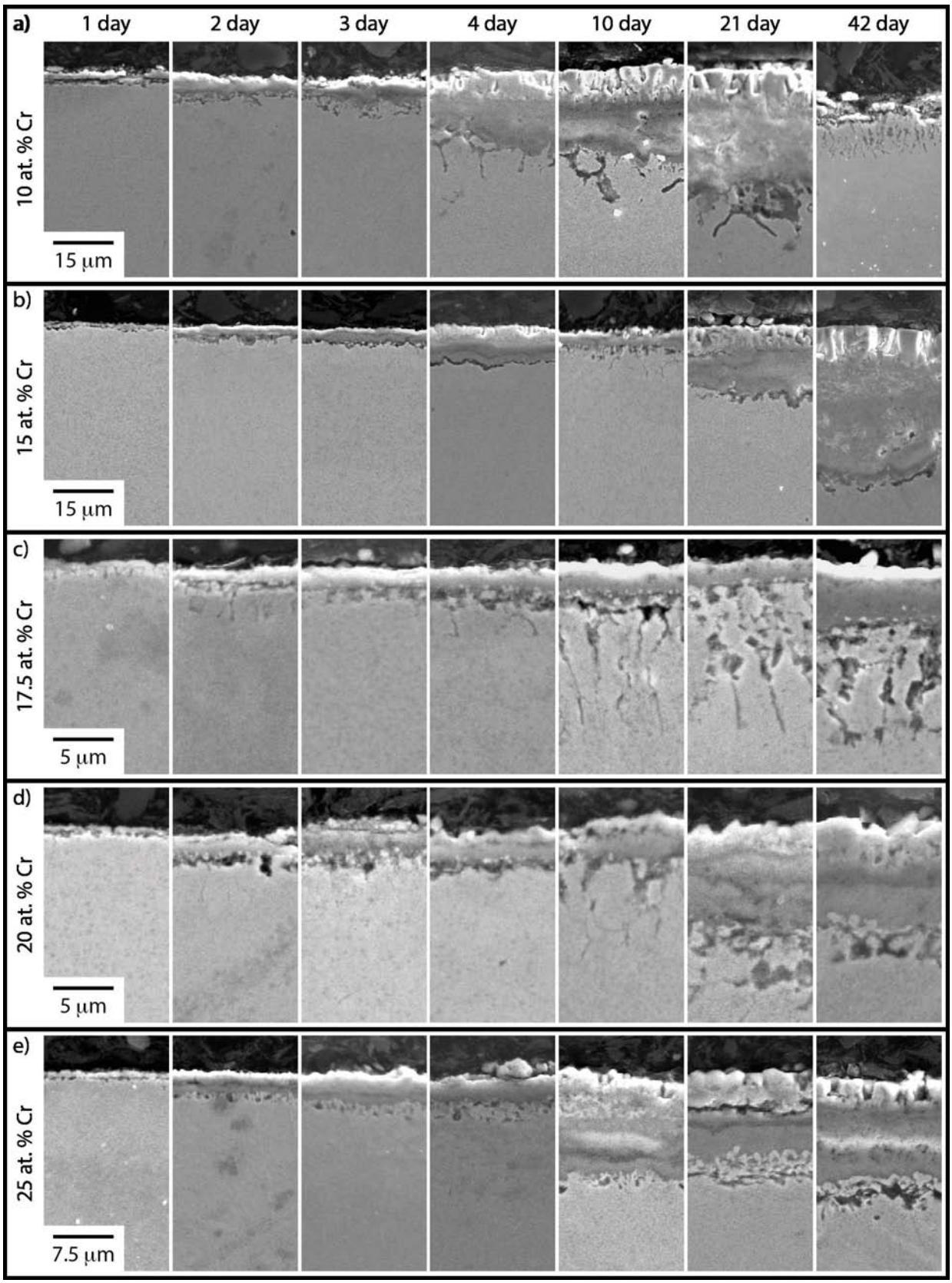

Figure 2: Micrografie SEI degli strati di ossido sviluppuati su ciascun campione dopo ossidazione isoterma a 800°Cin aria fino a 42 giorni di esposizione.

sore dello strato esterno e lunghezza del danneggiamento interno pari a circa la metà. L'anomalia riscontrata nel campione contenente il 15 at.% di Cr ossidato per 10 giorni è osservabile anche dalle misure degli spessori. In questo caso si osserva uno spessore dell'ossido molto piccolo, ma al contempo si può distinguere un picco nella lunghezza degli ossidi interni tale per cui si può pensare che il danneggiamento complessivo composto da ossido esterno e interno sia in linea con quanto osservato per gli altri campioni aventi la medesima composizione. Le due leghe contenenti il 17.5 e 20 at.% di Cr hanno mostrato un comportamento molto simile e sono quelle che presentano gli strati di ossido esterno più sottili. Per entrambe si è osservato uno spessore massimo pari circa 5μm dopo 42 giorni di esposizione. La differenza tra questi due materiali è però visibile per quanto riguarda la lunghezza media degli ossidi interni che si sono sviluppati. La lega contenente il 17.5 at.% di Cr ha infatti mostrato il danneggiamento interno più profondo dopo quello esibito dai campioni contenenti il 10 at.% di Cr. Per quanto riguarda la lega con il 20 at.% di Cr si è osservata invece una penetrazione interna molto bassa e pari ad un valore medio massimo di circa 6.5μm dopo 42 giorni. La lega contenente il 25 at.% di Cr invece non ha mostrato la miglior resistenza ad ossidazione come si poteva invece supporre. Lo strato di ossido esterno ha mostrato spessori intermedi tra quelli visti per la lega contenente il 15 at.% di Cr e quelli osservati nei campioni con il 17.5 e 20 at.% di Cr. Questo materiale ha però mostrato la miglior resistenza a danneggaimento interno come mostrato dal basso valore misurato per la profondità degli ossidi interni e pari a circa 6μm dopo 42 giorni di ossidazione.

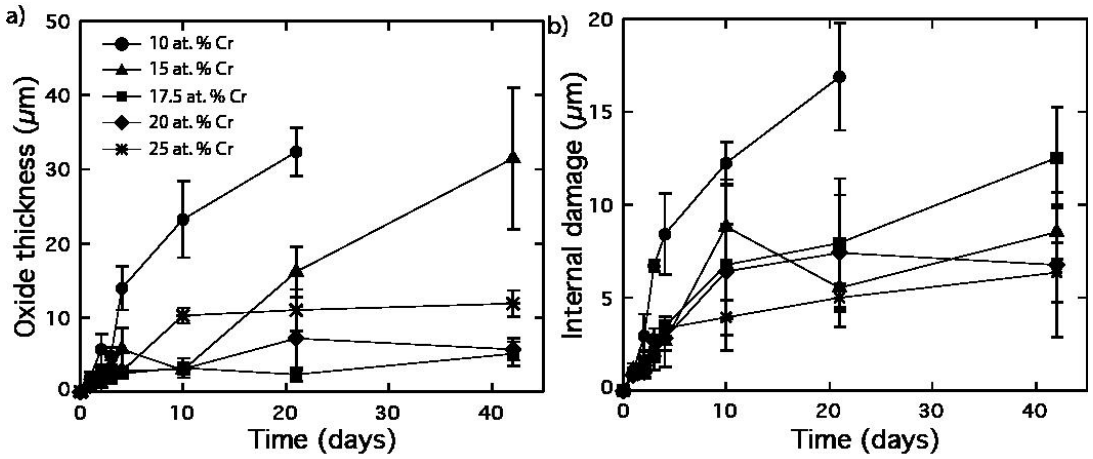

Figure 3: Misura dello spessore degli ossidi esterni e dell'entità del penetramento di ossido interno nelle cinque leghe dopo ossidazione.

Mappe EDX degli elementi

Dalle analisi EDX si sono potute ottenere informazioni più dettagliate per quanto riguarda la struttura degli strati di ossido e la composizione di questi dopo 42 giorni di ossidazione. Per quanto discusso precedentemente, la lega contenente il 10 at.% di Cr presenta un'eccezione in quanto l'analisi EDX è stata effettuata sul campione ossidato per 21 giorni. Le mappe degli elementi relative ai campioni contenenti il 10 e 15 at.% di Cr hanno evidenziato come il comportamento di queste due leghe sia molto simile confermando quanto osservato già dalle sezioni degli ossidi. In entrambi i casi si è osservato che lo starto più esterno, quello a crescita colonnare, è composto da un ossido misto a base di Ni e Co e leggermente arricchito in W. Subito sotto questo strato è presente una regione mista particolarmente ricca in ossido di Co e Cr. In questo secondo strato è possibile notare come l'ossido di Cr sia molto disperso e non si sia formato uno strato di cromia continuo. Si può notare inoltre come questi primi due strati costituiscano la maggior parte della crosta di ossido esterno. Un terzo strato è distinguibile al di sotto di questi composto per lo più da ossidi di Al e Ti che sono penetrati all'interno del substrato metallico sottostante. Per quanto riguarda la profondità di penetrazione da parte di questi ossidi si può notare come questa sia maggiore nella lega contenente il 10 at.% di Cr rispetto a quela con il 15 at.% di Cr. Al di sotto dello strato di ossidazione interna è possibile osservare una fascia di maeriale metallico arricchita in Ni ed impoverita in Cr. Da queste mappe si osserva infine come il Mo non abbia influito sulla formazione di ossidi. Solo al di sotto dello strato di ossido misto a base di Cr e Co si possono notare nelle aree in cui sembra esserci un arricchimento in Mo, ma non è possibile riscontrare un arricchimento in osigeno in corrispondenza di questi punti. Questo porta quindi a pensare che ci sia una precipitazione di fasi intermetalliche ricche in Mo al di sotto dello strato di ossido esterno.

Dal confronto tra le mappe EDX è stato possibile inoltre evidenziare le differenze microstrutturali presenti tra gli strati di ossido relativi ai campioni contenenti 17.5 e 20 at.% di Cr. Per entrame le leghe si è osservato uno strato più esterno composto da ossidi di Ni, Co e Cr, ma questo è risultato essere più sottile nella materiale con il 20 at.% di Cr. Al di sotto di questo si è osservata in entrambi i materiali uno strato continuo di ossido di Cr dello spessore di circa 1-2μm. Al di sotto di questo srato, il materiale contenente il 17.5 at.% di Cr ha mostrato una regione composta da ossidi di Al e Ti penetrati all'interno

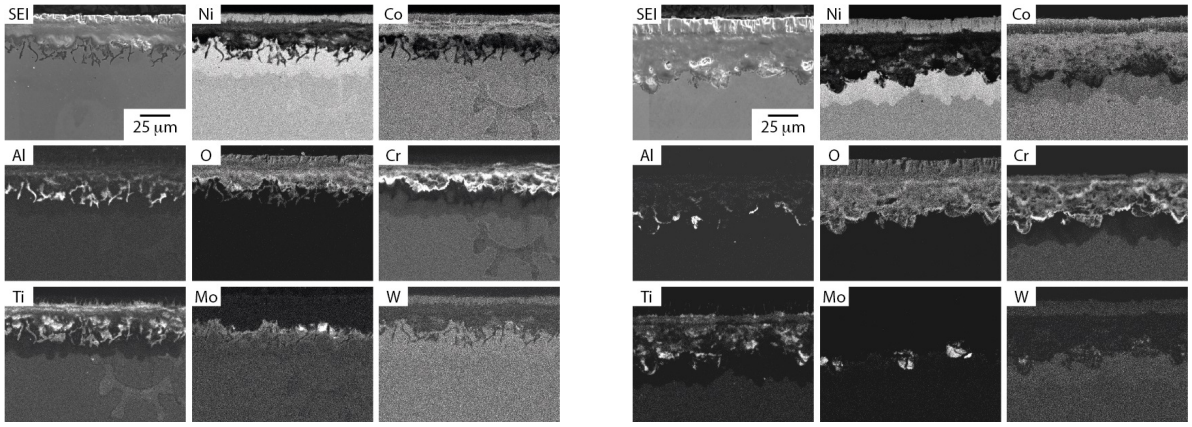

Figure 4: Mappe di distribuzione degli elementi nella lega con 10 at.% di Cr dopo 21 giorni (sinistra) e 15 at.% di Cr dopo 42 giorni (destra) a 800°C.

del substrato metallico. In questo caso si è notata anche la precipitazione di nitruri di Ti assieme agli ossidi interni testimoniata dalla presenza di aree particolarmente ricche in Ti, ma al contempo prive di ossigeno. Sfortunatamente non è stato possibile rilevare la presenza di N in quanto il dispositivo per le misure EDX non disponeva di una sensibilità sufficiente. Il campione con il 20 at.% di Cr ha invece mostrato un danneggiamento interno differente e costituito da un sottile strato continuo di allumina al di sotto della crosta di ossido esterno. In questo caso si è osservata la presenza di Ti solo al di sotto dello strato di ossido di Al, ma non vi è corrispondenza con la presenza di ossigeno nelle aree ricche in Ti. Si può quindi pensare che per questo materiale vi sia una precipitazione interna di nitruri di Ti, ma non di ossidi di Ti. Anche per queste due leghe è stato possibile osservare una regione impoverita in Cr e ricca in Ni al di sotto della regione degli ossidi interni. In questa regione si possono inoltre notare delle aree di arricchimento locale in Mo e Cr nel campione contenente il 20 at.% di Cr. Questo testimonia la presenza di fasi TCP, in particolare la fase σ, precipitate nella fase metallica.

Il campione contenente il 25 at.% di Cr ha mostrato una struttura interna significativamente differente rispetto a quella osservata per gli altri materiali studiati. Lo strato esternoa crescita colonnare è risultato in quetsi caso composto principalmente da ossido di Ni, anche se sono state rilevate tracce di Co. In questa regione è stata osservata inoltre la presenza di piccolissime tracce di ossido di Ti. Lo strato sottostante è costituito principalmente da ossidi di Co e Cr, ma anche qui si è notata la presenza di particelle di ossido di Ti disperse. Al di sotto è presente un trezo strato di ossido esterno composto

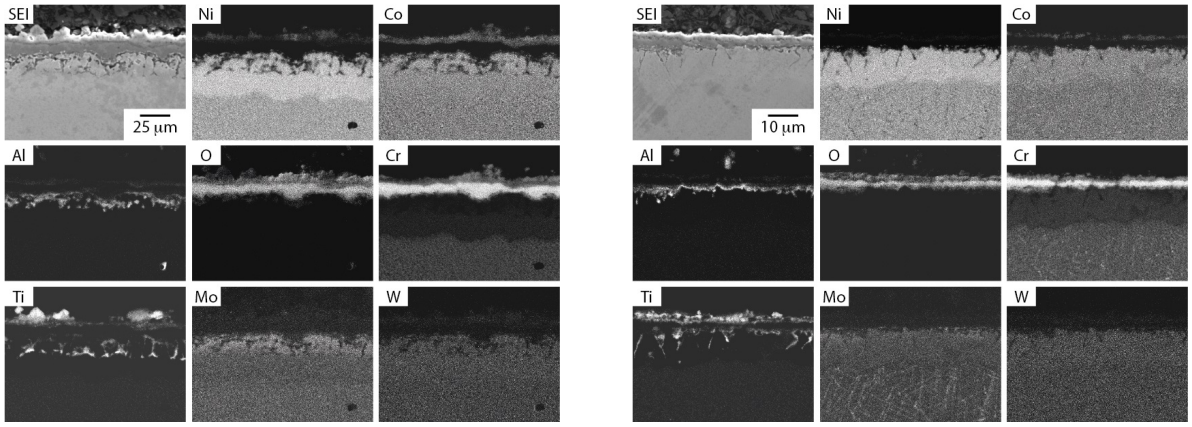

Figure 5: Mappe di distribuzione degli elementi nella lega con 17.5 at.% di Cr (sinistra) e 20 at.% di Cr dopo 42 giorni (destra) dopo 42 giorni a 800°C.

da una fascia continua di ossido di Cr dello spessore medio di circa 5μm. Tra ossido esterno e substrato metallico è presente anche in questo caso un sottile strato di ossido di Al continuo, simile a quello osservato nella lega contenente il 20 at.% di Cr. La regione di danneggiamento interno appare composta principalmente da notruri di Ti e ossidi di Al. Anche per questa lega si è osservata una regione impoverita in Cr ed arricchita in Ni al di sotto della regione di danneggiamento interno. Come per la lega contenente il 20 at.% di Cr sono state rilevate aree di arricchimento locale di Cr e Mo che suggeriscono la precipitazione di fase intermetallica σ.

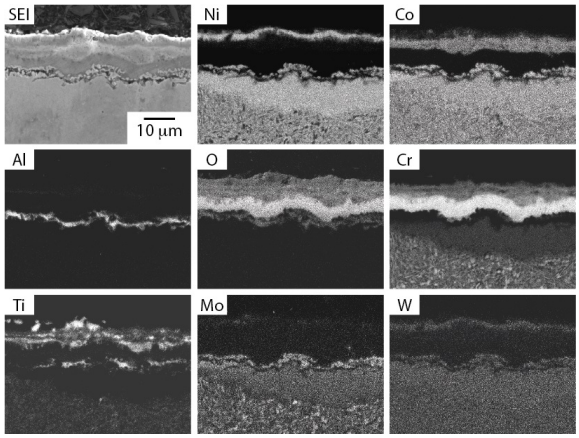

Figure 6: Mappe di distribuzione degli elementi nella lega con 25 at.% di Cr dopo 42 giorni a 800°C.

Discussione

Variazione di massa

I grafici che mettono in relazione la massa guadagnata dai campioni in funzione del tempo di esposizione in ambiente ossidante sono strettamente correlati a quelli ottenuti dalle misure degli spessori degli strati di ossido esterno e delle profondità di penetrazione degli ossidi interni. Per questo motivo sono stati rappresentate le variazioni di massa dei campioni in funzione sia degli spessori che delle profondità di penetrazine degli ossidi.

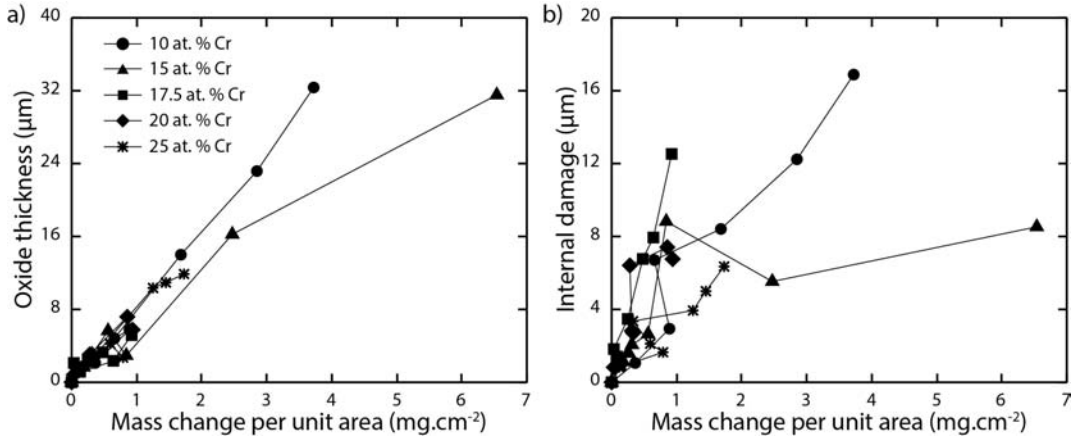

Figure 7: (a) Spessore dello strato di ossido esterno e (b) profondità della penetrazione interna in funzione della variazione di massa per unità di superficie.

Si può notare come la massa guadagnata e lo spessore dello strato di ossido esterno presentino una correlazione lineare per qualsiasi materiale, mentre in funzione della profondità di penetrazione degli ossidi interni vi è una certa dipendenza dalla composzione chimica della lega. Pertanto si può osservare come il grafici che mostrano la variazione di massa non siano da soli sufficienti a descrivere la resistenza ad ossidazione di queste leghe. Predendo ad esmepio la lega contenente il 17.5 at.% di Cr si nota come abbia mostrato una lieve variazione di massa e un sottile strato di ossido esterno, ma al contempo un'elevata profondità di penetrazione di ossidi interni. Inoltre è possibile notare come fino a 10 giorni di esposizione non vi sono tracce significative di danneggiamento interno, che invece aumenta in maniera sostanziale per periodi di esposizone superiori. Questo porta ad afferamere che va prestata attenzione nel valutare la resistenza ad ossidazione di una lega di questo tempo con tenciche di indagine che prevedono tempi di analisi più brevi.

Morfologia degli ossidi esterni

Dai risultati ottenuti con le analisi in scansione elettronica, sia dalle micrografie con elettroni secondari, sia dalle analisi EDX, è possibile ipotizzare una classificazione delle leghe studiate in base al comportamento ad ossidazione. Le leghe contenenti il 10 e 15 at.% di Cr presentano infatti uno strato di ossido sterno costituito principalmente da Ni e Co seguito da uno strato interno discontinuo composto da ossidi di Cr e Al dispersi. Questa microstruttura è tipica delle leghe aventi meccanismo di ossidazone di Tipo I. La lega contenente il 17.5 at.% di Cr presenta invece un meccanismo di ossidazione tipico dei materiali di Tipo II, ossia sviluppando uno strato esterno di ossido di Cr al di sotto del quale è presente uan regione costitiuta da ossido di alluminio penetrato internamente. Si può quindi pensare che la transizione tra i meccanismi di ossidazione di Tipo I e Tipo II giaccia tra le leghe che hanno una composizione intermedia tra quella avente il 15 at.% di Cr e quella con il 17.5 at.% di Cr.

Nelle leghe che hanno mostrato un'ossidazione di Tipo II si è osservato uno strato esterno composto principalmente da ossidi di Ni e Co che è però risultato notevolmente più spesso nella lega contenente il 25 at.% di Cr. Analogamente, anche lo strato compatto di ossido di Cr sottostante è risultato più spesso in questo materiale. Queste differenze possono essere attribuite alla differente cinetica di diffusione nella fomrazione dell'ossido in questi materiali. Teorie riguardanti il trasporto di ioni attraverso lo stratp di ossido suggeriscono l'incorporazione di cationi con valenza inferiore, come ad esempio Ni^{2+}, in un ossido semiconduttore di tipo p, come Cr_2O_3, porti ad una riduzione della concentrazione di difetti intrinseci. Questo implica quindi una riduzione del tasso di trasferimento di ioni attraverso lo strato di ossido di Cr e conseguentemente previene lo sviluppo di spessori elevati per lo strato di Cr_2O_3 e quello di ossido di Ni e Co sovrastante. Secondo studi condotti su leghe multicomponenete a base Ni si è osservato che il tasso di ossidazione più basso si ottiene con conentrazioni di Cr comprese tra 15-20 wt.%, confermando il fatto che un ulterioreaumento di Cr in lega porta ad un aumento del tasso di ossidazione.

Morfologia di ossidi interni e strato di impoverimento

Anche per quanto riguarda l'evoluzone degli ossidi interni si possono classificare le cinque leghe in maniera analoga a quanto fatto per gli ossidi esterni. Le leghe contenenti 10 e

15 at.% di Cr hanno mostrato ossidi interni allungati che sono penetrati in profondità nel substrato metallico confermando un comportamento ad ossidazione di Tipo I. La lega contenente il 17.5 at.% di Cr ha mostrato anch'essa una penetrazione considerevole degli ossidi interni, specie se confrontata con lo spessore dello srato di ossido esterno. La formazione di grani interni aciculari per questa lega può essere attribuita ad una differenza tra la velocità di accrescimento delle particelle di ossido tra loro, coarsening, e il fornte di avanzamento della reazione verso l'interno del substrato metallico. Questa condizione porta ad una diffuzione preferziale degli atomi di ossigeno verso la punta degli aghi di ossido favorendo quindi la crescita longitudinale di questi a discapito della nucleazione di nuovi grani. Le leghe contenenti tenori di Cr più elevati presentano un fornte di avanzamento della reazione di ossidazione con una velocità più bassa, pertanto sono meno propense a formare grani allungati. Inoltre lo sviluppo di allumina interna può essere favorito anche dalle diverse attività di Al al variare della composizione del materiale. Questo è osservabile dalla formazione di um film continuo di ossido di Al nella lega con il 25 at.% di Cr. Si può quindi pensare che la lega contenente di 20 at.% di Cr si sia comportata in maniera intermedia tra quanto osservato nei campioni contenenti 17.5 e 25 at.% di Cr.

Anche il comporamento del Ti in lega varia in funzione del tenore di Cr dissolto. Le leghe contenenti 10 e 15 at.% di Cr hanno subito un danneggiamento interno fortemente influenzato dalla formazione di ossido di Ti. Questo può essere attribuito alla scarsa protezione offerta dallo strato esterno di ossido di Ni e Co alla penetrazione dell'ossigeno. Nelle leghe contenenti $\geq$17.5 si è osservata al contrario una riduzione della diffusione di ossigeno all'interno dovuta alla formazione di uno strato cir ossido di Cr protettivo. Il risultato è stata la formazione preferenziale di ossido di Al e nitruri di Ti in quanto ossido di Ti e nitruro di Al presentano energie di Gibbs più elevate.

La regione di arricchimento in Ni osservabile in tutte le leghe al di sotto dello strato di ossido è originata dal moto diffusivo di elementi quali Cr, Al e Ti per la formazione degli ossidi stessi. Si è osservato inoltre che la formazione di allumina è stata favorita dalla dissoluzione della fase γ' che agisce come riserva di Al in prossimità degli ossidi. Analogamente le fasi intermetalliche precipitate nelle leghe contenenti 20 e 25 at.% di Cr fungono da riserve di Cr per la formazione di ossido. In queste leghe si è quindi osservata una seconda regione di transizione all'interno della regione ricca in Ni e priva di grani

di γ' dovuta alla dissoluzione dei precipitati intermetallici che si sono formati durante l'esperimento.

Conclusioni

In conclusione si può affermare che il comportamento ad ossidazione delle leghe contenenti 10 e 15 at.% di Cr sia pienamente di Tipo I. Questi fue materiali hanno mostrato i valori di massa guadagnata dopo ossidazione più elevati e la formazione di uno strato di ossido esterno continuo composto da ossidi di Ni e Co ed un considerevole danneggiamento da ossidi interni. Questi due materiali hanno inoltre mostrato una tendeza a scrostarsi a causa della formazione di ossidi durante l'intervallo di tempo studiato in questa ricerca. La lega con il 17.5 at.% di Cr ha mostrato un comportamento ad ossidazione di tipo II sviluppando uno strato di ossido di Cr esterno compatto. Anche il materiale con il 20 at.% di Cr ha mostrato un'ossidazione esterna analoga a quella svilupata dall alega con il 17.5 at.% di Cr, ma quest'ultima ha subito un maggior danneggiamento da ossidi interni. La lega con il 25 at.% di Cr ha mostrato uno strato di ossido esterno molto spesso accompagnato da un aumento di massa dopo ossidazione più elevato rispetto a quello relativo alle leghe con 17.5 e 20 at.% di Cr. Questo risultato è in linea con quanto osservato per i sistemi binari Ni-Cr ed è associato ad un aumento della diffusione attraverso gli ossidi. Dai risultati ottenuti in questa ricerca si è concluso inoltre che vi è una stretta correlazione tra la variazione di massa per unità di sperficie e lo spessore dell'ossido esterno, mentre non è stato osservato un legame così evidente tra variazione di massa per unità di superficie e profondità del danneggiamento interno. Da queste osservazioni si può concludere che le analisi termogravimetriche non consentono di valutare pienamente l'entità dell'ossidazione in leghe di questo tipo in quanto è necessario effettuare dei test tali prevedere tempi di esposizione dei campioni sufficienti da consentire le variazioni microstrutturali dovute all'ossidazione.

Introduction

Polycrystalline nickel-base superalloys are the only materials able to meet the service requirements of the turbine discs in the high-pressure stages of gas turbine engines. However, the elevated temperature and stresses required by future, more efficient engine designs, will exceed those that can be endured by current nickel-base superalloys and new alloys must therefore be developed. To facilitate the effective development of new nickel-base superalloys, an improved understanding of the role of alloying elements must be established. Nickel-base superalloys typically comprise a γ matrix strengthened by γ' precipitates and contain in excess of ten alloying elements to achieve the balance of properties required. The environmental resistance of alloys designed for service below 900℃is often realised through Cr additions, which lead to the formation of a protective chromia scale. In addition, the Al used to promote the formation of the γ' phase assists in the formation of the protective chromia scale, through increasing the activity of Cr in the alloy. However, excessive additions of Cr can lead to the precipitation of undesirable topologically close packed (TCP) phases, which compromise alloy performance.

Previous studies of the oxidation resistance of Ni-Cr-Al alloys have identified three distinct types of oxidation behaviour. Type I oxidation behaviour, characterised by the formation of an external NiO scale with alumina and chromia internal oxides, is seen in alloys containing low concentrations of both Al and Cr. Alloys containing higher concentrations of Cr ($\geq$10 wt.%) form continuous chromia external scales with alumina internal oxides, Type II oxidation behaviour. Elevated concentrations of Al ($\geq$5 wt.%) may promote the formation of a continuous external alumina scale only, Type III behaviour. However, these behaviours are sensitive to other elemental additions and exposure temperature. Alloying with Co has been shown to promote the formation of a NiO top scale, and reduces the oxidation resistance by decreasing the time to oxide spallation. Among

other additions, Ti has been reported to increase the extent of internal oxidation.

Udimet 720Li is currently used for turbine discs in gas turbine engines and combines high strength from γ' precipitation with good environmental resistance. In this study, the effect of varying the Cr content on the oxidation behaviour of a model alloy based on Udimet 720Li has been investigated. As such, the alloys investigated in the present study were produced with Cr concentrations, varying from 10 to 25 at.%. The alloys were subsequently isothermally exposed at 800℃in air for up to 42 days to investigate their oxidation response. Alloys with less than 17.5 at.% Cr exhibited large mass gains and formed extensive non-protective oxide scales. Higher Cr concentrations led to the formation of a continuous protective chromia layer and lower mass gains after all exposure times. The alloy containing the highest Cr concentration exhibited inferior oxidation characteristics to those with 17.5 and 20 at.% Cr, as a result of more rapid diffusion through the oxide. Data acquired in this study indicated that mass gain data alone does not capture all aspects of oxidation damage and that care must be taken when drawing conclusions from short–duration exposures about an alloy's oxidation behaviour.

Chapter 1

Superalloys: microstructure and properties

1.1 Superalloys as high temperature materials

1.1.1 Materials for gas turbine engines

Materials that can be considered ideal for high temperature applications must have specific characteristics. First of all is the ability to withstand a load at an operating temperature that is very close to the melting temprature of the material. This property is evaluated in terms of homologus temperature τ, that is defined as follows:

$$\tau = \frac{T_{OPER}}{T_m} \tag{1.1}$$

Where T_{OPER} is the operating temperature and T_m is the melting temperature of the material. Considering that the melting temperature of nickel is 1455℃, a nickel based superalloy that operates at 1000℃in a gas turbine engine can be considered a high temperature material.

Another important characteristic is the resistance to mechanical degradation over extened periods of time, which means excellent creep resistance for high temperature applications. In addition, typical features of structural materials are required, such as high yield stress, ultimate tensile strength and fracture toughness.

Finally, it is important to guarantee high resistance to severe operating environments. The high operating temperatures in gas turbine engines enhance the possibility of oxida-

tion. Furthemore, hot gases generated by the combustion of fuel, for example kerosene for aeroengines, present corrosive impurities that are detrimental for engines components. This leads to surface degradation and therefore reduces components life.

In the case of gas turbine engines for jet propoulsion operating temperatures are beyond 800℃[1] and all the previously described characteristic for high temperature materials are required. For these reasons, nickel based superalloys are the material of choice for these applications.

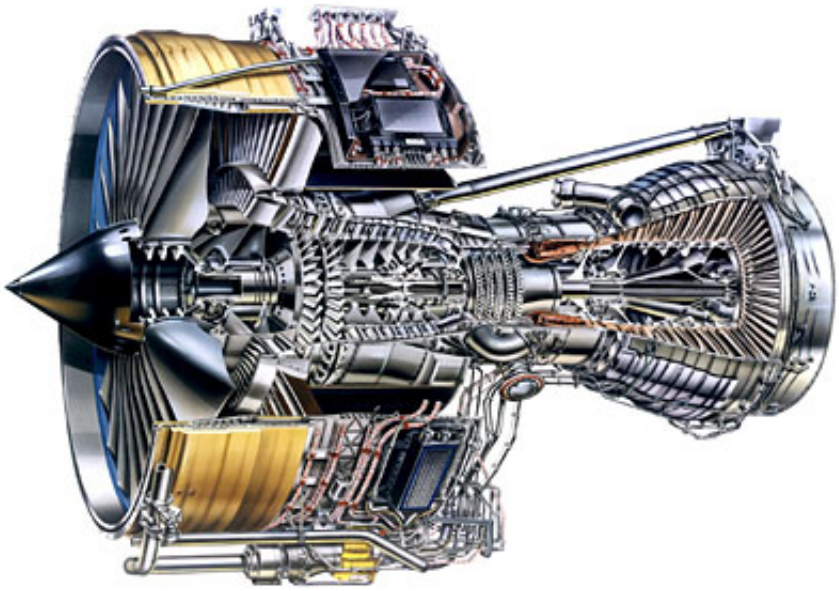

Figure 1.1: Artist's impression of the Rolls-Royce's Trent 800 engine.

In order to understand the role of nickel based superalloys, a brief description of a simple gas turbine engine is provided. A turboject engine, Figure 1.2, is composed of a compressor, a combustor, a shaft, a turbine and an exhaust nozzle. The compressor consists of a series of blades and discs whose function is to squeeze the incoming air, thus increasing its pressure. Since the temperature is not very high, in the intial stages on the compressor titanium alloys are chosen thanks to their low density, good specific strength and fatigue resistance. In the final stages of the compressor, where temprature and pressure increase, nickel based superalloys are preferred.

The compressed air than enters in the combustor where is mixed with fuel. Here the gas mixture is ignited allowing the combustion gases that have been produced to expand

through the turbine. The latter component extracts the mechanical work required to drive the compressor taking advantage of the gas expansion. This mechanism necessitates the shaft that allows the transmission of the torque from the turbine to the compressor. For the components of the combustor and the turbine nickel based superalloys are almost exclusively chosen.

In turbojet engines, thrust arises from the expulsion of the residual combustion gases at a significantly high velocity from the exhaust nozzle. The velocity variation is due to the momentum change between the compressed air in entrance at the combustor and the expanded gases exiting through the turbine.

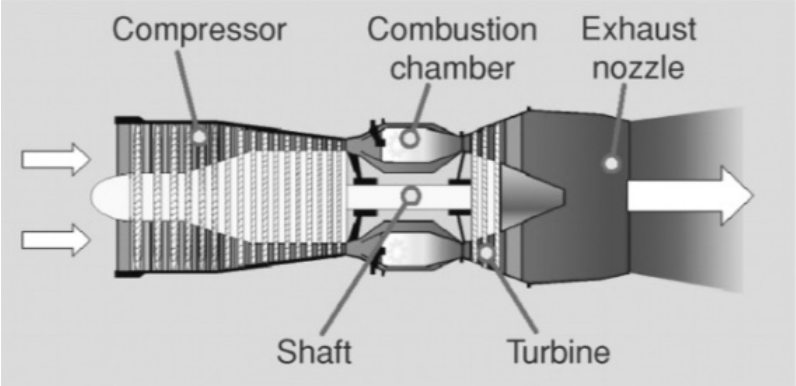

Figure 1.2: Schematic representation of the turbojet gas turbine engine, [2].

One of the most important aspects in the design of a new gas turbine engine is the turbine entry temeprature (TET), that is the temperature of the hot gases at the entrance of the turbine [3]. Since the extracted mechanical work is strictly related to the temperature, raising the TET leads to a significant improvment of the engine performance. Therefore, the design of new high temperature alloys with improved characteristics is essential [4].

1.1.2 Nickel as high temperature material

Under the condition of high temperature deformation, the creep shear strain rate $\dot{\gamma}$ for a pure metal is proportional to the volume diffusivity [5]:

$$\dot{\gamma} \propto D_{0,v} \exp\left(-\frac{Q_v}{RT}\right) \tag{1.2}$$

Where Q_v is the activational energy and $D_{0,v}$ is a pre-exponential term. Equation 1.2 can be normalized in order to become dimensionless and to facilitate the comparison of

different materials, Equation 1.3.

$$\overline{\dot{\gamma}} = \frac{\dot{\gamma}\Omega^{\frac{2}{3}}}{D_{T_m}} \propto \Omega^{\frac{2}{3}} \exp\left[-\frac{Q_v}{RT_m}\left(\frac{T_m}{T} - 1\right)\right] \tag{1.3}$$

Where T_m is the melting temperature, D_{T_m} is the diffusivity at the melting temperature and Ω is the atomic volume. From Equation 1.3 is possible to distinguish three dimensioless groups:

- homologous temeprature $\frac{T}{T_m}$;
- normalised activation energy $\frac{Q_v}{RT_m}$;
- normalising parameter $\frac{\Omega^{\frac{2}{3}}}{D_{T_m}}$.

Assuming that the normalised activation energy is approximately the same for different materials, is important to chose materials with high melting temperature in order to minimize the homologous temperature. Similarly, if the material is chosen to work at a certain homologous temperature, materials with the maximum $\frac{Q_v}{RT_m}$ and $\frac{\Omega^{\frac{2}{3}}}{D_{T_m}}$ are the ideal ones.

Nickel displays a FCC crystal structure, thus it combines ductility and toughness. Furthermore, nickel has a stable crystal structure from room temperature to its melting. In fact, metals that display phase transformation are subject to variations of melting point diffusivity and normalised activation energy. FCC metals also exhibit low melting point diffusivity and high normalised activation energies compared to HCP and BCC metals [6]] and this means that thermally activated creep is limited. Nickel in particular presents low values for these two characteristics, hence its microstructure is considerably stable at high temepratures. Finally, there are other materials that can be considered interesting for high temperatures applications, but they all result less efficient than Nickel. For example, platinum has an FCC structure and excellent stability, but is more dense and expensive than nickel; cobalt, which presents a HCP crystal structure, could be a good choice, but it is more expensive and chromium, that presents ductile/brittle transition.

1.2 Microstructure of polycrystalline nickel based alloys

In nickel based superalloys a wide variety of alloying elements are generally used. Most of them contains significant amounts of chromium, aluminium, cobalt and titanium, but small amounts of boron, zirconium, carbon, rhenium, tungsten, tantalum, hafnium, ruthenium, molybdenum and niobium are often included. There are also alloys that contain significant fractions of iron and are usually called nickel-iron superalloys. Different elements have different stabilities and tend to form different phases [7]:

- γ: this is the phase that constitutes the metallic matrix of the alloy where the other precipitates reside and has a FCC crystal structure. Elements as cobalt, chromium, molybdenum, ruthenium and rhenium tends to dissolve in this phase if they are present.
- γ': this is a precipitate phase that is usually coherent with the γ matrix. It is rich in elements such as aluminium, titanium and tantalum. In nickel-iron superalloys the γ" phase precipitate tends to form instead of the γ'.
- Carbides and borides: when carbon is present it combines with elements such as titanium, tantalum and hafnium to form MC type carbides. These carbides could later react with chromium, molybdenum and tungsten during service or processing operations and decompose to form $M_{23}C_6$ and M_6C carbides. These species prefer to reside in γ grain boundaries. Boron combines with elements such as chromium and molybdenum forming borides that tends to reside in γ grain boundaries.
- topologically closed packed (TCP) phases: these are undesired phases that tends to form during service in ageing consitions. Serveral types of TCP phases exisist such as σ, μ, laves and other. Care must be payed while chosing the elemental composition af an alloy in order to limitate rather than promoting TCP species precipitation.

1.2.1 The γ phase

The γ phase constitutes the matrix of the alloy and has a FCC crystal structure. As previously described, this phase must be stable in the FCC form and not subject to phase transformation in order to satisfy the requirements for a high temperature material.

Alloying with elements such as chromium, which presents a BCC strcuture, could lead to a undesired phase transformation during soldification. The Ni-Cr diagram, Figure 1.3, shows the presence of a BCC or a FCC+BCC structure depending the composition.

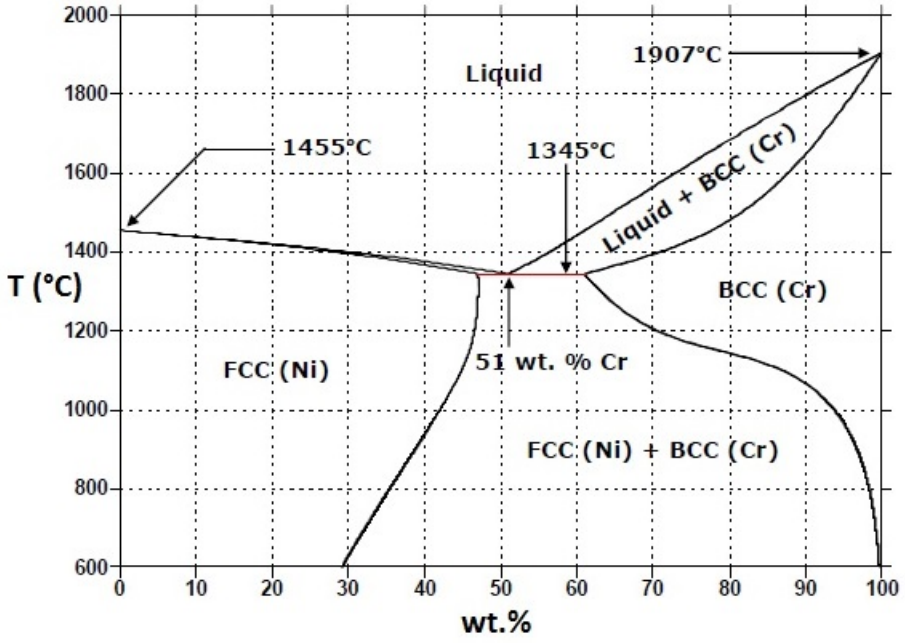

Figure 1.3: Ni-Cr binary phase diagram.

It is possibile to calculate the molar Gibbs free energies of each element in the solution for the phase transformation from liquid L to solid ϕ, where the FCC phase could be represented by the ϕ phase. As first approximation, the solid-liquid system can be considered ideal. The driving force for the phase transfomration of each component i is defined as:

$$\Delta G_i^{L\to\phi} = G_i^{\phi} - G_i^{L} \tag{1.4}$$

The liquid-solid coexistence region, bounded by the liquidus and solidus curves, is described by Equation 1.5 or, after some manipulation, Equation 1.6.

$$\mu_i^L = G_i^L + RT\ln x_i^L = \mu_i^{\phi} = G_i^{\phi} + RT\ln x_i^{\phi} \tag{1.5}$$

$$\frac{x_i^{\phi}}{x_i^L} = \exp\left(-\frac{\Delta G_i^{L\to\phi}}{RT}\right) \tag{1.6}$$

Equation 1.6 is consistent with the equilibrium condition that is represented by the equality of the chemical potentials μ_i^L and μ_i^{ϕ} of the solute i in each phase. The terms x_i^L and x_i^{ϕ} represent the mole fractions of component i in the liquid and solid phase respectively.

Ni solutions are rarely ideal in practice, thus these equations do not provide a correct representation of the phenomena. In the regular solution model the partial molar excess energy, $\Delta\overline{G}_i^{excess}$ must be considered. This feature is identified as the partial molar enthalpy of mixing, $\Delta\overline{H}_i^{mix}$, which is function of an interaction parameter Ω and the mole fraction of component i.

$$\Delta\overline{G}_i^{excess} = \Delta\overline{H}_i^{mix} = \Omega\left(1 - x_i\right)^2 \tag{1.7}$$

Equation 1.7 must be added to Equation 1.5, so that:

$$\mu_i^L = G_i^L + RT\ln x_i^L + \Delta\overline{G}_i^{excess,L} = \mu_i^\phi = G_i^\phi + RT\ln x_i^\phi + \Delta\overline{G}_i^{excess,\phi} \tag{1.8}$$

After some manipulation is possible to obtain Equations 1.9 and 1.10, where i=1 represents the solvent (nickel) and i=2 represents the solute (alloying elements).

$$\frac{\Delta G_1^{L\to\phi}}{RT} + \frac{\Omega^\phi}{RT}\left(x_2^\phi\right)^2 - \frac{\Omega^L}{RT}\left(x_2^L\right)^2 + \ln\left[\frac{\left(1 - x_2^\phi\right)}{\left(1 - x_2^L\right)}\right] = 0 \tag{1.9}$$

$$\frac{\Delta G_2^{L\to\phi}}{RT} + \frac{\Omega^\phi}{RT}\left(1 - x_2^\phi\right)^2 - \frac{\Omega^L}{RT}\left(1 - x_2^L\right)^2 + \ln\left(\frac{x_2^\phi}{x_2^L}\right) = 0 \tag{1.10}$$

The system composed by Equations 1.9 and 1.10 can be solved iteratively and therefore the mole fraction x_2^ϕ and x_2^L can be estimated. The values of Ω^ϕ and Ω^L are empirically calculated from experimental data. The calculation of the phase diagrams of multicomponent nickel based superalloys can be performed using themodynamic softwares equipped with themodynamic databases of parameters that enable the description of lattice stabilities and interaction parameters.

In Figure 1.4 the liquidus and solidus lines for several alloying elements are plotted. It is interesting to note how the liquidus curve is not affected by the melting temperature of each element. For example, rhenium has a strong positive effect on the liquidus temeprature. According to the Hume-Rothery rule, a strong correlation between the solubility of each element i and its atomic diameter is observed. Metals with atomic diameter comparable to that of nickel have shown a larger solubility in the FCC crystal structure, Figure 1.5.

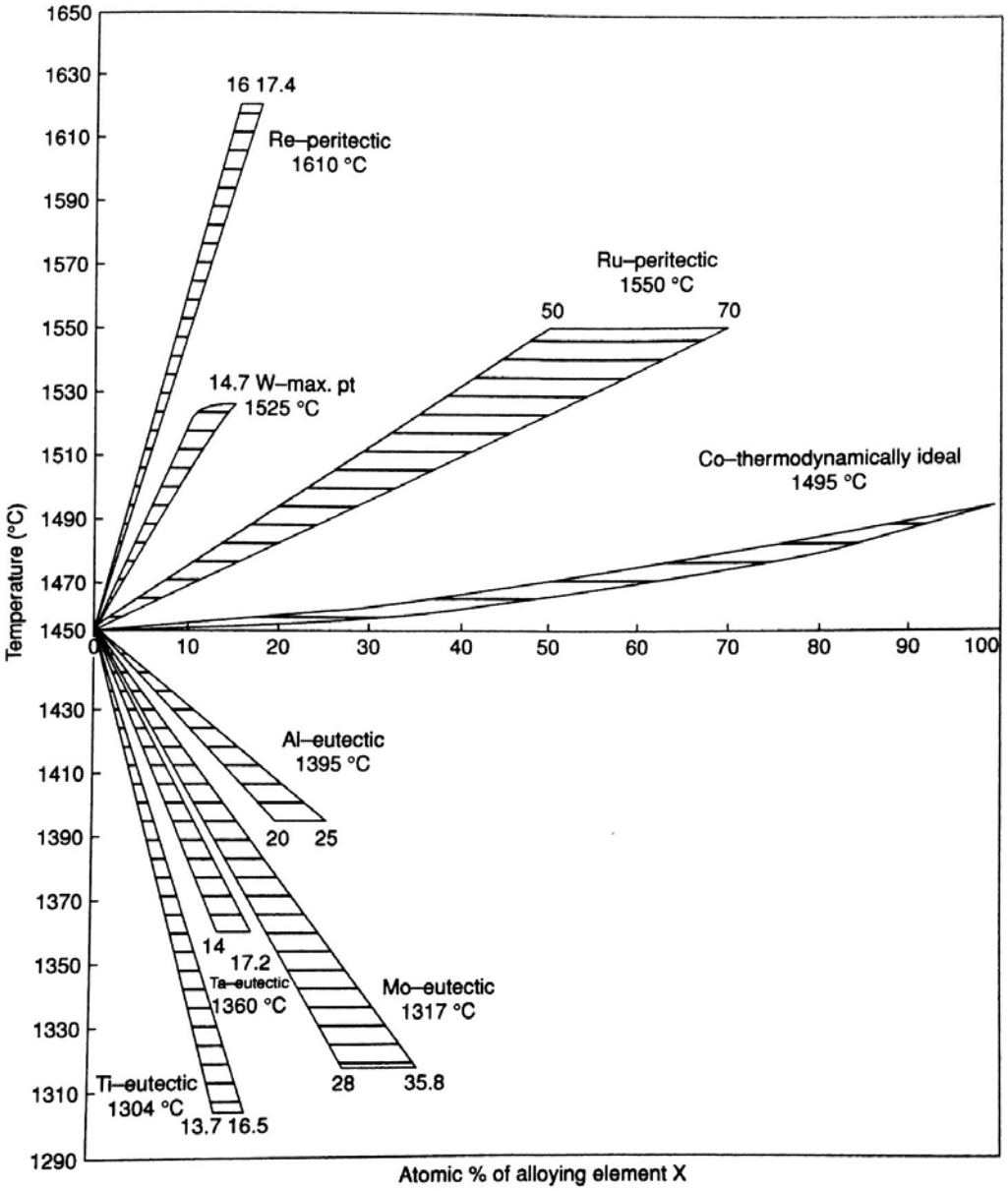

Figure 1.4: Liquidus and solidus curves for seveal alloying elements in binary Ni-X systems, [2].

1.2.2 The γ' phase

Although nickel and aluminium possess the FCC crystal structure, the solubility of the latter element is not very high as one could expect from what previously said. This is explained by the different crystal structures that the nickel and aliminium can form once combined, Figure 1.6. The chemical formulae of the species that could form are Ni_3Al, NiAl, Ni_2Al_3, $NiAl_3$ and Ni_2Al_9. Each phase is characterized by a different crystal structure that could be FCC or BCC. There are two reasons for the formation of these

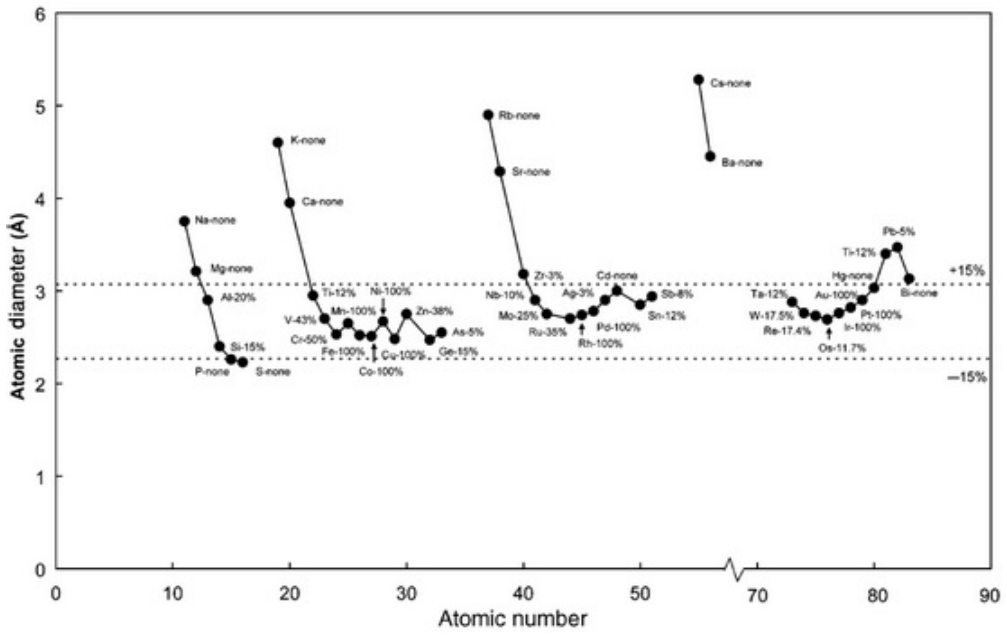

Figure 1.5: The atomic diameter of the elements is represented as function of the atomic number. The percentages represent the solubility of each element in the FCC crystal structure of nickel. The horizontal lines represents the ±15% deviations from the atomic diamater of nickel, [2].

species rather than dissolution of aluminium in the FCC matrix. The first is the precise stoichiometric relationships existing between Ni and Al that is orginated by a significant degree of directional covalent bonding. The second is the preference to form Ni-Al crystal structures rather than Ni-Ni or Al-Al structures. The most significant specie is the Ni_3Al, which confers strength to the superalloys.

Considering a ternary system Ni-Al-X, Figure 1.7, where X could be an element such as Co, Cr, Mo, W, etc. It is interesting to note that the γ' phase field is extended in the direction on which the alloying element X is soluble. Elements such as cobalt promote the extension of γ' parallel to the Ni-X axis thus suggesting that substitution of Ni is preferred. On the contrary, elements such as Ti promote the γ' field in parallel to the Al-X axis implying that the substitution of Al is preferred. In general, the substitution of Al is favoured by large elements while the substitution of Ni atoms is favoured by smaller atoms.

Since the entropic contribution to Gibbs free energy increases as the temperature is raised , it is important to know what is the degree of disordering of the γ' phase at high

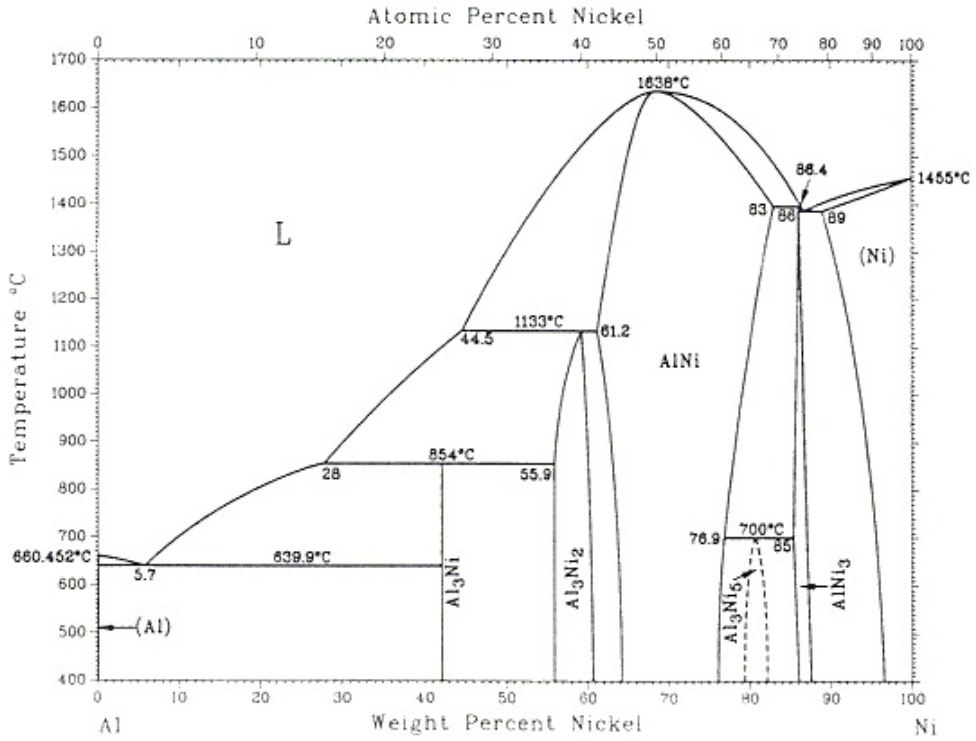

Figure 1.6: Ni-Al binary phase diagram, [8].

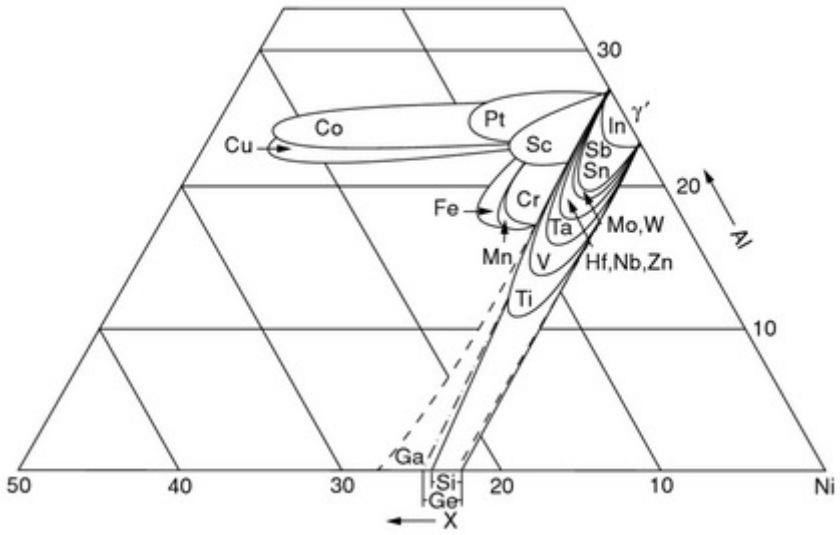

Figure 1.7: Ni-Al-X ternary phase diagram illustrating the effect of several alloying elements on the extension of the γ' field, [9].

temperature. It is known that the ordering temperature for the Ni_3Al phase is very closed to its melting temperature, 1375℃[10]. It was observed that γ' grains have a cuboidal shape in binary Ni-Al alloys [11]. Furthermore, the lattice parameters for the γ matrix and the γ' grains are similar and this leads to common maxima in the diffraction patterns of the two phases.

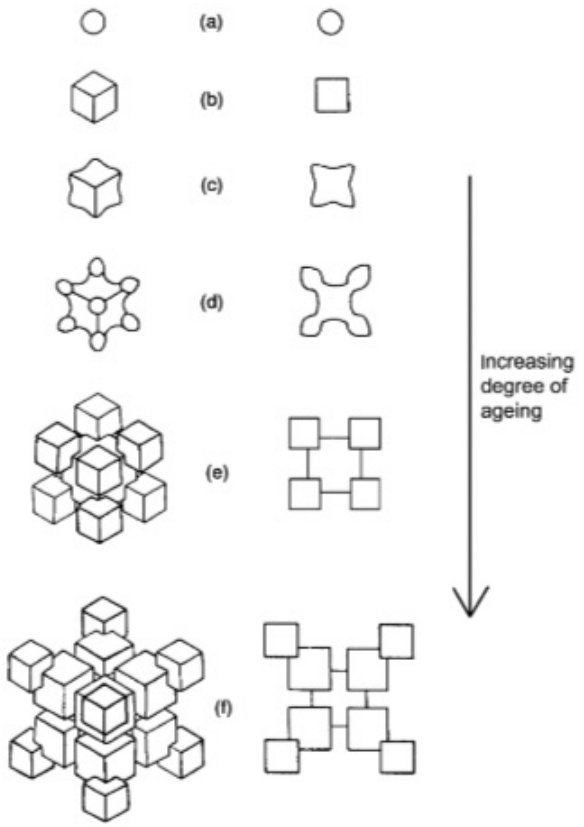

Figure 1.8: Development of the γ' grain morphology during ageing, [12].

The lattice misfit for the γ/γ' interface, δ, is definied as function of the lattice parameters of each phase, Equation 1.11.

$$\delta = 2 \cdot \left(\frac{a_{\gamma'} - a_{\gamma}}{a_{\gamma'} + a_{\gamma}} \right) \tag{1.11}$$

Where the lattice parameters are calculated according to the Vegard's relationship, Equations 1.12 and 1.13. These equations are function of the Vegard's coefficients, Γ_i^{γ} and $\Gamma_i^{\gamma'}$, whose values are strictly correlated to the position of the i element in the periodic table.

$$a_{\gamma} = a_{\gamma}^0 + \sum_i \Gamma_i^{\gamma} x_i^{\gamma} \tag{1.12}$$

$$a_{\gamma'} = a_{\gamma'}^0 + \sum_i \Gamma_i^{\gamma'} x_i^{\gamma'} \tag{1.13}$$

Furthermore, from Vegard's relationships, is possible to observe that δ depends on the partioning of the solute i in γ and γ'.

For what concerns the growth of γ' grains it was shown that the morphology develops in the sequence spheres, cuboids, arrays of cuboids and solid state dendrites [12], Figure 1.8. Moreover, it was found that coarsening of γ' grains is promoted by ageing and γ' development is influenced by the lattice misfit. For alloys with low misfits the size of the γ' spheres needs to be larger before the misfit strain effects are sufficient to promote the formation of cuboids.

1.2.3 The TCP phases

The formation of these precipitates is promoted by an excess of elements such as chromium, molybdenum, tungsten and rhenium [13]. In general, TCP phases are associate with some characteristics:

i. high and uniform packing density of atoms;

ii. a degree of non-metallic, directional bonding;

iii. their crystal structure is a complex result of the combination of distinct tasselated layers consisting of arrays of hexagons, pentagons and triangles stacked in a limited number of coordination polyedra also called Kasper coordination polyedra [14], Figure 1.9.

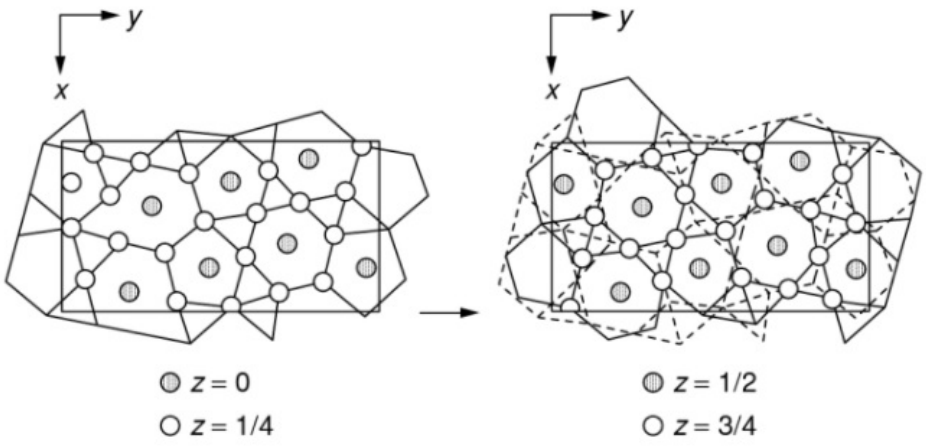

Figure 1.9: Example of TCP species: the unit cell of the P phase, [14].

TCP intermetallics have the general chemical formulae A_xB_y. In the specific case of the σ phase, the formulae is A_2B and has a tetragonal cell containing 30 atoms. Examples of σ species include Cr_2Ru, $Cr_{61}Co_{39}$ and $Re_{67}Mo_{33}$. However, TCP species can have different compositions due to the wide stochiometry ranges.

1.3 Turbine disc alloys

Turbine discs are subject to lower temperatures, but higher stresses if compared to turbine blades. Thus, an ideal material of choice for a turbine disc requires specific characteristics that are summarised as follows:

i. high yield stress and tensile strength in order to prevent yield and fracture;

ii. ductility and fracture toughness in order to tolerate defects;

iii. resistance to the initiation of fatigue cracking;

iv. ensure low rates of fatigue crack propagation.

Since temperatures are lower, creep resistance is considered less important for these components and less emphasis is given to enhance this property.

Contrary to alloys for turbine blades, where nowadays only single crystal alloys are employed, the alloys for discs are polycrystalline. Hence, the presence of grain boundaries in the strucutre is an added complexity. This implies that care must be taken when the chemical composition and the relative microstructure and morphology of the alloy are chosen. The choice of new alloys is ruled by three criteria that should be adhered to.

1.3.1 Criterion I: γ' phase

The first criterion of choice concerns the percentage of γ' grains in the superalloy. Since strength and fatigue resistance are enhanced by the presence of this phase is important to choose alloying elements that are γ' formers such as Al, Ti and Ta. The typical desired percentage of this precipitate lies between 40% to 55%. In Figure 1.10 the effect of several elements and temeprature on the strength of turbine disc alloys is shown. Titanium have proved a strong effect on the formation of γ' thus improving yield properties. Similarly, aluminium and niobium exhibited a beneficial effect on the formation of precipitates.

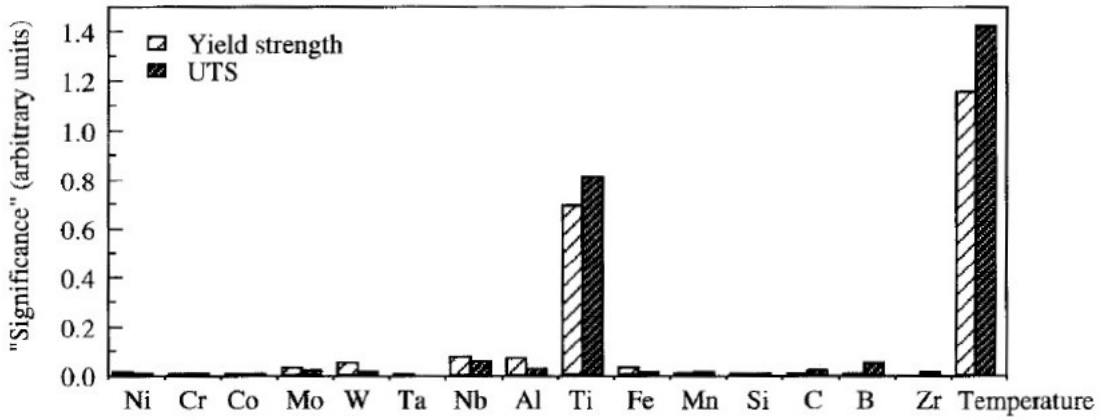

Figure 1.10: The chart shows the relative 'significance' of several elements and temperature on the yield and ultimate tensile strength (UTS) of turbine disc alloys, [15].

It was also observed that high Ti/Al ratios improve the resistance of the alloy in terms of yield stress and ultimate tensile strength, Figure 1.11. Cobalt was found to have a negligible effect on the yield properties, wehereas molybdenum has a strong positive effect on the maximum yield stress.

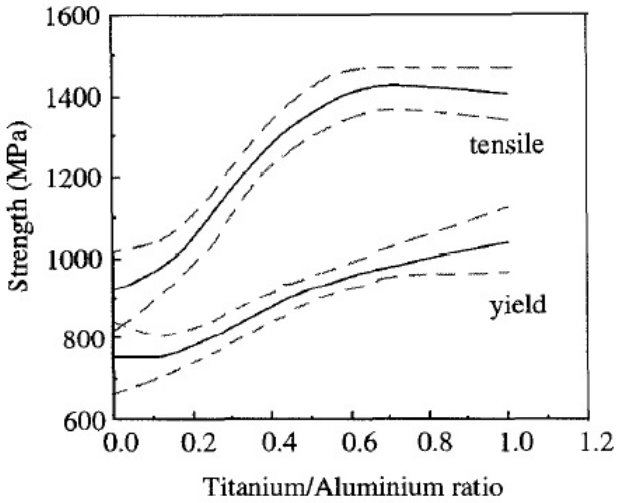

Figure 1.11: The curves show the beneficial effect of high Ti/Al ratios on the yield properties of turbine disc alloys, [15].

Yield stress of polycrystalline superalloys for turbine disc depends critically on the heat treatment applied to it. In particular, it was found that the solutioning treatment, which is carried out in the vicinity of the solvus temperature, is the most influent to yield

properties. For this alloys the solvus temperature lies between 1050℃and 1200℃. Sub-solvus treatments lead to the formation of primary γ' grains that have a grain-pinning effect on the γ grains. The result is a structure composed by small γ grains blocked by the presence of primary γ' on grain boundary triple points, Figure 1.12. On the contrary, a super-solvus treatment eliminates the primary γ' allowing the formation of coarsen γ grains.

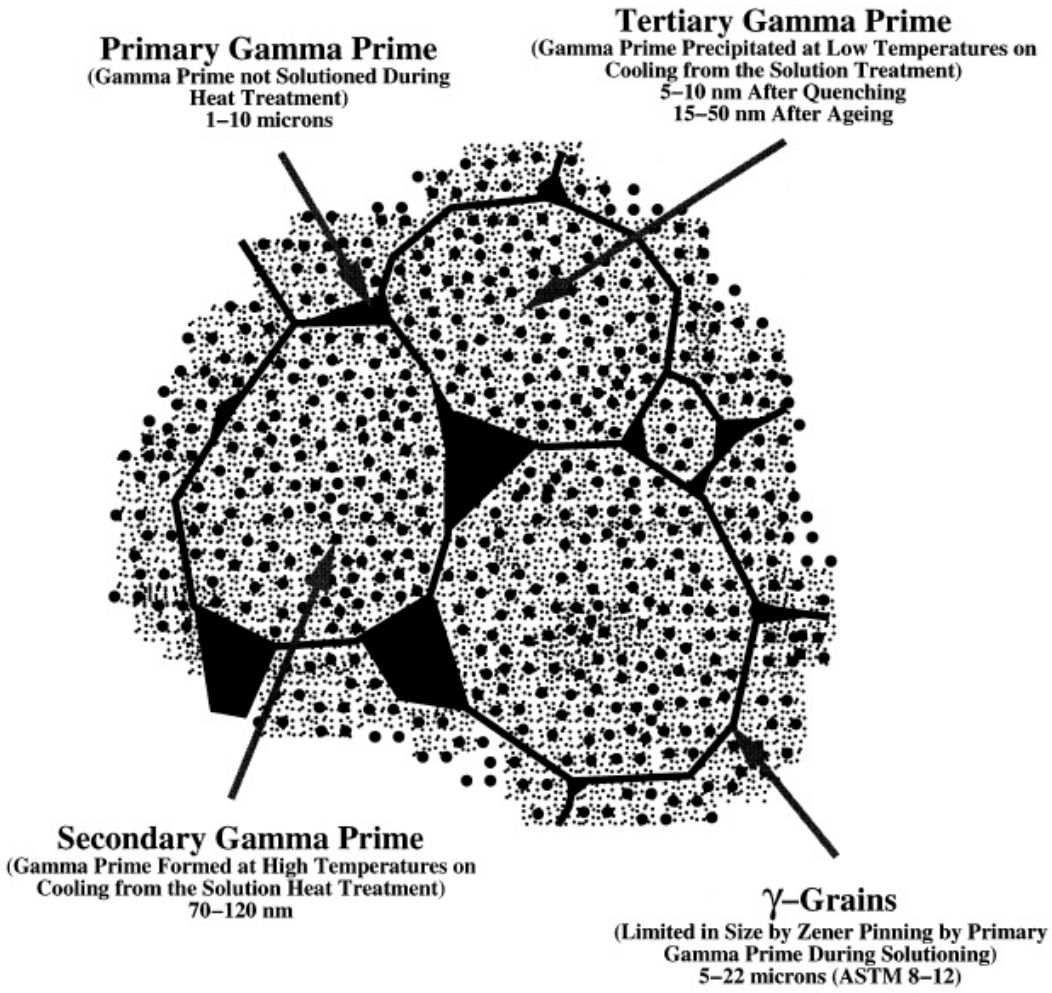

Figure 1.12: Illustration of the γ' distribution on a turbine disc alloy, [16].

In addition to primary grains, secondary and tertiary intragranular γ' is observed in turbine disc superalloys. The formation of these species is due to kinetics of nucleation, growth and coarsening during solutioning and ageing treatments. Furhtermore it was found that particular attention must be payed during cooling of the alloy after the heat treatments. This is because the equilibrium fraction of γ' grains in the γ matrix is not completely obtained during treatments, thus part of γ' nucleate during cooling.

The ageing heat treatment is usually carried out at about 700℃for several hours. This causes an age-hardening effect caused by coarsening of the tertiary γ' particles. Interestingly, the size secondary γ' particales is not altered by the ageing treatment.

It was found that the super-solvus heat treatment has a positive effect on the fatigue resistance of the alloy. In particular, this treatment causes an improvment of the fatigue crack propagation (FCP) rate that is more potent than that obtained by minor changes in the chemical composition of the alloy involving the Nb/Ti ratio or the content of Co. However, the cooling phase after the super-solvus heat treatment has a strong effect on the FCP rate. It was found that FCP rate increases if the alloy is air cooled rather than furnace cooled. This is caused by a decrease in the size of γ' particles during cooling.

In conclusion, the microstructure required to improve yield properties is the opposite of what required to enhance fatigue resistance, Figure 1.13. The first is optimized by small γ grains with primary γ' precipitates, the latter is imporved by large γ grains and the presence of secondary and tertiary γ' particles.

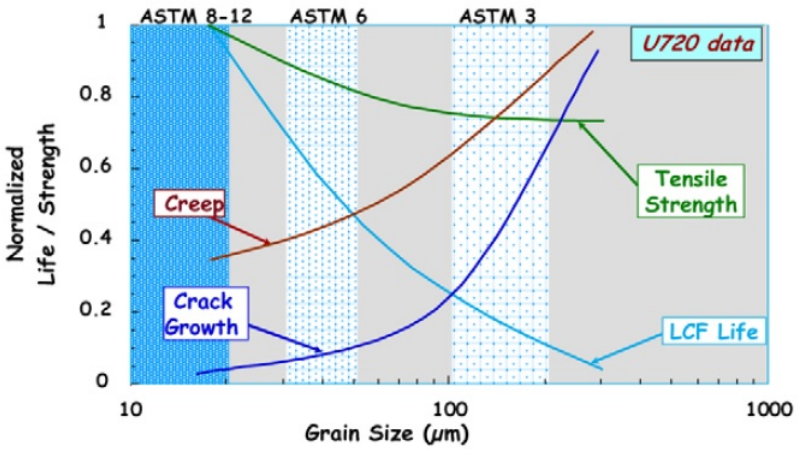

Figure 1.13: The graph shows the comparison between yield properties and fatigue resistance of a turbine disc alloy as function of the grain size, [17].

1.3.2 Criterion II: grain size

For what has been previously said, it is important to have an accurate control of the γ and γ' grain size in order to obtain the best performance from the alloy. In general, is possible to conclude that a fine grain structure is preferred if yield properties have to be optimized. On the contrary, larger grains are required if significant fatigue resistance is

desired [18]. This is not entirely true, in fact it was observed that for low cycle fatigue (LCF) fine grains structures perform better. Similarly, it has been proved that at high temperatures creep resistance is better for alloys with coarsen grains. However, fine grains structures have been seen to be more efficient at low temperatures.

These considerations led to the development of dual heat treatments in order to obtain different microstructure on the turbine disc. In particular, super-solvus heat treatment is performed in the rim, where temperatures are higher, and sub-solvus heat treatment is performed in the bore, where temperatures are lower and the alloy is subject to LCF, Figure 1.14.

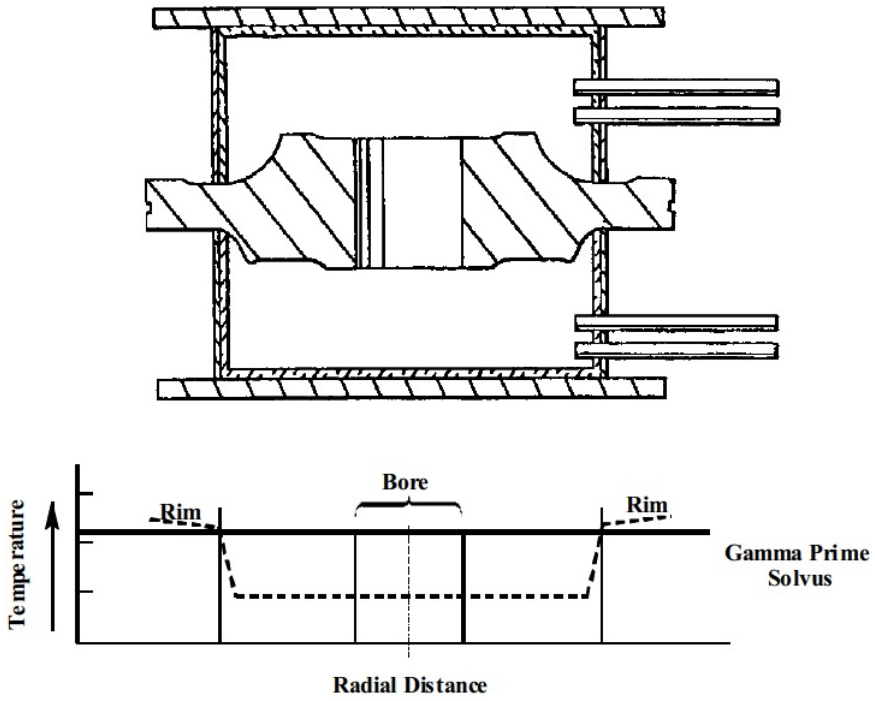

Figure 1.14: Illustration of the temperature profile during the dual heat treatment of turbine discs, [19].

1.3.3 Criterion III: grain boundary elements

Grain boundary elements such as boron and carbon can be added in small quantities in order to improve creep and LCF resistance. This is due to the segregation of these elements in γ/γ interfaces increasing the work of cohesion. However, it is important to limit the dissolution of such elements in the alloy because excessive addition leads to the formation of carbides and borides and is not beneficial for the properties. The optimum

concentrations of boron and carbon are 0.03 wt.% and 0.025 wt.% respectively. Similarly, it has been proven that the presence of small quantities of zirconium are beneficial to creep and LCF resistance [24].

1.3.4 The Udimet 720Li

The Udimet 720Li is a polycrystalline nickel based superalloy that is currently used for gas turbine disc applications, [20, 21, 22]. This alloy derives from the Udimet 720 which is a polycrystalline nickel based superalloy that was initially designed for gas turbine blades, [20]. The Udimet 720 was found to be prone to σ precipitation at elevated temperatures, especially in the subsolvus heat treated condition, so that eventually the mechanical properties are degraded [23]. For this reason, the Udimet 720Li was designed with lower content of chromium resulting a more stable alloy at high temperatures. Furthermore, the carbon and boron contents are reduced in order to promote billet homogeneity and to infer better hot working properties.

wt.%	Ni	Cr	Co	Mo	W	Al	Ti	C	B
UDIMET 720	Bal.	17.9	14.7	3	1.25	2.5	5	0.035	0.033
UDIMET 720Li	Bal.	16	15	3	1.25	2.5	5	0.025	0.018

Table 1.1: The chemical composition of the Udimet 720 and Udimet 720Li. [22].

Chapter 2

Oxidation of superalloys

2.1 External oxidation

Noble parent materials are those that form only moderately stable oxides under normal conditions so that their behaviour is similar to noble metals such as Pt, Au, Ag, etc. At reduced oxygen partial pressures, Nickel behaves as a noble parent metal.

An example of this behaviour is provided by the Pt-Ni alloy. When the system is exposed to the oxidizion atmosphere, oxygen begins to dissolve in the metal. However, the low solubility of oxygen in the platinum matrix and the moderate stability of the NiO oxide, due to the low negative value of the free standard energy of formation for this specie, prevent the internal nucleation of oxides. The result is the outward migration of Ni atoms to form a continuous external NiO layer.

When the content of nickel in the alloy is low, the diffusion of Ni atoms through the platinum matrix limits the reaction, hence this stage is rate determining. On the contrary, when the nickel content is high, Ni ions have to diffuse across the oxide scale to the oxide-gas interface where further oxide formation occurs. Thus, in this case, the diffusion through the oxide is rate determining. For a general system A-B, where A is the noble solvent and B is the solute, the content of B below which diffusion in the alloy controls the reaction ($N_B^{(O)}$) can be calculated by Equation 2.1:

$$N_B^{(O)} = \frac{V_m}{32\nu}\left(\frac{\pi k_p}{D_B}\right)^{\frac{1}{2}} \tag{2.1}$$

Where V_m is the molar volume, D_B is the diffusivity of B in the base metal, ν represents the number of oxygen ions in the BO_ν oxide and k_p is the boltzmann constant.

It was also observed that in the case of scale growth controlled by diffusion in the alloy, the oxide/metal interface can become unstable, Figure 2.1. The development of protuberances reduces the diffusion distance across the zone depleted in B beneath the oxide scale, hence such protuberances will grow further.

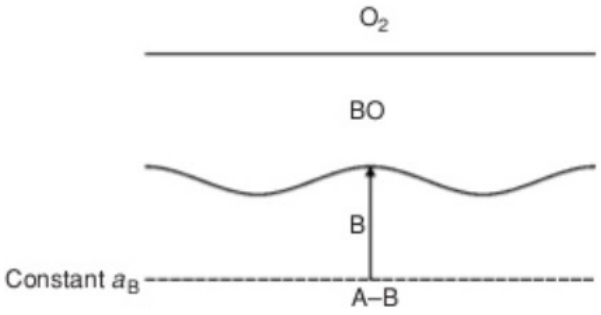

Figure 2.1: Illustration of unstable oxide/metal interface when diffusion in the alloy is rate determining, [25].

2.2 Internal oxidation

2.2.1 Conditions and mechanism

Internal oxidation is defined as the process in which oxygen diffuses into the alloy causing the internal precipitation of oxides of one or more alloying elements [26]. This phenomenon occurs only if the following conditions are satisfied:

i. The standard free energy of formation (per mole O_2) for the solute metal oxide (BO_ν), must be more negative than the free energy of formation for the solvent metal oxide.

ii. The ΔG for the reaction $B + \nu O = BO_\nu$ must be negative. This condition implies that solubility and diffusivity of oxygen in the base metal are sufficient to reach the required activity of dissolved oxygen at the reaction front.

iii. The solute concentration in the alloy must be lower than that required for the transition from internal to external oxidation.

iv. The surface layer must allow the dissolution of oxygen into the alloy at the start of oxidation.

When these conditions are satisfied, the internal oxidation occurs according to a reaction mechanism that can be divide in the following stages:

i. Oxygen dissolves in the base metal and diffuses inward through the metal matrix. The dissolution must be allowed in both the external metal surface or, if present, in the external oxide scale.

ii. Parallel to the sample surface, a reaction front is formed by the inward diffusion of oxygen and the outward diffusion of oxide forming solute. Here the critical activity product $a_B a_O^{\nu}$ is established.

iii. The internal precipitated oxide nucleates and and grows until the reaction front moves forward. This causes the depletion of the oxide forming solute arriving at the precipitate.

iv. The oxide precipitates grow further by Ostwald ripening mechanism.

2.2.2 Kinetics

It is possible to derive the internal oxidation rate for a planar specimen geometry assuming the quasi-steady-state apporximation. This apprioximation implies that the variation of dissolved oxygen across the internal oxidation zone (IOZ) varies linearly, Figure 2.2. Therefore, the oxygen flux through the IOZ, J, can be calculated using the Fick's first law, Equation 2.2.

$$J = \frac{\mathrm{d}m}{\mathrm{d}t} = D_O \frac{N_O^{(S)}}{X V_m} \tag{2.2}$$

Where $\mathrm{N}_O^{(S)}$ and D_O are the oxygen solubility and diffusivity in the base metal respectively. Assuming that the counter diffusion of solute B is negligible, the amount of oxygen accumulated in the IOZ per unit area can be calculated using the Equation 2.3.

$$m = \frac{N_B^{(O)} \nu X}{V_m} \tag{2.3}$$

Where $\mathrm{N}_B^{(O)}$ represents the initial solute concentration. From this equation is possible to derive another expression for the oxygen flux, Equation 2.4.

$$\frac{\mathrm{d}m}{\mathrm{d}t} = \frac{N_B^{(O)} \nu X}{V_m \mathrm{d}t} \tag{2.4}$$

Equating equations 2.2 and 2.4, after some manipulation, gives an expression for the penetration depth of the IOZ, X, as function of the oxidation time, Equation 2.5. It is interesting to note that the penetration depth has a parabolic dependence with time: $X \propto t^{\frac{1}{2}}$.

$$X = \left(\frac{2N_O^{(S)} D_O}{\nu N_B^{(O)}} t \right)^{\frac{1}{2}} \tag{2.5}$$

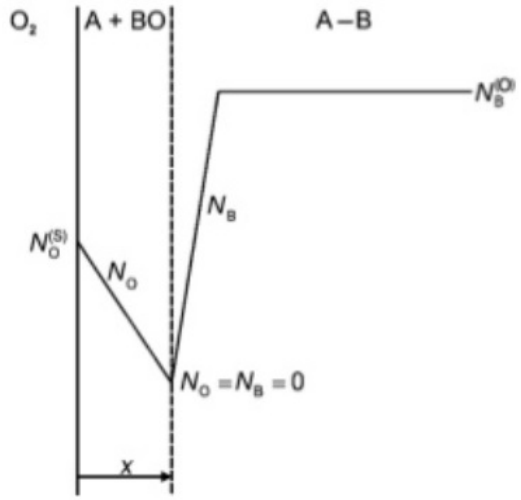

Figure 2.2: Illustration of the concentration profiles for oxygen and the solute B, in the IOZ and the underlying metal substrate, [25].

2.2.3 Precipitate morphology

The internal oxide particle size is determined by the rate of nucleation as the oxidation front passes and the susequent growth and coarsening rates of the particles. In general, a nucleated particle grows as long as oxygen and solute diffuse at its surface. This phenomen is stopped when a new particle that depletes the supply of solute nucleates. Successively, particles can coarse causing a further growth of the precipitates. Assuming that nucleation is controlled by the velocity of the oxidation front, Equation 2.6, and the growth by the available time it is possible to note that precipitate size and nucleation are inversely proportional.

$$\vec{v} = \frac{\mathrm{d}X}{\mathrm{d}t} = \frac{N_O^{(S)} D_O}{\nu N_B^{(O)}} \cdot \frac{1}{X} \tag{2.6}$$

Apparently, temperature has a poor effect on the nucleation rate, but affects more significantly the growth rate of internal oxides.

As the front of reaction increases, $\vec{v}$ decreases to a point where the diffusion of solute to the particle is rapid enough to prevent the further nucleation of new particles. At this point, the inward diffusion of oxygen occurs along the metal/oxide interface of the internal oxide particle. The combination of these effects promotes the formation of elongated or needle-like internal oxide particles [27].

The effect of particle/matrix interfacial free energy is important in the nucleation and coarsening of internal oxides. Equation 2.7 describes the free energy of formation of a nucleus of radius r.

$$\Delta G = 4\pi r^2\sigma + \frac{4}{3}\pi^3\Delta G_V \tag{2.7}$$

Where σ is the specific interfacial free energy and ΔG_V is the variation of the free energy per unit volume of the precipitate formed. Figure 2.3 shows ΔG as function of r and the effect of the two terms in Equation 2.7.

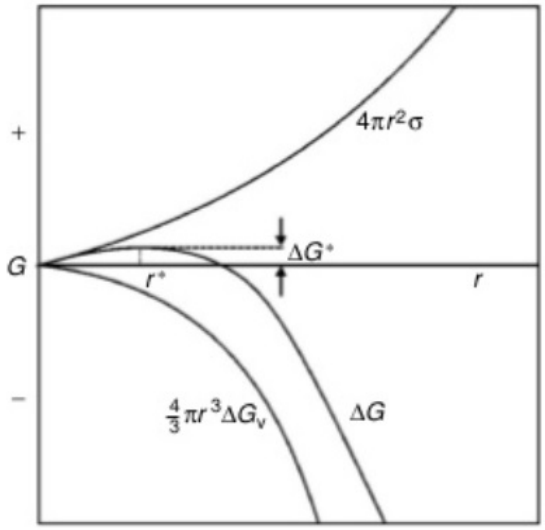

Figure 2.3: Schematic rapresentation of ΔG as function of r.

From this function is possible to note that nuclei with a radii greater than r^* will grow spontaneously. The critic radius r^* is calculated following Equation 2.8 to which corresponds the activation barrier to nucleation ΔG^*, Equation 2.9.

$$r^* = \frac{-2\sigma}{\Delta G_V} \tag{2.8}$$

$$\Delta G^* = \frac{16}{3}\pi\frac{\sigma^3}{\Delta G_V^2} \tag{2.9}$$

The activation energy barrier to nucleation influences the nucleation rate as calculated from Equation 2.10, where C_0 is the concentration of reactant molecules, C^* is the concentration of critical nucleai and ω is the frequency with which atoms are added to the critical nucleus . From this expression is possible to observe that particle size increase if ΔG^* increases, thus if the interfacial energy σ increases.

$$J = \omega C^* = \omega C_0 \exp\left(-\frac{\Delta G^*}{RT}\right) \tag{2.10}$$

In conclusion, large internal oxide formation is favoured by:

- deep penetration front, X;
- high solute concentration, $N_B^{(O)}$;
- low oxygen solubility (low p_{O_2});
- high temperature;
- high particle/matrix interfacial free energy, σ;
- oxides with low stability.

2.3 Transition from internal to external oxidation

The transition from internal to external oxidation occurs when the content of oxide forming solute in the alloy, B, is higher than a limiting concentration. In this situation, the diffusion of B will be rapid enough to allow the formation of a continuous layer of BO_ν that is able to stop the inward diffusion of oxygen, thus blocking the nucleation and growth of internal precipitates. Therefore, engineering alloys, such as nickel based superalloys, are designed to contain a sufficient amount of solute, for example Cr or Al, in order to prevent the internal oxidation. This process is also known as selective oxidation.

In Figure 2.5 a more accurate description of the compositional profiles in the IOZ is represented. In this situation, the depth of the reaction front is expressed as in Equation 2.11.

$$X = 2\gamma \left(D_O t\right)^{\frac{1}{2}} \tag{2.11}$$

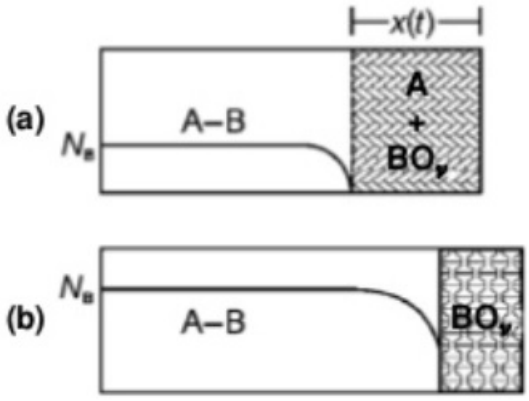

Figure 2.4: Schematic rapresentation of the transition from internal (a) to external (b) oxidation, [25].

Where γ is a proportional coefficient defined as in Equation 2.12 and θ is the diffusion coefficient ratio, $\theta = \dfrac{D_O}{D_B}$.

$$\gamma = \frac{N_O^{(S)}\sqrt{\pi\theta}}{2\nu N_B^{(S)}} \tag{2.12}$$

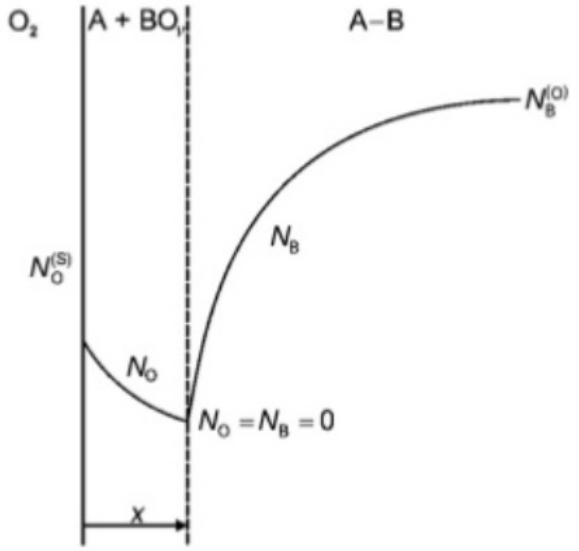

Figure 2.5: Concentration profiles for internal oxidation in a A-B system, [25].

Considering the following initial, t=0, and boundary, t=t, conditions:

$$t = 0 \begin{cases} N_B = 0 & \text{for } x < 0 \\ N_B = N_B^{(O)} & \text{for } x > 0 \end{cases} \qquad t = t \begin{cases} N_B = 0 & \text{for } x = X \\ N_B = N_B^{(O)} & \text{for } x = \infty \end{cases}$$

It is possible to solve Fick's second law, Equation 2.13. The result gives an expression of

the concentration profile for the solute B, Equation 2.14.

$$\frac{\partial N_B}{\partial t} = D_B \frac{\partial^2 N_B}{\partial x^2} \tag{2.13}$$

$$N_B(x,t) = N_B^{(O)} \left[1 - \frac{\operatorname{erfc}\left(\dfrac{x}{2(D_B t)^{\frac{1}{2}}} \right)}{\operatorname{erfc}(\gamma \theta^{\frac{1}{2}})} \right] \tag{2.14}$$

Defining with f the mole fraction of BO_ν in the IOZ it is possible to express the mole concentration per volume as f/V_m. Consequently, the number of moles in a volume element, $A\mathrm{d}X$, will be $(f/V_m)A\mathrm{d}X$, where A is the cross section area for diffusion. Equating this quantity with the number of moles of B arriving at x=X in the time dt by diffusion Equation 2.15.

$$\frac{f A \mathrm{d}X}{V_m} = \left(\frac{A D_B}{V_m} \frac{\partial N_B}{\partial x} \right) \mathrm{d}t \tag{2.15}$$

Therefore, substitution of Equation 2.11 and 2.14 in the last equation gives an expression of the enrichment factor α, Equation 2.16. The latter equivalence is explained by the different oxygen permeability between matrix and oxide, $\mathrm{N}_O^{(S)}\mathrm{D}_O \ll \mathrm{N}_B^{(O)}\mathrm{D}_B$, thus $\gamma\theta^{\frac{1}{2}} \ll 1$.

$$\alpha = \frac{f}{N_B^{(O)}} = \frac{1}{\gamma \pi^{\frac{1}{2}}} \left(\frac{D_B}{D_O} \right)^{\frac{1}{2}} \frac{\exp\left(-\gamma^2 \theta\right)}{\operatorname{erfc}\left(\gamma \theta^{\frac{1}{2}}\right)} \approx \frac{2\nu}{\pi} \left(\frac{N_B^{(O)} D_B}{N_O^{(S)} D_O} \right) \tag{2.16}$$

Hence, it is possible to conclude that when α is large the internal oxides will accumulate and grow laterally forming a continuous oxide layer. Thus the transition from internal to external oxidation occurs when the enrichment factor α is high. The volume fraction of oxide, g, is defined as follows:

$$g = f \left(\frac{V_{ox}}{V_m} \right) \tag{2.17}$$

Therefore, the transition from internal to external oxidation occurs when g reaches a critical value g^*. The substitution of f in terms of g^* in Equation 2.16 gives an expression that can be used to predict the solute concentration required to observe the transition, Equation 2.18.

$$N_B^{(O)} > \left(\frac{\pi g^*}{2\nu} N_O^{(S)} \frac{D_O V_m}{D_B V_{ox}} \right)^{\frac{1}{2}} \tag{2.18}$$

The transition from internal to external oxide is strongly affected by the presence of a second solute whose oxide has a stability intermediate between that of the base metal and the other solute. If the partial pressure of oxygen in the atmosphere is sufficiently high

to form the oxide of the second solute, the inward flux of oxygen into the base metal will decrease. Thus, the formation of the external BO_ν oxide layer will be favoured at lower concentrations of the first solute B.

2.4 Oxidation of Ni-Cr alloys

2.4.1 Transient oxidation

Considering the steady-state oxidation of a Ni-Cr binary system. When the content of solute is low, the alloy shows internal oxidation of Cr to form Cr_2O_3 precipitates surrounded by almost pure Ni. Successively, an outer scale composed of NiO develops with an inner, sometimes porous, mixed $NiO/NiCr_2O_4$ oxides layer. The outermost layer contains Cr ions in equilibrium with the $NiCr_2O_4$ phase. This provides cation vacancies therefore increasing the Ni ions mobility, hence the growth of the oxide layer.

Cation diffusion is slower in $NiCr_2O_4$ oxide rather than in NiO, thus the first phase act as diffusion block for the outward migration of Ni ions. Therefore, if the Cr content in the alloy is raised, the precipitation of $NiCr_2O_4$ will increase causing a significant reduction on the flux of Ni ions. In this situation a complete external layer of Cr_2O_3 will form.

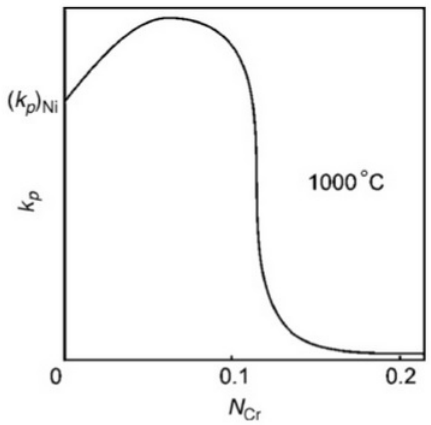

Figure 2.6: Parabolic rate constant for the oxidation of a binary Ni-Cr system as function of the Cr content in the alloy at 1000℃, [25].

In practice, since Ni oxides grow more rapidly than Cr oxides, an external $NiO/NiCr_2O_4$ can develop before the formation of the Cr_2O_3 continuous scale. This phenomenon is called transient oxidation [28], and occurs on those alloys for which the oxides of more

than one component have negative free energy variations for their formation in the given atmosphere. In Figure 2.7 the transient oxidation is represented: when the solute concentration is low the internal oxidation of B and a continuous external scale of AO is observed. On the contrary, when the content of B is sufficient, a protective Bo scale will form. However, in the latter situation, the presence of transient AO particles is observed on the top of the BO layer.

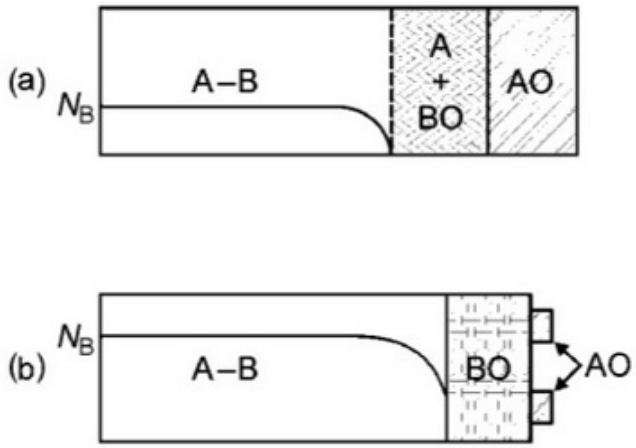

Figure 2.7: Schematic illustration of the oxidation of a A-B binary alloy: when the concentration of B is low (a) and when the content of B is raised (b), [25].

Transient oxidation is prevented by those factors that promotes selective oxidation, thus less NiO formation is observed when:

i. Cr content is high;

ii. oxygen partial pressure is low;

iii. cold-worked alloys are exposed.

2.4.2 Chromium depleted region

It is important to note that if the content of Cr is around the critical value to give transient oxidation, the protection confered by the outermost Cr_2O_3 scale may not be sufficient. In this situation, a Cr depleted region was observed in the metallic substrate beneath the continuous external oxide [29]. Here the content of Cr is below the critical concentration required for the transient oxidation. Therefore, any rupturing of the oxide scale will

expose the alloy with lower Cr to the oxidant atmosphere causing the rapid formation of NiO and increasing the oxidation reaction rate. Furthermore, if the concentration of Cr in the depleted region is below the minimum required to provide a sufficient flux of solute to the alloy/oxide interface to maintain a stable chromia layer, the Cr_2O_3 scale can break down without fracturing. For this reason, Ni-Cr systems usually contains at least 18-20 wt.% of Cr.

2.5 Alumina forming alloys

2.5.1 Oxidation of Ni-Al alloys

The oxidation behaviour of binary Ni-Al alloys can be classified as function of Al content as follows:

- 0-13 at.% (0-6 wt.%) of Al: the system will develop an internal Al_2O_3 precipitate and an external NiO scale. It is possible to observe the formation of $NiAl_2O_4$ between the internal oxides and the external layer.
- 13-31 at.% (6-17 wt.%) of Al: the formation of an external Al_2O_3 scale is initially permitted, but the growth of a continuous layer is limited by an inadequate supply of Al. This leads to the rapid formation of Ni oxides, hence the resulting oxide is a $NiO/NiAl_2O_4/Al_2O_3$ mixture.
- $\geq$31 at.% (17 wt.%) of Al: The system is able to form a continuous Al_2O_3 scale and to maintain it by a sufficient supply of Al from the metallic substrate.

Temperature has a significant effect in the oxide formation mechanism. It has been observed that higher temepratures extend the continuous Al_2O_3 region to lower Al contents, Figure 2.8. In this figure, the crosshatched regions represent variable behaviours that can be obtained varying the surface conditions of the sample.

2.5.2 Oxidation of Ni-Cr-Al alloys

The addition of Cr in a Ni-Al alloy result in a synergistic effect that led to an improvment in the design of oxidation resistant superalloys and has been widely studied [31, 32, 33].

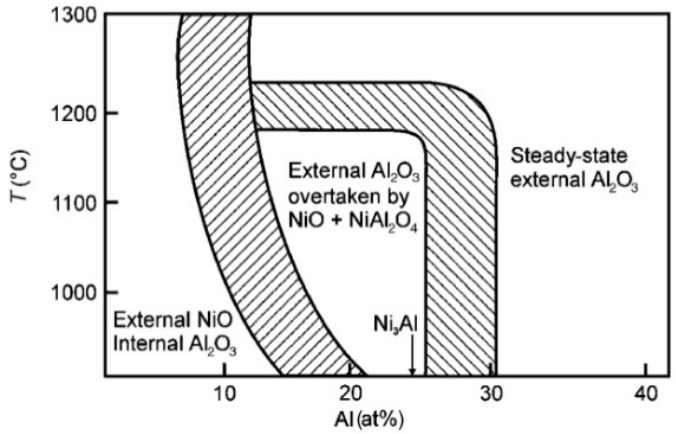

Figure 2.8: Binary Ni-Al alloys oxidation as function of Al content and temperature, [30].

For example, the addition of 10 wt.% of Cr allows the formation of a continuous Al_2O_3 external scale in an alloy with 5 wt.% of Al. The behaviour of these alloys can be summarised in oxide maps, Figure 2.9, and divided in three distinct types of oxidation:

Type I: characterised by the formation of a NiO external scale and mixed Al_2O_3/Cr_2O_3 internal oxides.

Type II: characterised by the formation of a continuous Cr_2O_3 external scale and Al_2O_3 internal oxides.

Type III: characterised by a continuous Al_2O_3 external layer only.

It is important to note that the ternary diagram in Figure 2.9 is not a thermodynamic diagram, but is based upon kinetics processes which take place during scale development. An example of the transient oxidation exhibited by a Ni-15 wt.% of Cr-6 wt.% of Al alloy is shown in Figure 2.10. Initially, the formation of a mixed $Ni(Cr,Al)_2O_4$ oxide layer and NiO grains was observed on the surface of the specimen, (a). After 5 minutes, (b), of exposure, the partial pressure of oxygen beneath the external scale is decreased promoting the formation of a more stable Cr_2O_3 subscale. The formation of Cr_2O_3 reduces the oxygen partial pressure further, hence internal Al_2O_3 particle start to form. Successively the Cr_2O_3 become continuous (c), therefore the partial pressure in the substrate is reduced and the growth of internal oxides is favoured. For longer exposure time it was observed that the internal Al_2O_3 particles could coarse to form a continuous scale which become rate controlling.

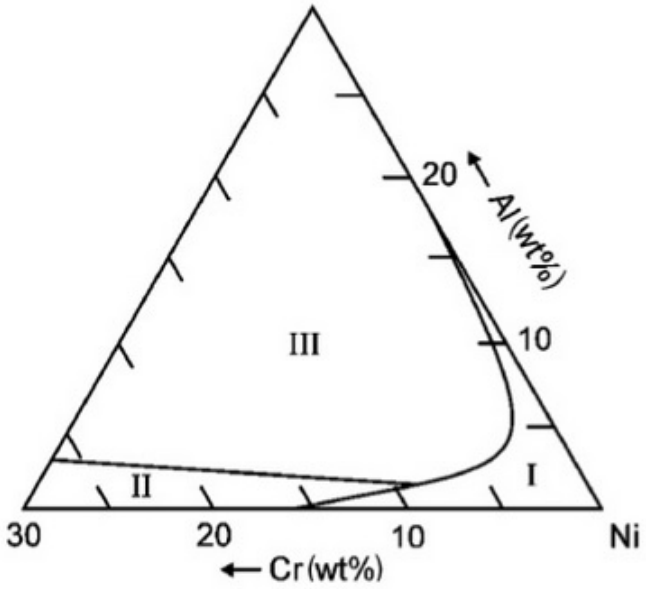

Figure 2.9: The ternary diagram proposed by Pettit et al. for the three types of oxidation behaviour of Ni-Cr-Al alloys at high temperature, [31].

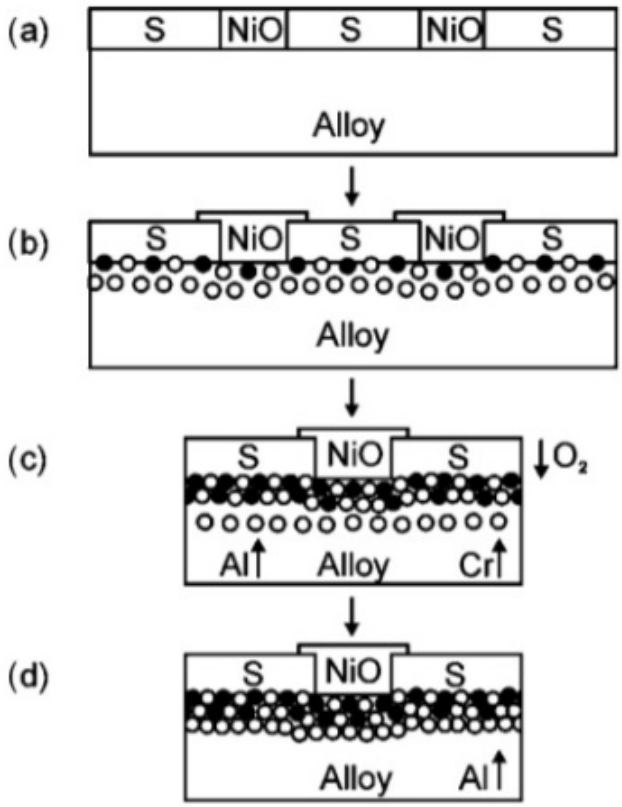

Figure 2.10: The transient oxidation of a model Ni-15 wt.% of Cr-6 wt.% of Al at 1000℃after: (a) 1 minute; (b) 5 minutes; (c) 40 minutes; (d) >40 minutes, [34]. S=$Ni(Cr,Al)_2O_4$ mixed oxide, •=Cr_2O_3, ○=Al_2O_3.

Studies of Ni-Cr-Al alloys have shown that at least 10 wt.% Cr is required to achieve Type II oxidation behaviour and that the lowest rate of oxide growth rate can be obtained with a Cr content between 24–26 wt.% in binary Ni-Cr alloys [35], or between 15–20 wt.% in more complex non-precipitation hardened alloys, [36].

2.6 Alloying with cobalt and titanium

It was observed that CoO is only slightly more stable than NiO, thus Ni-Co alloys oxidise similarly to pure nickel. Oxidation of these systems leads to the formation of an outer scale composed of mixed NiO/CoO oxide. However, the rate of oxidation results faster for alloys of this kind rather than for pure Ni, [37]. Furthermore, a segregation of cations was observed across the oxide scale as shown in Figure 2.11. Since the mobility of Co ions is higher than Ni ions, Co results concentrate near the oxide/atmospher interface. The lower actiation energy for the formation of CoO compared to NiO also contributes to segregation.

It was also observed that the presence of solute Co reduces the oxidation resistance by decreasing the time to oxide spallation, [38]

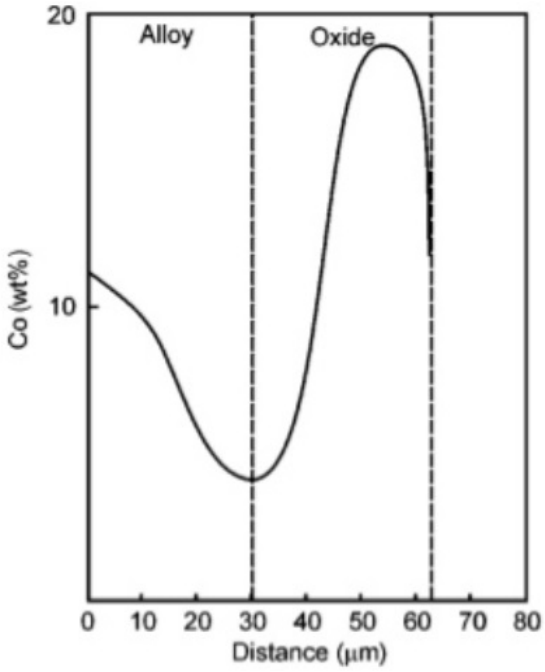

Figure 2.11: Co concentration profile across the (Ni,Co)O scale for a Ni-10.9 wt.% of Co after 24 hours at 1000℃in a 1 atm O_2 atmosphere, [37].

Ti has been reported to increase the extent of internal oxidation due to the formation of both alumina and titania and, as such, is generally thought to be detrimental to an alloys oxidation resistance, [39, 40, 41, 42].

Chapter 3

Experimental procedure

3.1 Initial samples preparation and characterization

Five model nickel-base superalloys based upon the composition of UDIMET 720Li, Table 3.1, with Cr contents of 10, 15, 17.5, 20 and 25 at.% were vacuum arc melted using elements of purity ≥99.9% to produce 50 g bars. The alloys were all solution heat treated at 1170℃for 4 hours followed by 1080℃for 4 hours. A two-step age consisting of 850℃for 24 hours and 760℃for 16 hours was subsequently applied [43].

at.%	Ni	Co	Cr	Mo	W	Al	Ti
UDIMET 720Li	Bal.	15	17.5	2	0.5	5	6

Table 3.1: The nominal composition of the alloy based on UDIMET 720Li investigated in this study.

The end of each arc melted and heat treated bar was cut at the height of ∼2 cm and mounted in conductive bakelite in order to be analysed with the SEM. The mounted ends were then polished to a 1 μm finish and etched using a water-base solution with 10% of phosphoric acid setting a 3 V on the voltage source. 2 mm slices were cut from the previously cut end of each bar in order to obtain XRD characterization samples of the as-heat treated alloys. The surfaces of the as-heat-treated XRD samples were then mechanically ground to a P600 grit.

Images of the as-heat-treated samples microstructure were obtained using a FEI Nova NanoSEM. The bulk composition of the initial samples were determined using an Oxford

Instruments EDX detector in a JEOL 5800LV SEM. The analysis of the crystal structure was conducted using a Bruker D8 DAVINCI X-ray diffractometer. Measurements of the γ' phase size and distribution were obtained from the secondary electron images using the ImageJ software package.

Figure 3.1: FEI Nova NanoSEM.

Microindentation tests on the as-heat-treated alloys were performed on the bakelite mounted samples after the SEM analysis.

The remaining bars were each sectioned to produce 7 rectilinear samples with dimensions 17 x 9 x 1.5 mm. The corners and edges of each sample were ground to 45° and the surfaces mechanically ground to a P4000 grit finish. Prior to oxidation, the rectilinear samples were immersed in ethanol and cleaned in an ultrasonic bath.

3.2 Isothermal oxidation tests and analysis

The rectilinear samples were loaded into lidded alumina crucibles and placed into a Carbolite 1100 furnace, which was subsequently heated to 800℃. Individual oxidised samples of each alloy were removed from the furnace and bench cooled after 1, 2, 3, 4, 10, 21 and 42 days, that corresponds to 24, 48, 72, 96, 240, 504 and 1008 hours respectively.

Figure 3.2: Bruker D8 DAVINCI X-ray diffractometer.

All of the samples, crucibles and samples + crucibles sets were weighted before and after oxidation and the mass change per area (Δm) was calculated as follows:

$$\Delta m = \frac{m_f - m_i}{s} \tag{3.1}$$

Where m_i and m_f are the masses of the samples before and after oxidation respectively and s is the total surface area of the sample.

Figure 3.3: Image of a sample after cutting and prior to corners and edges ground.

Secondary electron images of the outer oxide scale of each sample were obatained using a JEOL 5800LV SEM after oxidation. The oxidised samples were then sectioned without

using cooling water in order to minimise contamination. The exposed cross sections were then mounted in conductive Bakelite and polished to a 1 μm finish. Images of the oxide structure were obtained in secondary electron imaging mode using a JEOL 5800LV SEM. The spatial distributions of elements in the oxide scale were characterised by area mapping using an Oxford Instruments EDX detector in the same microscope. Images of the bulk material after oxidation were obtained in backscattered electron imaging using a Phenom ProX SEM. The surfaces of the remaining material of each oxidised sample were mechanically ground to a P2500 grit finish in order to be analysed with a Bruker D8 DAVINCI X-ray diffractometer. Measurements of the oxide thickness were obtained from electron images using the ImageJ software package.

Figure 3.4: JEOL 5800LV SEM.

Chapter 4

Results

4.1 Characterization of the alloys

The bulk compositions of the five alloys, determined by large area SEM-EDX analysis, are shown in Table 4.1. All elements are within 0.6 at.% of the nominal compositions. However it is noted that the Co concentrations were systematically ∼0.5 at.% lower than the target value of 15 at.%. Similarly, both Ti and Mo concentrations were slightly higher than their target values.

at.%	Ni	Co	Cr	Mo	W	Al	Ti
10 % Cr	Bal.	14.6	10.3	2.17	0.53	5.08	6.48
15 % Cr	Bal.	14.5	15.3	2.22	0.57	5.25	6.49
17.5 % Cr	Bal.	14.6	17.7	2.08	0.59	4.85	6.47
20 % Cr	Bal.	14.7	20.3	2.10	0.49	4.61	6.22
25 % Cr	Bal.	14.4	25.5	2.18	0.56	4.95	6.50

Table 4.1: Experimentally determined alloy compositions.

Secondary electron imaging micrographs of the as-heat-treated alloys are shown in Figure 4.1. It can be seen that the microstructure of the alloys with 10 and 15 at.% of Cr are very similar and composed of roundend secondary γ' grains with little evidence of tertiary γ' precipitation. The alloy with 17.5 at.% of Cr showed a more ordered structure composed of slightly rectangular secondary γ' grains and a substantial presence of precipitated tertiary γ' grains. The most ordered microstrucutre was shown by the alloy

with 20 at.% of Cr which showed rectangular shaped secondary γ' grains. Similarly to the sample with 17.5 at.% of Cr, a considerable prensence of tertiary γ' grains precipitation is observable. A massive presence of intermetallic phase precipitation was observed in the alloy with 25 at.% of Cr. This led to a very irregular structure where there was only a little evidence of the precipitation of secondary and tertiary γ' grains.

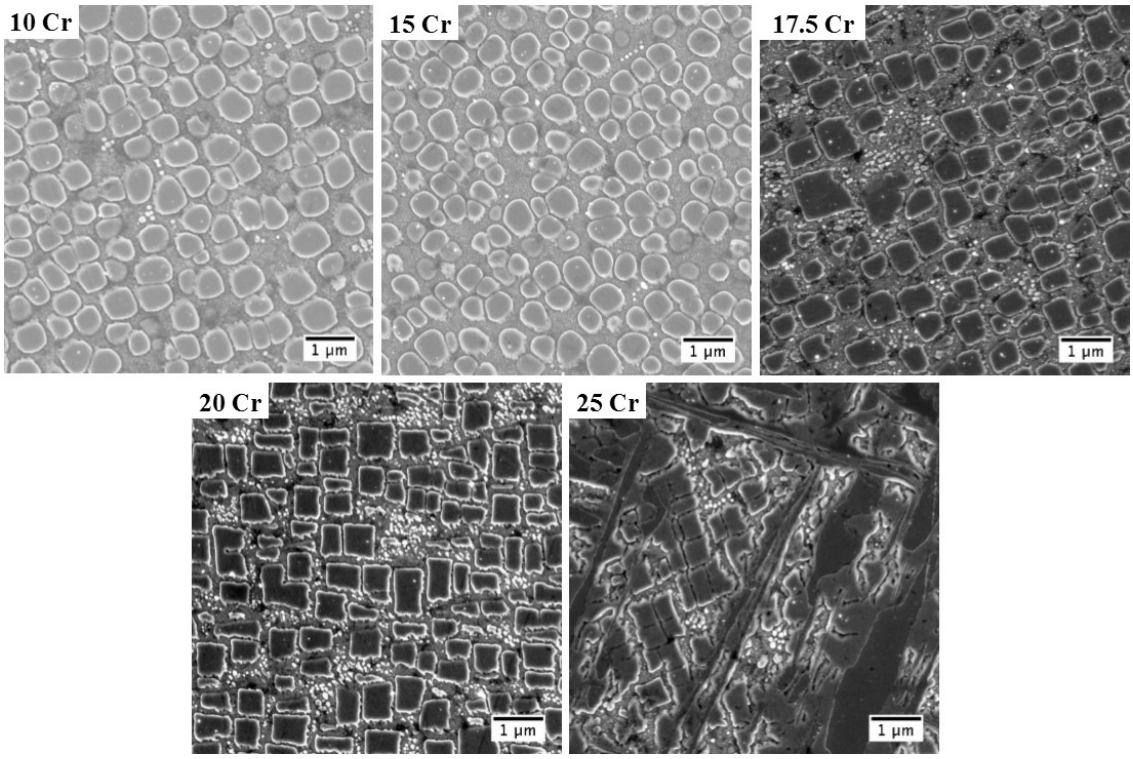

Figure 4.1: SEI micrographs of the five alloys as heat treated.

Measurements of the γ' phase size and distribution highlighted what was observable from the secondary electron micrographs, Table 4.2. Values corresponding to the alloy with 25 at.% of Cr were not estimated because of the massive presence of precipitated intermetallic phase in the microstructure. The concentration of secondary γ' was higher in the alloys with 10 and 15 at.% of Cr, whereas the tertiary γ' was seen to be less. The sample with 17.5 at.% of Cr showed a greater precipitation of tertiary γ' that increased further in the alloy with 20 at.% of Cr. The total amount of γ' phase in the bulk, secondary and tertiary, was seen to be constant for compositions up to 17.5 at.% of Cr, but resulted higher in the alloy with 20 at.% of Cr because of the increase in the quantity of tertiary γ' precipitated. The size of γ' particles was seen to be constant in all the alloys with an average diameter that varies from 0.55 to 0.69 μm for the secondary and from 0.11 to

0.17 μm for the tertiary. Secondary γ' grains roundness decreased as the Cr content in the alloys increased.

	Secondary γ'			Tertiary γ'		Total
at.% of Cr	Area %	Size μm	Roundness	Area %	Size μm	%
10	56.10	0.66	0.78	1.96	0.17	58.06
15	58.55	0.55	0.80	0.50	0.11	59.06
17.5	54.91	0.64	0.74	2.90	0.13	57.82
20	54.12	0.69	0.63	7.77	0.15	61.89

Table 4.2: Secondary and tertiary γ' size and distribution estimated using the ImageJ software package.

XRD patterns of the five alloys as-heat-treated are shown in Figure 4.2. The X-ray diffraction characterization proves the precipitation of γ' in all the materials and the presence of the intermetallic σ phase in the alloy with 25 at.% of Cr. Diffraction crystallographic planes and the related angles for the γ' phase are listed in Table 4.3. Diffraction peaks at 42.5°, 44.0°, 46.0°, 48.0°, 49.0°, 50.0°, 51.0°, 52.0°, 58.0°, 75.0°, 78.0° and 79.0° are representative of the σ phase.

γ'			
2θ	h	k	l
42.3°	1	1	1
52.5°	2	0	0
74.0°	2	2	0
90.0°	2	2	0

Table 4.3: Crystallographic diffraction planes and angles of the γ' precipitated phases.

Microindentation hardness measurments on the as-heat-treated samples are shown in Figure 4.3. For the alloys to up to 20 at.% of Cr the hardness values were similar, with a maximum of approximately 370 HV for the alloy with 20 at.% of Cr. The precipitated σ intermetallic phase conferred a hardenss of approximately 529 HV to the alloy with 25

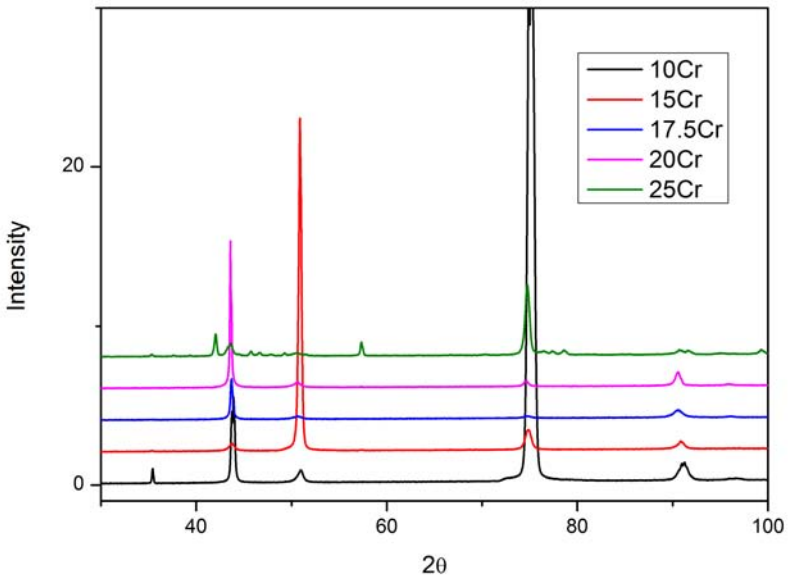

Figure 4.2: XRD patterns of the five alloys as-heat-treated.

at.% of Cr, that was considerably higher compared to the hardness recorded by the other samples.

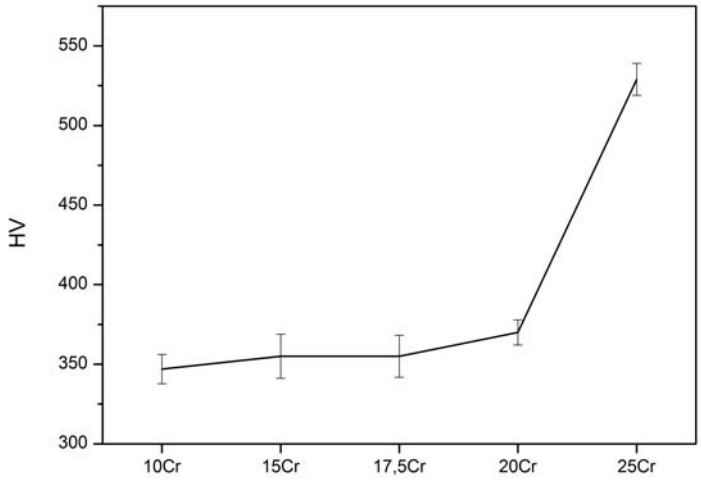

Figure 4.3: Microindentation hardness measured on the alloys of the present study.

4.2 Mass change per unit area

The mass changes per unit area, obtained using Equation 3.1 with the initial mass and that after each thermal exposure, are shown as a function of exposure time in Figure 4.4. For all exposure times, the greatest mass change per unit area was recorded for the alloy with 10 at.% Cr. This alloy exhibited an approximately linear increase in mass with exposure time and, after 42 days, the mass had increased by approximately 9 mg/cm^2. Approximately linear oxidation kinetics were also shown by the alloy with 15 at.% Cr, albeit with smaller mass gains being recorded at each time interval and a final mass change of 6.5 mg/cm^2 after 42 days. The alloys with 17.5 and 20 at.% Cr exhibited similar mass changes per unit area over the 42 days of oxidation testing. Their associated mass changes per unit area followed an approximately parabolic behaviour culminating in final mass changes per unit area of ∼1 mg/cm^2. The alloy with 25 at.% Cr also showed parabolic kinetics, although, the final mass change per unit area after 42 days was approximately twice that of the alloys with 17.5 and 20 at.% Cr, being just under 2 mg/cm^2.

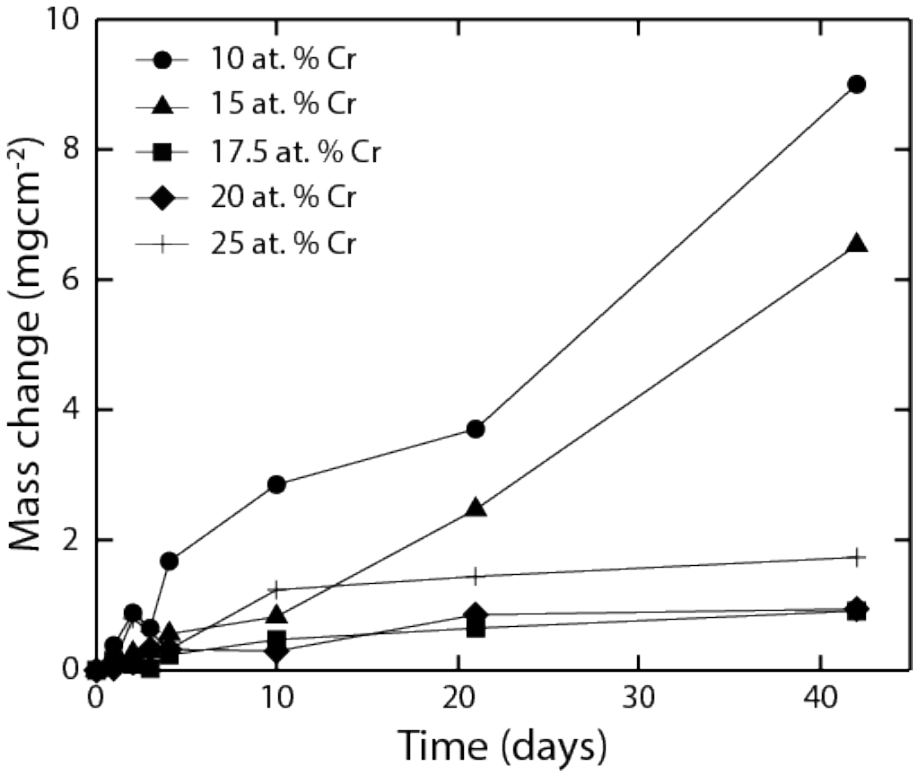

Figure 4.4: Mass change per unit area of the five experimental alloys following isothermal oxidation at 800℃in air for durations up to 42 days.

4.3 Outermost oxide scales

Secondary electron images of the external oxide scale revealed the different behaviour of the five alloys after oxidation for up to 42 days. Figure 4.5 shows the external oxide growth in the alloy with 10 at.% of Cr. It should be noted that the image of the sample exposed for 42 days does not include the external oxide due to complete spallation from the surface prior to microstructural examination. Evidence of partial spallation was also observed from 10 days of exposure onwards. However, sufficient amounts of the oxide scale remained adherent after 10 and 21 days to permit microstructural examination. Similarly to what showed by the other alloys, a fine grain external scale was observed for this composition from 1 to 3 days. For longer exposure times, a more compact scale associated with larger oxide grains was observed. The growth of the grains cuminated in the largest and most compact oxide scale showed by this alloy after 21 days of exposure.

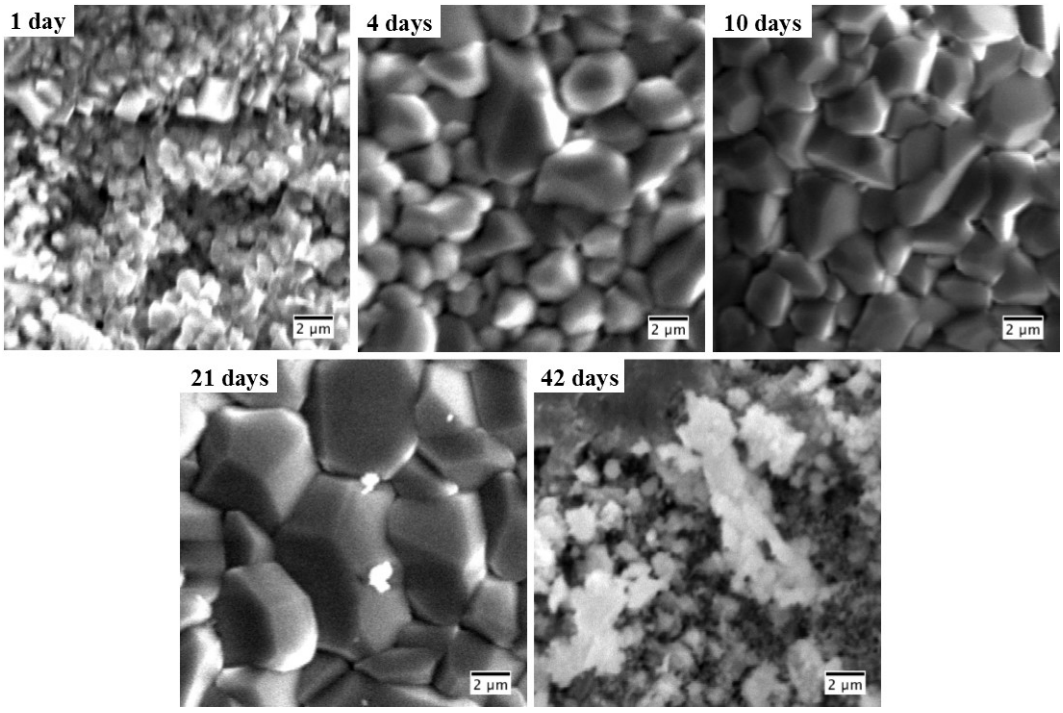

Figure 4.5: SEI micrographs of outermost external scale for the alloy with 10 at.% of Cr for up to 42 days of exposure time at 800℃in air.

The alloy with 15 at.% of Cr developed a fine grain structure for up to 4 days of oxidation, Figure 4.6. The sample exposed for 10 days exhibited a mixed scale composed of both fine and coarsed oxide grains. The alloys oxidised for 21 and 42 days appeared to have a compact scale composed of larger oxide grains similar to that developed in the alloy

with 10 at.% of Cr from 4 to 21 days of exposure time.It should be noted that evidence of partial spallation was also observed for this composition in the samples oxidised for 21 and 42 days.

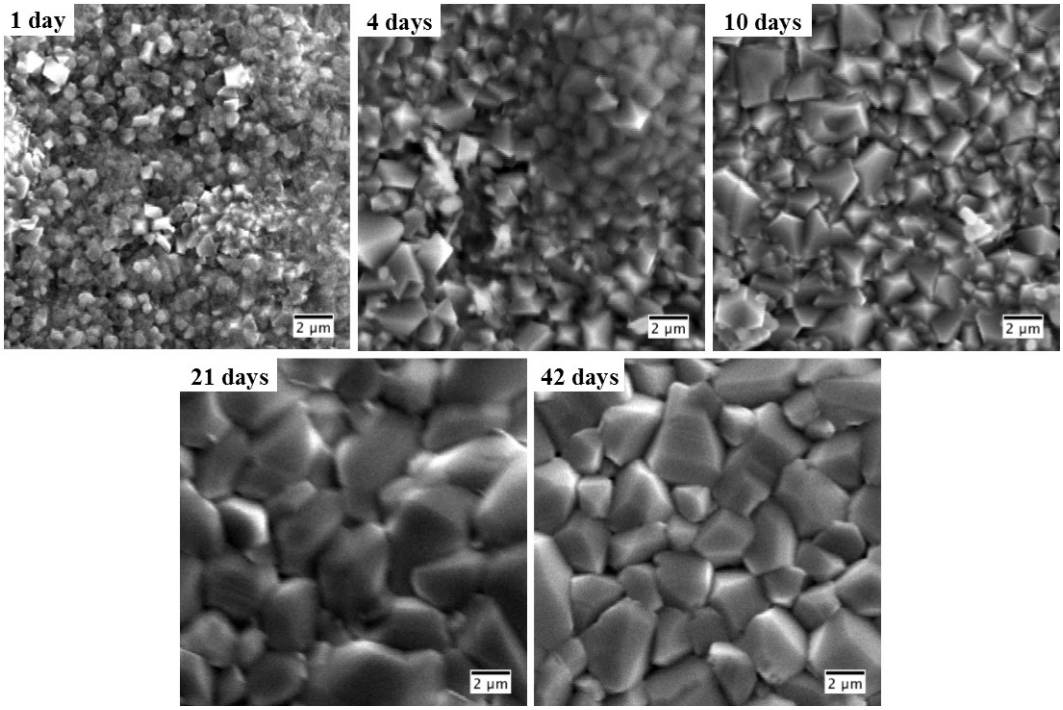

Figure 4.6: SEI micrographs of outermost external scale for the alloy with 15 at.% of Cr for up to 42 days of exposure time at 800℃in air.

The alloys with 17.5 and 20 at.% of Cr exhibited a very similar behaviour for up to 10 days of exposure, Figures 4.7 and 4.8. The alloy with 17.5 at.% of Cr displayed a fine grain external oxide scale for the entire range of exposure times, whereas the alloy with 20 at.% of Cr developed a different external oxide scale from 21 to 42 days. Whilst the morphology was seen to be very similar to those of the alloys with 10 and 15 at.% of Cr after long exposure times, the oxide grains appeared smaller. However, the compact structure of the external scale was again observed on the samples with 20 at.% of Cr oxidised for more than 21 days.

Figure 4.9 shows the evolution of the external oxide scale in the alloy with 25 at.% of Cr. This material developed a fine grain external scale from 1 to 4 days of exposure, similarly to what exhibited by the alloys with lower Cr content. From 10 days of oxidation onwards, a more compact oxide developed on the surface of the samples. The morphology of the external scale after 10 days of exposure appeared very similar to that observed on

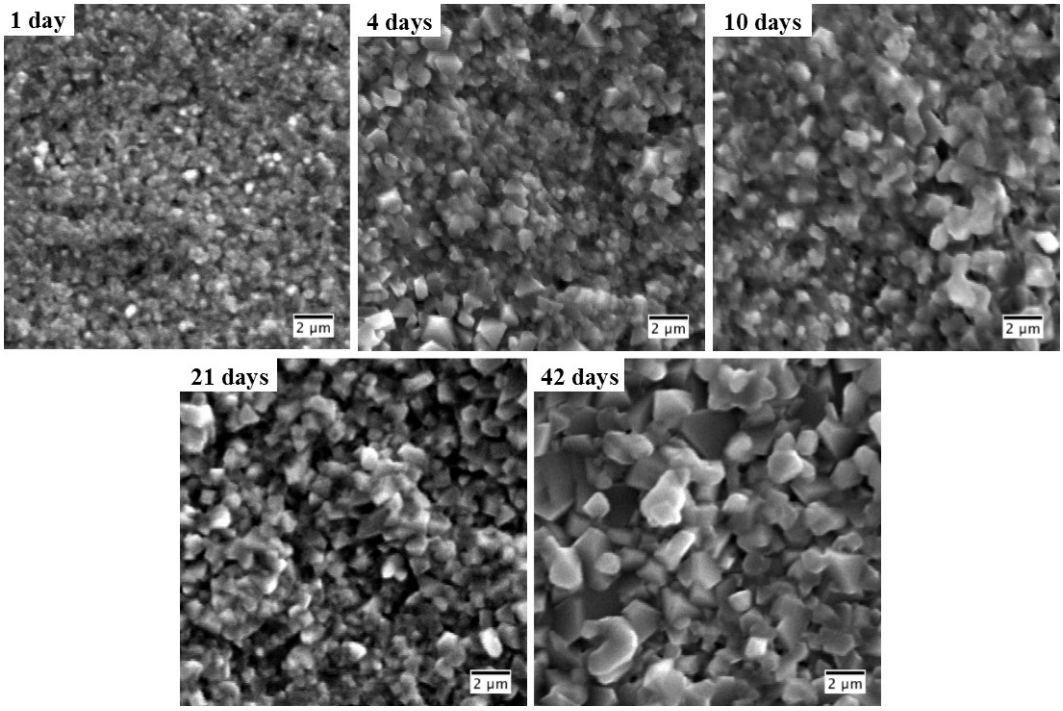

Figure 4.7: SEI micrographs of outermost external scale for the alloy with 17.5 at.% of Cr for up to 42 days of exposure time at 800℃in air.

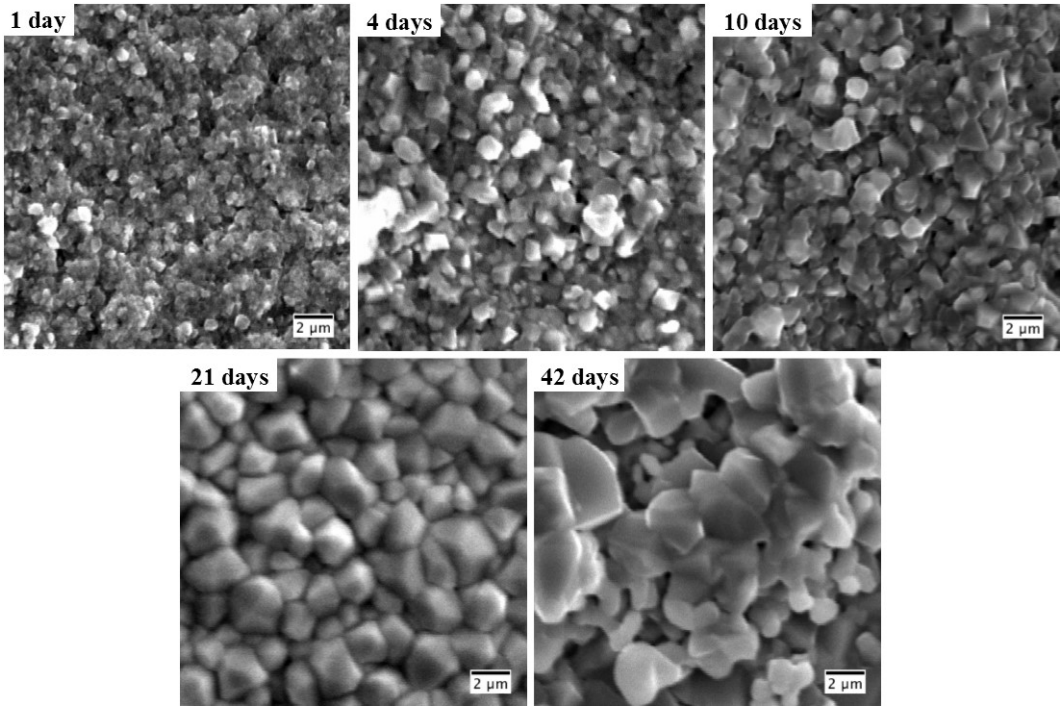

Figure 4.8: SEI micrographs of outermost external scale for the alloy with 20 at.% of Cr for up to 42 days of exposure time at 800℃in air.

the alloy with 20 at.% of Cr after 21 days.

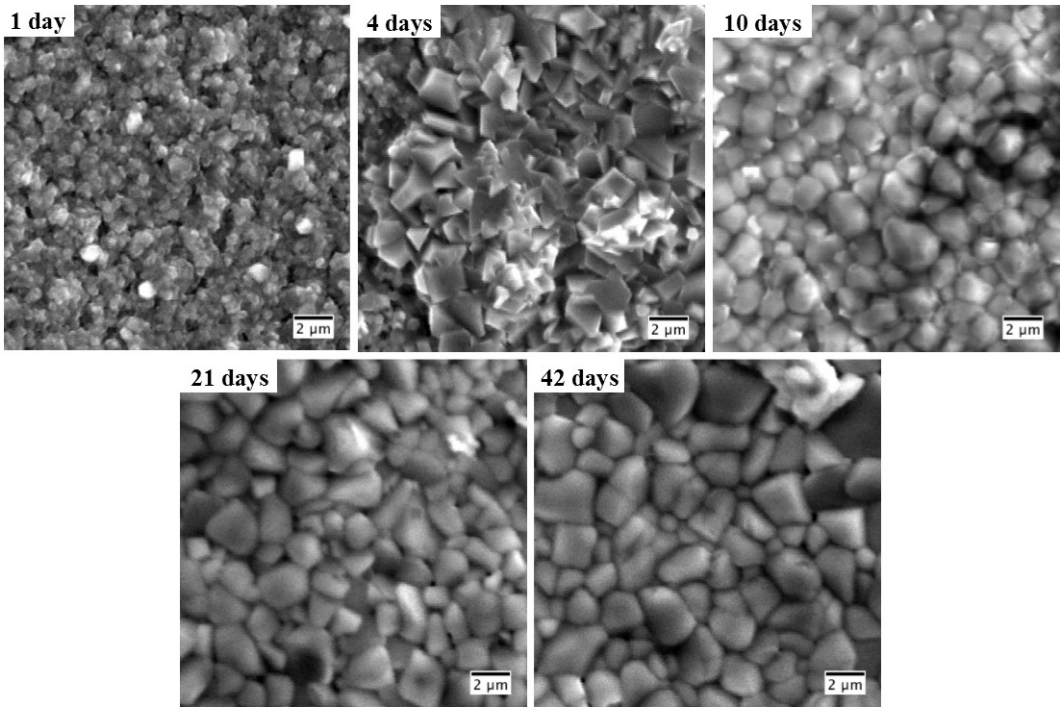

Figure 4.9: SEI micrographs of outermost external scale for the alloy with 25 at.% of Cr for up to 42 days of exposure time at 800℃in air.

4.4 Cross sections

SEI micrographs of the cross section of each alloy after exposure for 1, 2, 3, 4, 10, 21 and 42 days are shown in Figure 4.10. For the alloy with 10 at.% Cr, Figure 4.10a, it can be seen that a continuous external oxide scale has formed, the thickness of which increased up to 21 days of exposure. A marked difference in the morphology of the oxide following exposure for 3 and 4 days can be observed. Through this period an additional top scale develops, composed of vertically growing grains, which became more pronounced for the longer exposure times. Beneath this layer, an extensive oxidised region formed, under which oxide fingers penetrated further into the substrate.

The oxide scales formed on the alloy with 15 at.% Cr, Figure 4.10b, were morphologically similar to those produced on the alloy with 10 at.% Cr. However, the rate of oxide growth on this alloy was considerably slower across the range of exposure times. As with the alloy with 10 at.% Cr, a columnar oxide over-scale was observed to develop

and thicken over the longer exposure times, accompanied by subscale internal oxidation. However, oxide fingers were not observed to form at the base of the internally oxidised region, instead they adopted a more continuous globular morphology. Whilst, these microstructural changes were also observed to occur after 3 days, the transition is harder to identify as the sections examined after 4 days of exposure showed anomalously thicker oxide scales than that after 10 days.

After isothermal oxidation for up to 4 days, the alloy with 17.5 at.% Cr displayed a thin, continuous and compact external oxide layer that increased in thickness over that period. Beneath this layer a thin mixed oxide layer was observed with limited internal penetration of one of the constituents into the substrate. As with the previously described alloys, significant changes were observed following the longer duration exposures. Whilst the external oxide layer continued to slowly thicken, in line with the parabolic growth kinetics observed for this alloy, the depth to which the internal oxide fingers penetrated increased markedly, extending to $\sim$10 μm below the mixed oxide layer.

The alloy with 20 at.% of Cr, Figure 4.10d, initially formed a thin, compact, external oxide scale, with evidence of a mixed oxide sub-scale, both of which slowly increased in thickness between 1 and 4 days of exposure. This oxide morphology was very similar to that seen for the alloy with 17.5 at.% Cr over the same time period. However, following longer exposures, the external oxide scale thickened more rapidly than the alloy with 17.5 at.% Cr, and the formation of a columnar oxide top scale layer was observed. Whilst internal oxide fingers were again observed after 10 days, their extent was less than the alloy with 17.5 at.% Cr and, notably, after 21 and 42 days of exposure the oxide fingers adopted a more globular morphology.

Figure 4.10e shows that the layers present in the oxide scale of the alloy with 25 at.% Cr were similar to the 20 at.% Cr alloy, albeit with increased layer thickness, as shown by the change in magnification of the images provided. As with the other alloys, a small increase in the thickness of the oxide was observed from 1 to 4 days of exposure. From 4 to 10 days of exposure, a large increase in the thickness of the external oxide layer was seen, along with the development of a top scale. However for longer exposure times, beyond 10 days, the external oxide thickened more slowly.

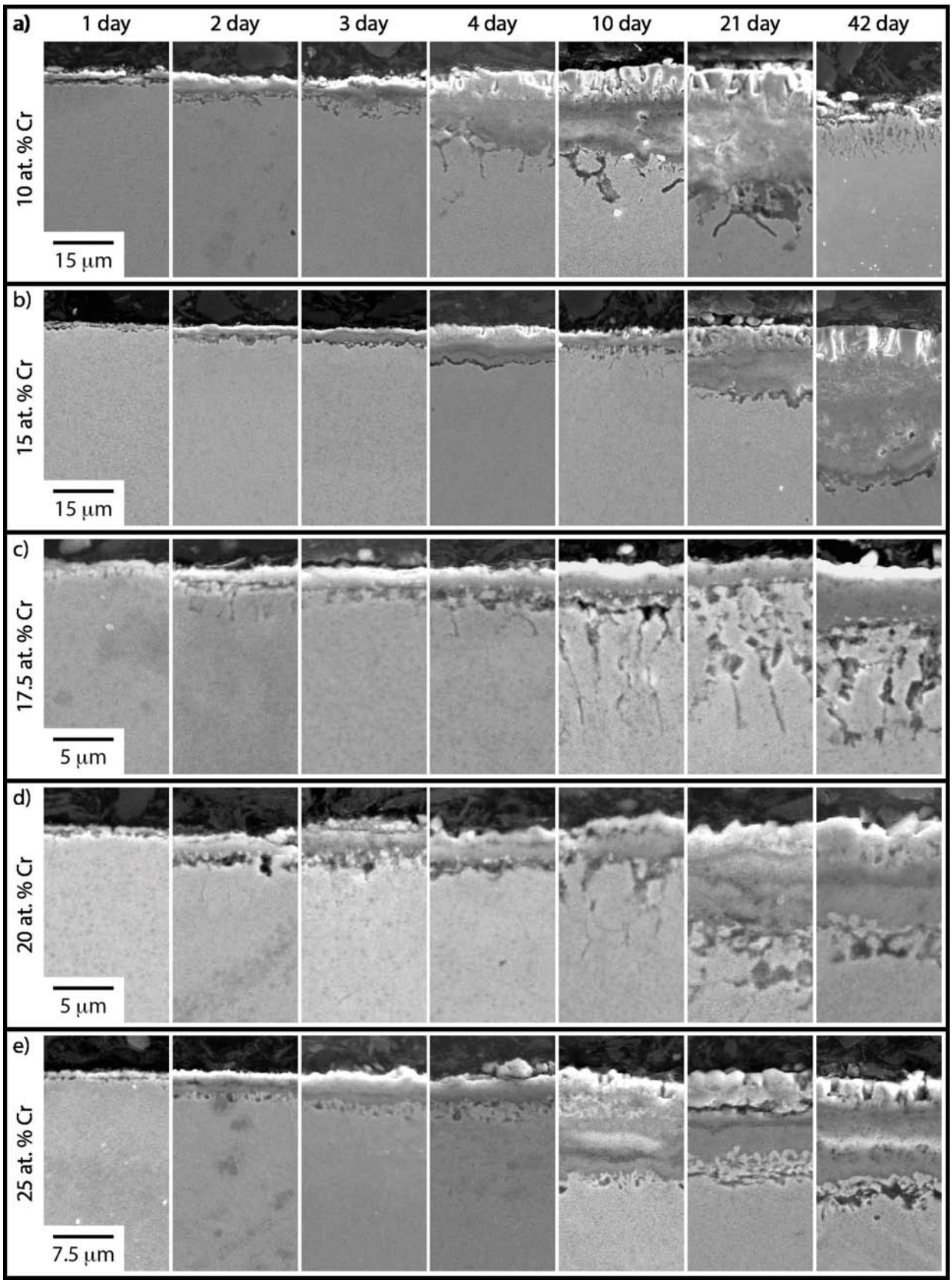

Figure 4.10: SEI micrographs of the oxide scale of each alloy after isothermal exposure at 800℃in air for up to 42 days.

4.5 External oxide thickness and internal damage penetration

The thickness of the external oxide scales and the depth of internal damage, determined from the micrographs for the five alloys following oxidation, are presented in Figure 4.11a and Figure 4.11b respectively. In general, the extent of damage described by these two measurements is correlated, and they are also consistent with the mass gains per unit area shown in Figure 4.4.

The alloys with 10 and 15 at.% Cr exhibited the greatest mass changes per unit area following oxidation, and this behaviour was reflected in the measurements of the external oxide thickness and internal damaged layers. The alloy with 10 at.% Cr exhibited an oxide thickness of 32 μm and internal damage to a depth of 17 μm after exposure for 21 days. Measurements from this alloy after 42 days were not possible as complete spallation of the oxide had occurred and, as such, any data acquired would not be directly comparable with measurements made from the other alloys. The thicknesses of the external oxide scales and internal damage regions of the alloy with 15 at.% Cr were approximately half those of the alloy with 10 at.% Cr after similar exposure times. As was noted previously, an anomalously thin oxide was produced on the surface of the alloy with 15 at.% Cr after oxidation for 10 days. This was also associated with comparatively deep internal damage penetration into the alloy, Figure 4.11.

The alloys with 17.5 and 20 at.% Cr showed the thinnest external oxide scales and behaved in a similar manner, Figure 4.11a. The maximum measured external oxide scale thickness was $\sim$5 μm after 42 days of exposure for both alloys. However, an important difference can be identified when examining the extent of internal damage penetration, Figure 4.11b. The alloy with 17.5 at.% Cr exhibited the second deepest internal penetration measured, after that from the alloy with 10 at % Cr. In contrast, the alloy with 20 at.% Cr showed very small depths of internal oxide penetration over the range of exposure times, with a maximum penetration of $\sim$6.5 μm after 42 days of exposure.

Interestingly, the alloy with the highest Cr concentration, of 25 at.%, did not exhibit the greatest resistance to oxidation. Instead, the thicknesses of the external oxide scales were intermediate between those of the alloys discussed above, Figure 4.11a, being approximately one third of that measured from the alloy with 15 at.% Cr, and approximately

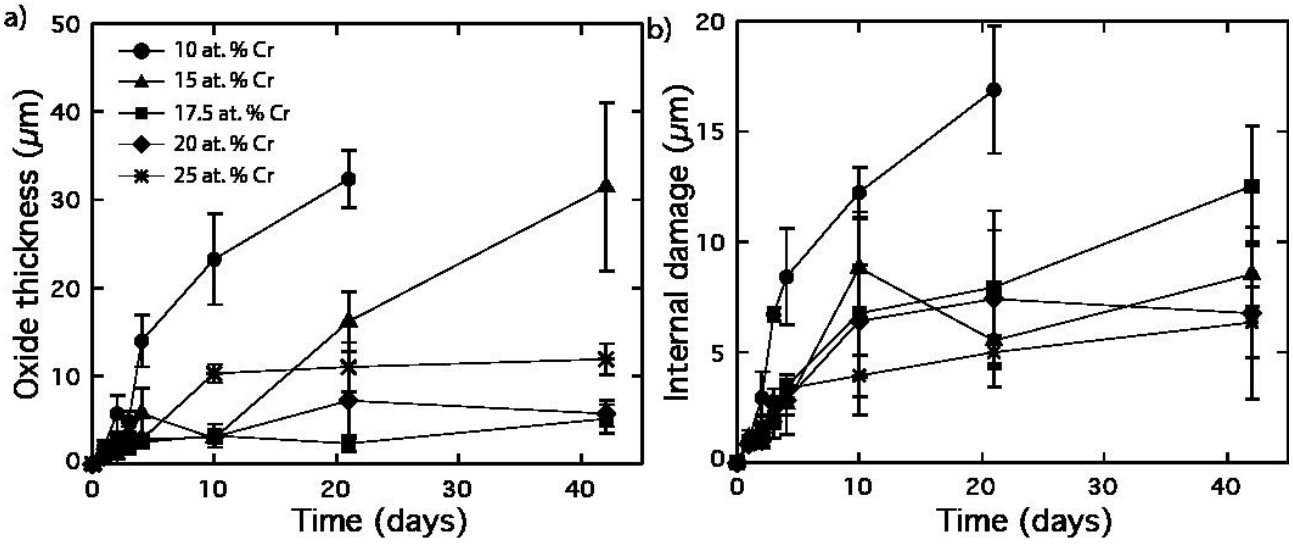

Figure 4.11: Measurements of oxide thickness and internal penetration depth of the five alloys following thermal exposure.

twice that of the alloys with 17.5 and 20 at.% Cr. However, Figure 4.11b shows that the alloy with 25 at.% Cr was the most resistant to internal damage penetration across the range of exposure times studied, with only $\sim$6 μm of penetration measured after oxidation for 42 days.

4.6 Characterization after oxidation for 42 days

The characterization of the five alloys after 42 days at 800℃was carried by X-ray diffraction and backscattered electron imaging (BSI). Investigation with XRD revealed that the internal microstructure of the materials has not changed for the alloys with less than 20 at.% of Cr after oxidation for up to 42 days, Figure 4.12. Patterns resulted comparable to those obtained during the initial charcterization, Figure 4.2, and proves that intermetallic phases precipitation were absent. Similarly, the microstrucuture of the alloy with 25 at.% of Cr has not changed during the experiment. The presence of precipitated TCP phases appared unvaried compared to initial stage XRD patterns. The alloy with 20 at.% of Cr showed the presence of diffraction peaks in the 40-60° diffraction angles range, Figure 4.13. The equivalent position of the extra peaks for the alloys with 20 and 25 at.% of Cr suggests the precipitation of σ phase in both these alloys.

Microstructural changes in the five alloys are shown by the BSI micrographs, Figure

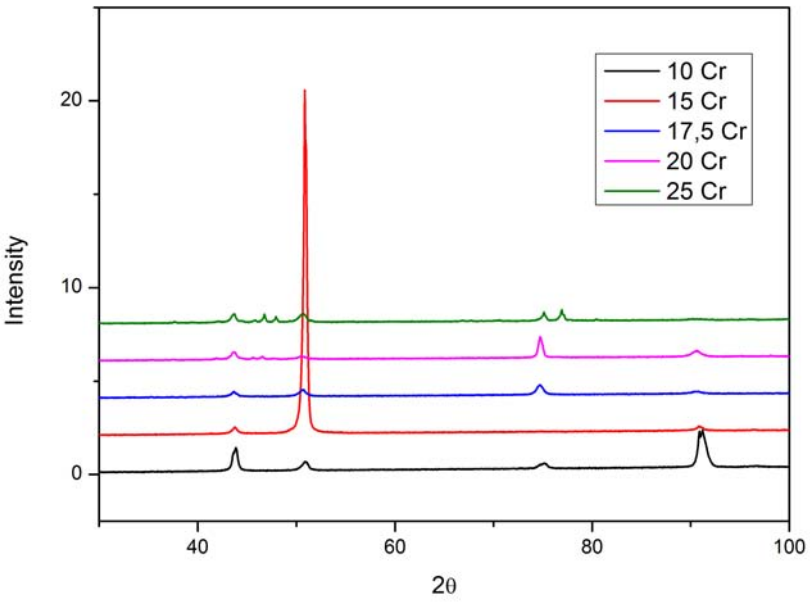

Figure 4.12: XRD patterns of the five alloys after oxidation for 42 days at 800℃.

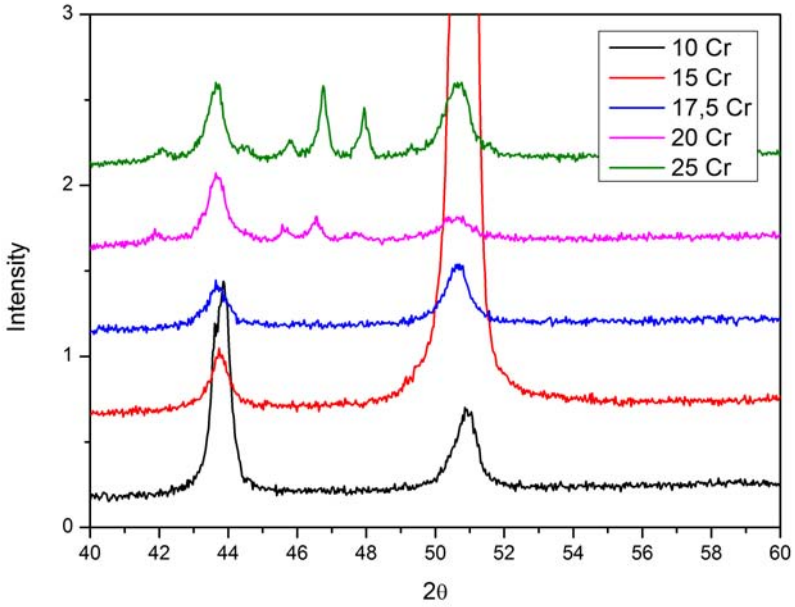

Figure 4.13: Magnification of the diffraction peaks for the five alloys after 42 days of exposure in the 40-60° diffraction angles range.

4.14. The alloys with 10, 15 and 17.5 at.% of Cr exhibited a similar internal structure composed of secondary γ' grains that were more squared compared to what observed by the intial stage micrographs, Figure 4.1. In line with the results of the XRD measurments, there is no evidence of precipitated TCP phases in these alloys. Coherently with the X ray analysis, the micrograph of the alloy with 20 at.% of Cr revealed the presence of intermetallic phases after the oxidation for 42 days. Secondary γ' grains have not changed during the experiment and the morphology appared squared and similar to that of the as heat treated samples. The alloy with 25 at.% of Cr showed a different microstructure with large intermetallic TCP phase grains with a reduced amount of secondary γ' grains. Interestingly, no evidence of tertiary γ' grains was observed in the alloys for each composition.

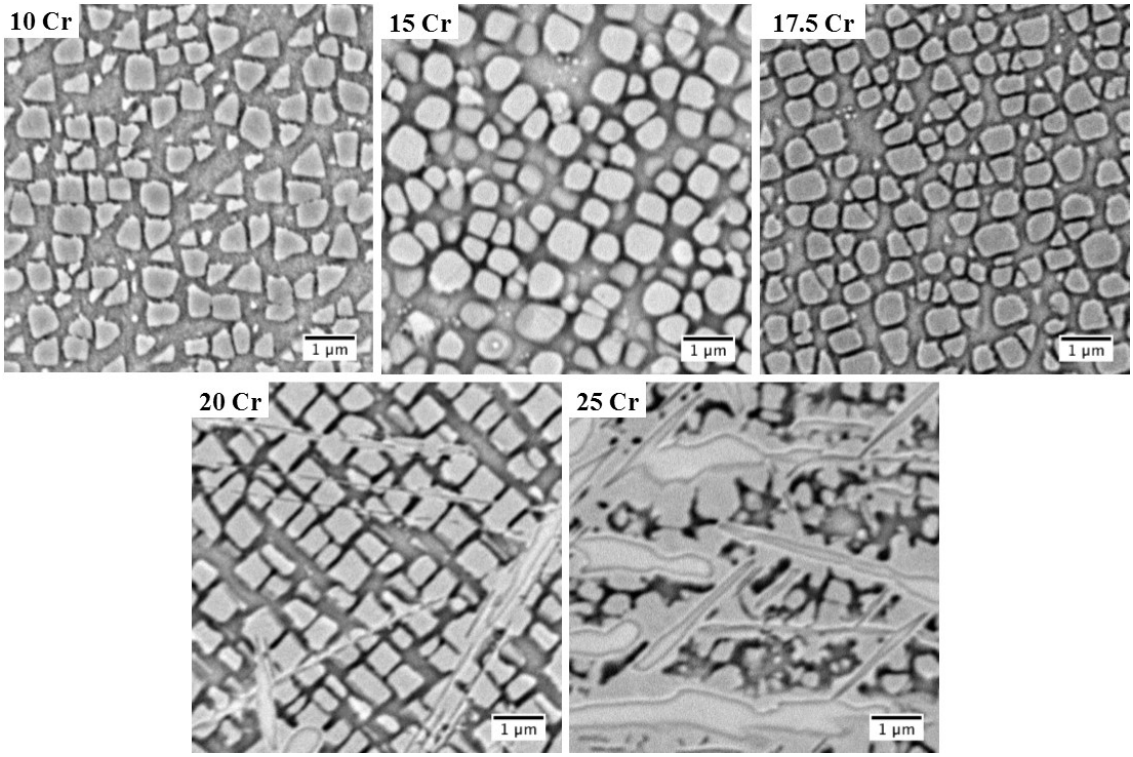

Figure 4.14: BSI micrographs of the five alloys after oxidation for 42 days at 800°C.

In order to understand the mechanism of TCP phases precipitation in the alloy with 20 at.% of Cr, other XRD measurment were carried for less than 42 days of oxidation time exposures. The analysis revealed that intermetallic phases first appeared after 21 days of oxidation, Figure 4.15. The presence of diffraction peaks at 42.5°, 46° and 48°, exhibited also after 42 days of oxidation and by the alloy with 25 at.% of Cr, suggests the presence

of σ phase. X-ray diffraction patterns after 10 days or less showed the nonexistence of TCP phases in the alloys with up to 20 at.% of Cr.

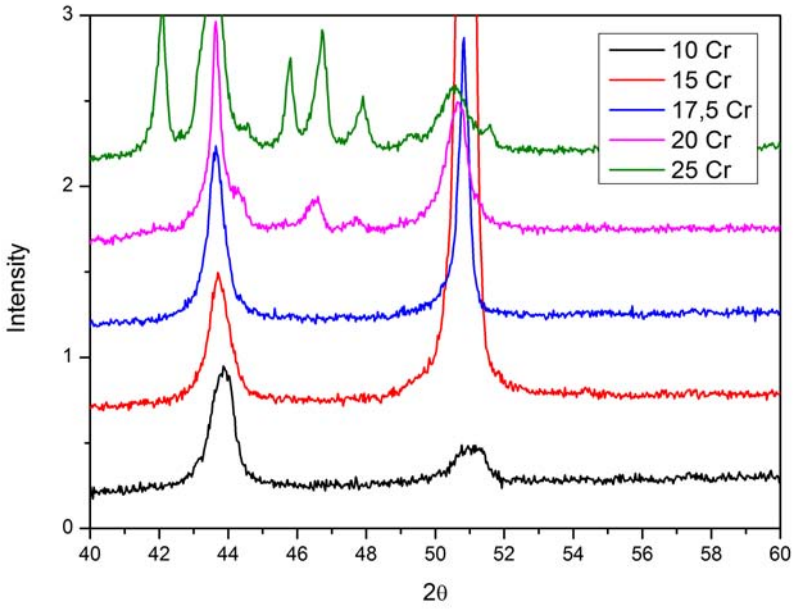

Figure 4.15: Magnification of the diffraction peaks for the five alloys after 21 days of exposure in the 40-60° diffraction angles range.

Evidence of TCP phases in the microstructure of the alloy with 20 at.% of Cr were observed by the BSI micrographs after oxidation between 10 and 42 days, Figure 4.16. It is possible to observe the presence of intermetallic phase in the sample oxidized for 10 days that was not detected by the XRD analysis. This could be attributed to the low concentration of TCP phase grains that led to a diffraction signal that was beyond the sensitivity of the instrument. Micrographs of the samples oxidized for less than 10 days have not exhibited the presence of intermetallic phase precipitation. Tertiary γ' particles were seen to be present in the alloy for up to 10 days of oxidation, but there is no evidence of this phase for longer exposure time.

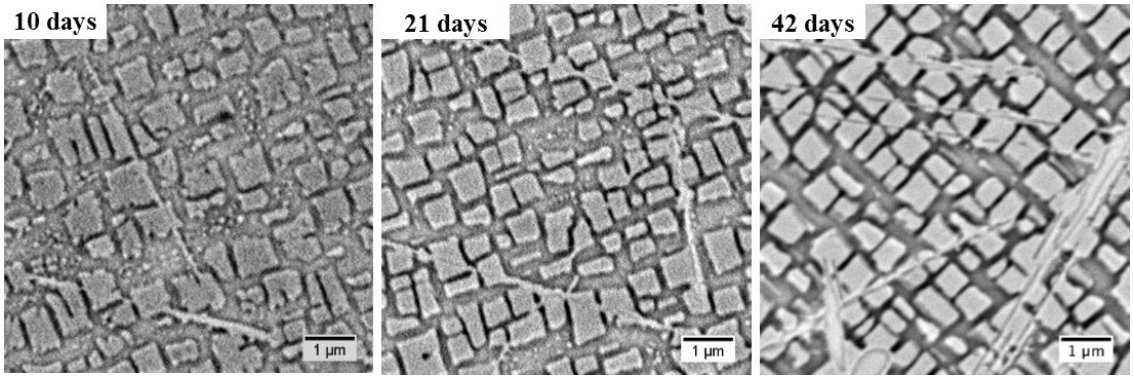

Figure 4.16: BSI micrographs of the alloy with 20at.% of Cr after oxidation between 10 and 42 days at 800℃.

4.7 EDX mapping and elements distribution on the cross sections

Detailed information on the structure of the oxide scales and the species present in the internal damage region was obtained through elemental EDX mapping of the samples oxidised for 42 days, with the exception of the alloy with 10 at.% Cr, which was examined using the sample oxidised for 21 days due to the spallation of the oxide, previously discussed. In line with the microstructural evolution of the oxide scales, Figure 4.10, the oxides formed on the alloys with 10 and 15 at.% Cr, Figures 4.17 and 4.18, showed similar distributions of elements within their oxide layers. The outermost layer consisted of a Ni and Co oxide, slightly enriched in W and had a columnar morphology. Immediately beneath the Ni and Co oxide, a second mixed oxide layer of Co and Cr could be identified. This layer contained regions of chromia, although these existed as dispersed particles, with no evidence of them forming a continuous layer. These two layers together constituted the majority of the measured oxidation damage. The third layer contained Al and Ti rich internal oxides that penetrated into the base material. The depth to which these oxides penetrated the substrate of the alloy with 15 at.% Cr was less than that in the alloy with 10 at.% Cr. Below the oxidised layers of the alloys with 10 and 15 at.% Cr, a region enriched in Ni and depleted in Cr was observed. The elemental distribution maps suggested that Mo was not incorporated in any of the outer oxide layers, although elevated concentrations were observed at the base of the Co and Cr mixed oxide layer. However, these features do not appear to be associated with appreciable concentrations

of O, which suggests that these may be intermetallic species.

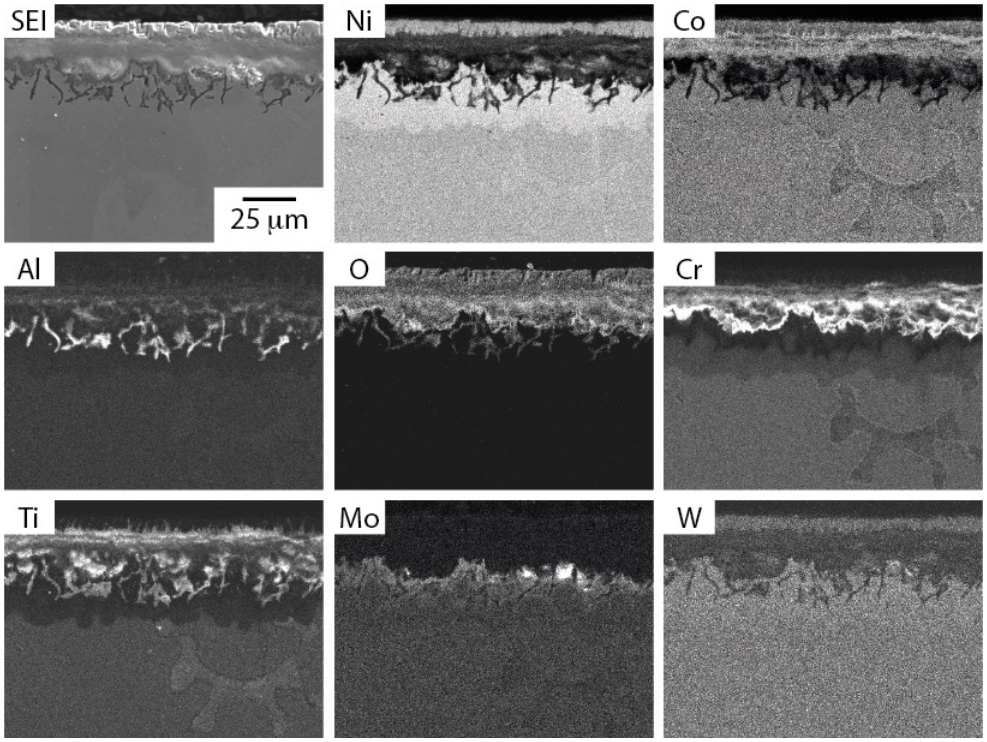

Figure 4.17: Elemental distribution maps of the alloy with 10 at.% Cr after oxidation for 21 days at 800℃.

Elemental distribution maps obtained from the alloys with 17.5 and 20 at.% Cr, Figures 4.19 and 4.20, revealed differences to those from the alloys with 10 and 15 at.% Cr. The outermost scale of the alloys with 17.5 and 20 at.% Cr consisted of a Ni, Co and Cr oxide, which was thinnest for the alloy with 20 at.% Cr. Beneath this oxide a continuous chromia scale was observed, ∼1–2 μm in thickness. The internal damage of the alloy with 17.5 at.% Cr comprised of Al and Ti rich oxides that penetrated into the substrate, accompanied by Ti nitrides, which were identified by regions of high Ti concentration and an absence of O. Regrettably, reliable measurements of N concentration were beyond the sensitivity of the SEM EDX system used. In contrast, alumina fingers were not observed in the alloy with 20 at.% Cr. Instead, a continuous thin alumina layer was observed that also contained elevated levels of Ti. Beneath the alumina layer, the EDX analysis revealed Ti without the presence of oxygen, again suggesting the formation of Ti nitrides, rather than titania at this depth. In both alloys, a distinct region depleted in Cr and enriched in Ni was observed below the internal damage layer, similar to that seen for the lower Cr containing alloys. Localised enrichment of both Mo and Cr can also be seen within the

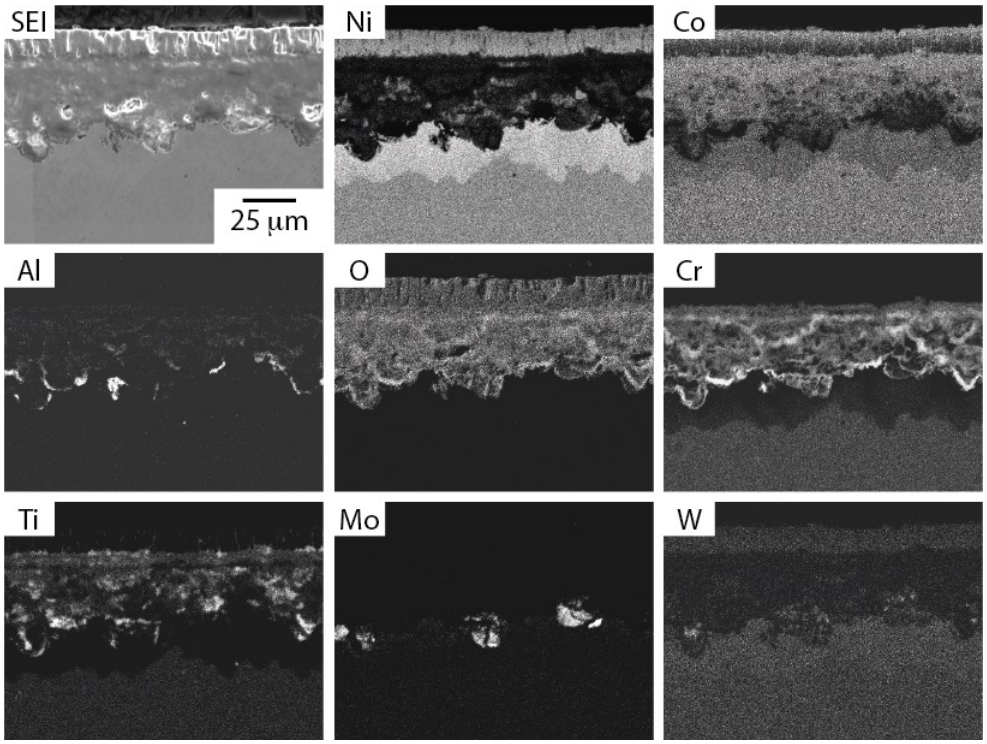

Figure 4.18: Elemental distribution maps of the alloy with 15 at.% Cr after oxidation for 42 days at 800℃.

substrate of the alloy with 20 at.% Cr. This is consistent with the formation of the sigma TCP phase, commonly reported in alloys of this type [13, 44, 45].

The oxide strata produced on the alloy with 25 at.% Cr, Figure 4.7, were markedly different than those seen on the other alloys investigated in this study. The outermost layer was comprised mainly of a Ni oxide with a columnar morphology, Figure 4.10e, although a small amount of Co was also detected in this layer. Evidence of a few isolated titanium oxides was also found intersecting the continuous outer Ni oxide layer. The second layer consisted of a mixed Co and Cr oxide, which also appeared to contain a dispersion of titanium oxide particles. Beneath this mixed oxide, a continuous chromia layer, $\sim$5 μm thick, was observed. A thin layer of alumina existed immediately below the chromia layer, similar to that observed within the oxide formed on the alloy with 20 at.% Cr. The internally damaged regions appeared to comprise a mixture of Ti nitrides and alumina, which penetrated into the substrate. Unlike previous alloys, the nitrides in the alloy with 25 at.% Cr formed as a band parallel to the exposed surface, rather than extending into the substrate. A region of Cr depletion and Ni enrichment was observed beneath the internally damaged region, consistent with the other alloys in this study. As

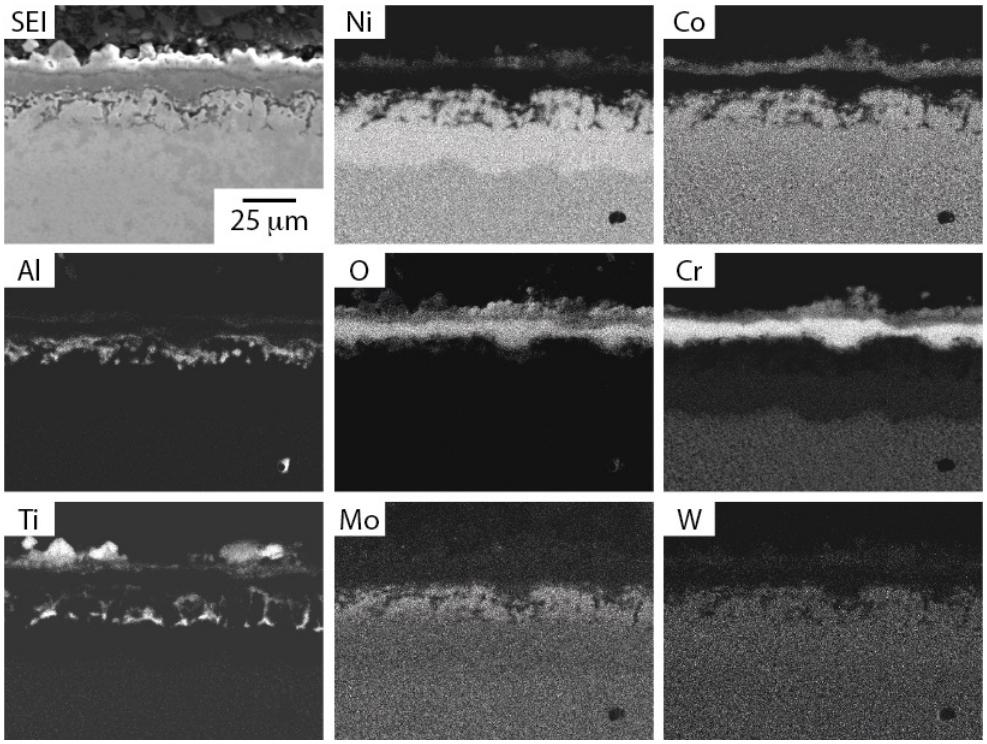

Figure 4.19: Elemental distribution maps of the alloy with 17.5 at.% Cr after oxidation for 42 days at 800℃.

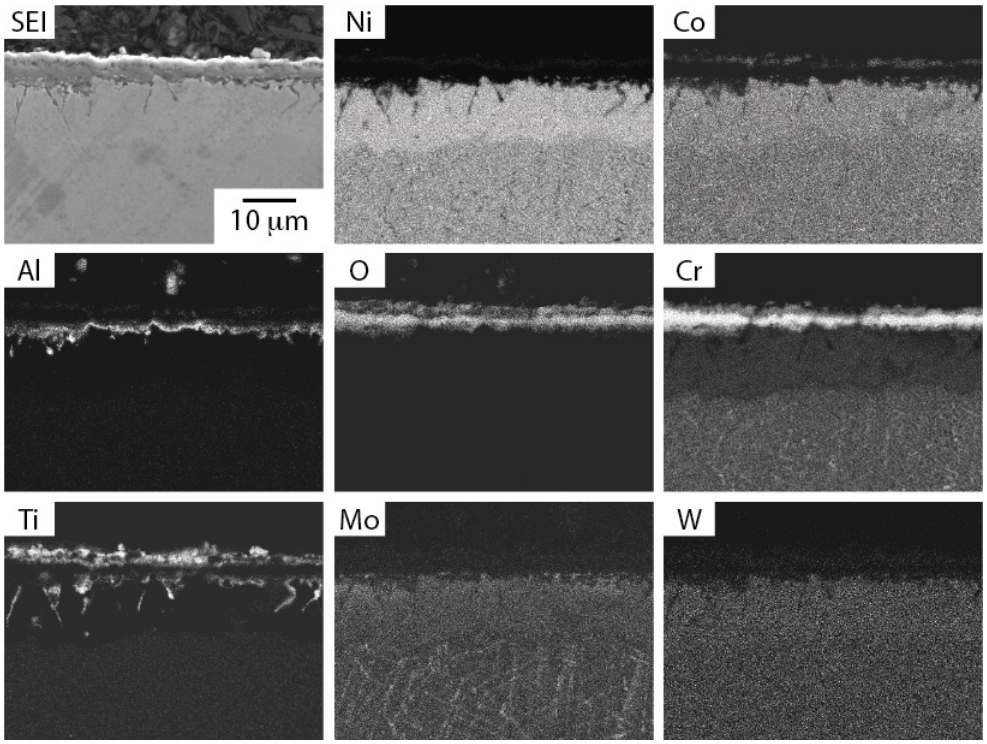

Figure 4.20: Elemental distribution maps of the alloy with and 20 at.% Cr after oxidation for 42 days at 800℃.

with the alloy with 20 at.% Cr, localised enrichment of both Mo and Cr was detected in the substrate, suggesting the presence of intermetallic phases.

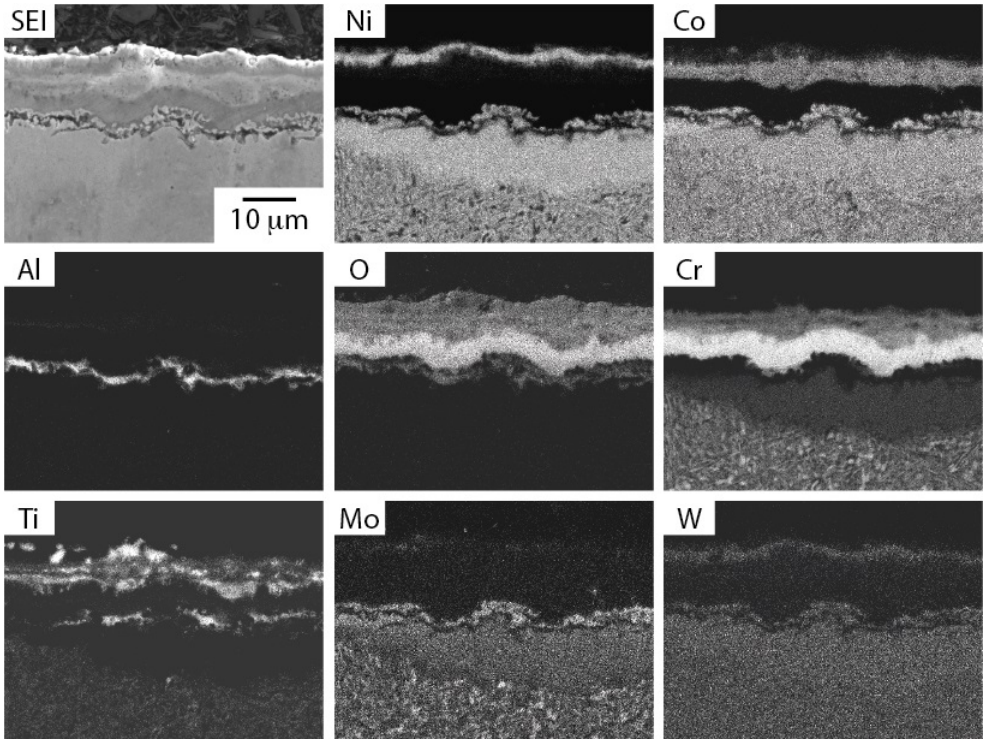

Figure 4.21: Elemental distribution maps of the alloy with 25 at.% Cr after oxidation for 42 days at 800℃.

4.8 Chromium depletion layer

In order to analyse in detail the depletion layer beneath the oxide scale, EDX linescans were performed on each alloy after oxidation for 42 days. As previously discussed, it should be noted that the measurements are referred to the sample oxidised for 21 for the alloy with 10 at.% of Cr days because of the complete spallation occurred for 42 days of exposure at 800℃. The alloy with 10 and 15 at.% of Cr, Figures 4.22 and 4.23 respectively, have shown similar compositional profiles. Both these alloys exhibited a Ni oxide enriched outermost layer, followed by a mixed oxide region where an alumina film can be distinguished. These results confirm what previously discussed in detail from the EDX mapping analysis. Furthermore, from the EDX linescans is possible to distinguish a pure Ni enriched region beneath the external oxide scale. The increase in this element is accompanied by a depletion of Cr, Co, Ti and, to a lesser extent, Al.

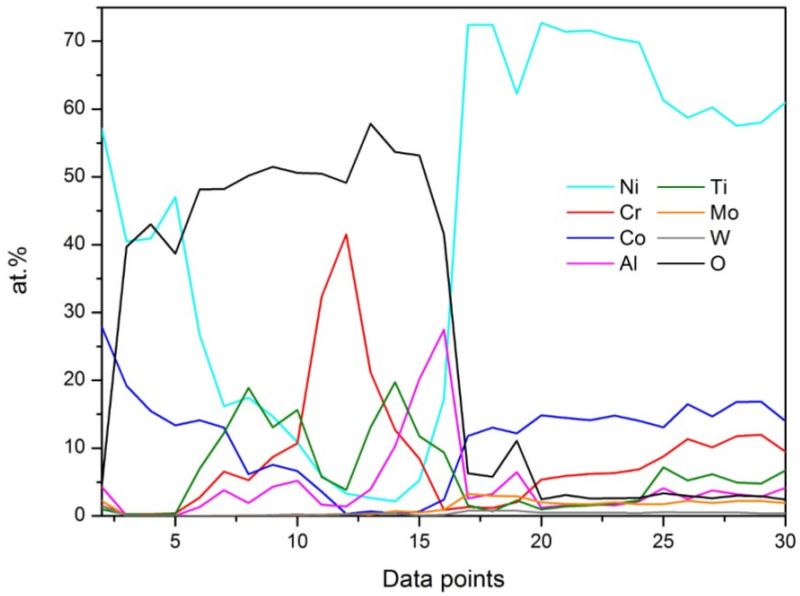

Figure 4.22: Elemental composition of the cross section of the alloy with 10 at.% of Cr after oxidation for 21 days at 800℃

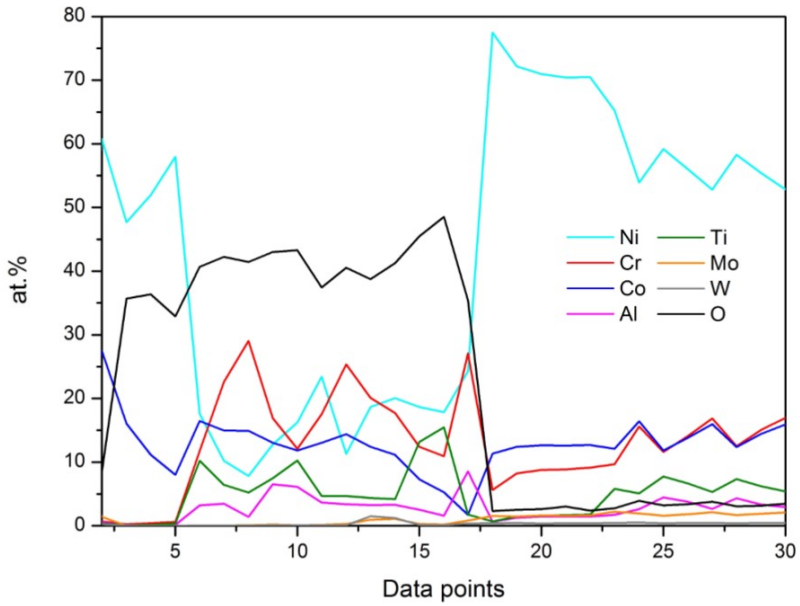

Figure 4.23: Elemental composition of the cross section of the alloy with 15 at.% of Cr after oxidation for 42 days at 800℃

The alloys with 17.5 and 20 at.% of Cr have shown similar profiles, Figures 4.24 and 4.25. For both these alloys the top layer was composed mostly of Cr oxide with traces of Co, Ti and Ni oxides dispersed in the external scale. Similarly, Al and Ti concentration peaks were observed beneath the external layer. Interestingly, no evidence of oxygen presence was detected in correspondence to these peaks suggesting that titanium and aluminium nitrides could have formed. Compared to the alloys with 10 and 15 at.% a less pronunced Cr depletion region was observed. Evidence of Al and Ti depletion was observed beneath the nitride peaks region for each composition whereas Co concentration resulted unvaried in the metallic substrate below the oxide scale.

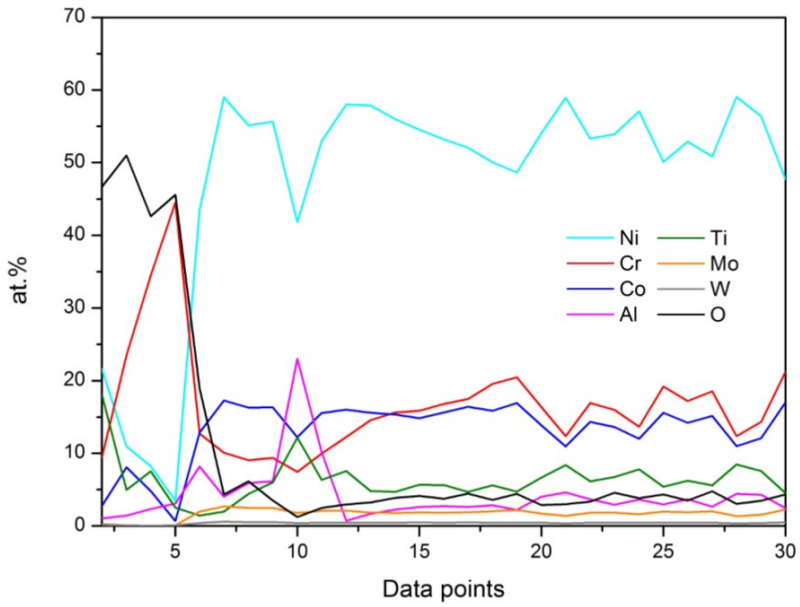

Figure 4.24: Elemental composition of the cross section of the alloy with 17.5 at.% of Cr after oxidation for 42 days at 800°C

A more complex compositional profile was exhibited by the alloy with 25 at.% of Cr, Figure 4.26. In line with what discussed in EDX mapping section, a top Ni oxide layer was detected followed by a Cr and Co mixed oxide and a pure chromia strata beneath. The internal damage region was composed by a Ni and Co oxide mixed film and an alumina enriched layer. For this composition, the Cr depletion layer corresponding to an enrichment in Ni is noted beneath the alumina fingers. As for the alloys with 17.5 and 20 at.% of Cr, the concentration of Co appeared constant in the substrate. Similarly, Al

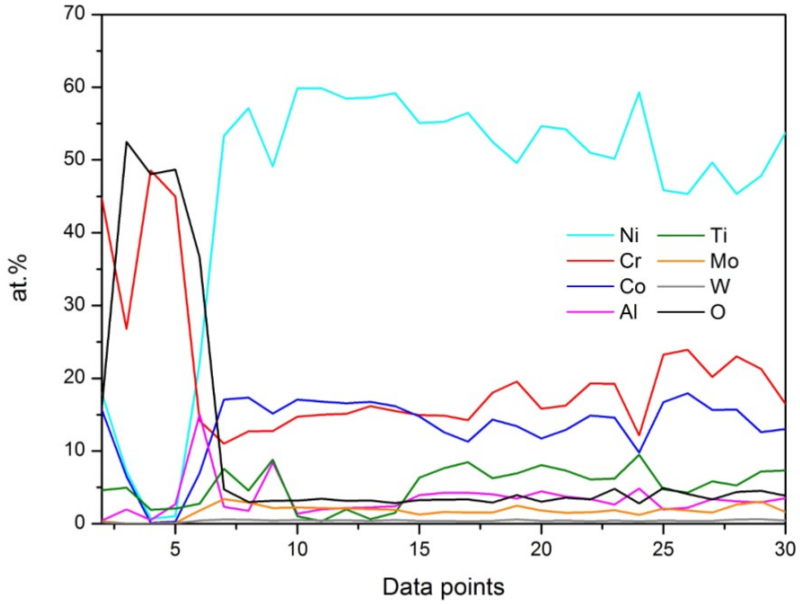

Figure 4.25: Elemental composition of the cross section of the alloy with 20 at.% of Cr after oxidation for 42 days at 800℃

and Ti have shown a less pronounced depletion in proximity to the external oxides.

BSI micrographs of the depletion layer in the metallic substrate were taken for the alloys with 20 and 25 at.% of Cr after oxidation for 42 days, Figure 4.27. A layer composed of pure metal with no presence of precipitated species was observed beneath the inetrnal damage region. Below this region, the substrate exhibited a structure composed of a γ matrix with γ' and TCP phases according with what previously observed in Figure 4.14. The edge between these regions appears composed by intermtallic grains, mostly γ' and TCP species for the alloys with 20 and 25 at.% of Cr respectively, that are partially dissolved in the Ni enriched region.

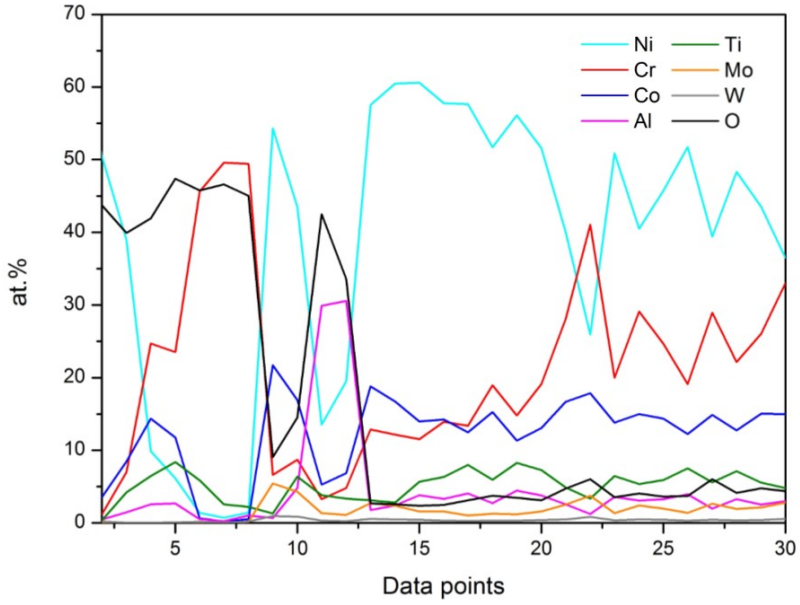

Figure 4.26: Elemental composition of the cross section of the alloy with 25 at.% of Cr after oxidation for 42 days at 800℃

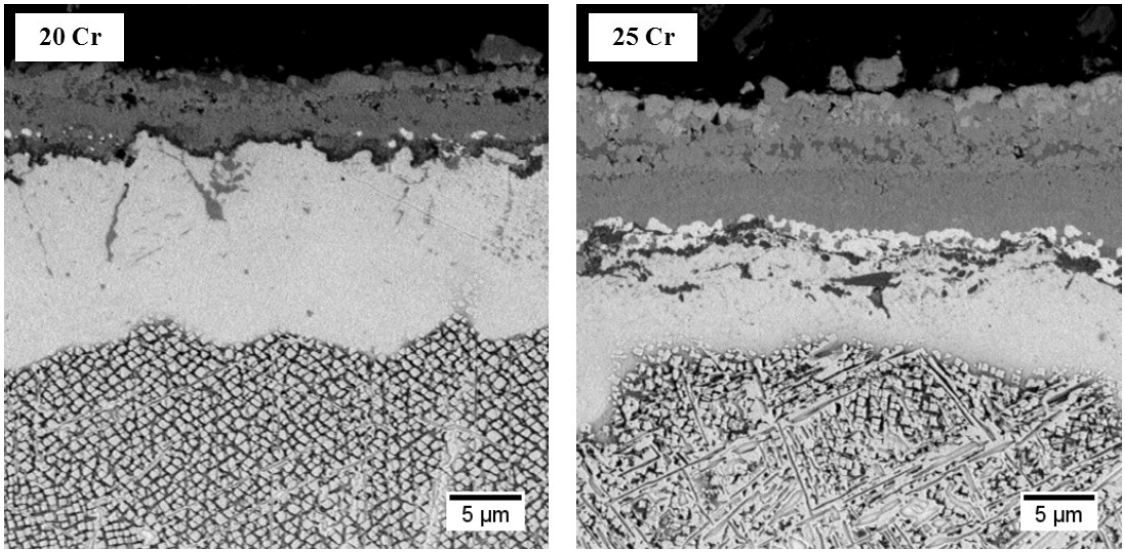

Figure 4.27: BSI micrographs of the cross section of the alloys with 20 and 25 at.% of Cr after oxidation for 42 days at 800℃.

Chapter 5

Discussion

5.1 External oxide scale and microstructural evolution

Since from the as heat treated sample characterization is evident that an excessive increase of the content of Cr lead to the formation of undesired intermetallic species formation. This is the case of the alloy with 25 at.% of Cr whose TCP rich microstructure caused an increase in the hardness of the material making it useless for aerospace applications. The different morphology and distribution of the secondary and tertiary γ' grains as well as the similar hardness values measured for the alloys with less than 25 at.% of Cr lead to think that the alloys with 17.5 and 20 at.% Cr have better mechanical properties compared to the alloys with 10 and 15 at.% of Cr. This is true for short exposure time at high temperature. However, for exposure times $\geq$10 days, intermetallic species were observed in the alloy with 20 at.% of Cr whereas the alloys with $\leq$17.5 at.% of Cr have not shown TCP precipitation in the entire experimental time considered for this study. This indicates that the best microstructural stability at high temperature for precipitation hardenend alloys is achieved with a content of Cr that must not be in excess. The alloy with 25 at.% of Cr showed an increase in the amount of intermetallic phase in the microstructure revealing a poor resistance to hot environments. From the comparison between the microstructures of the alloys as heat treated and after oxidation for 42 days it is possible to observe the almost total absence of tertiary γ' at the end of the experiment. This could be explained by the activation of coarsening and diffusion phenomena that are facilitated by high tem-

perture.

The evolution of the external oxide scales of the alloys suggest that there is little correlation with the oxidation resistance after 42 days of exposure at 800℃. It should be noted that the alloys with 10 and 15 at.% of Cr have shown large top scale grains that corresponds to the Ni/Co mixed columnar oxide. These materials were both subject to a deep internal oxidation and to spallation after long exposure time. Similarly, the alloy with 25 at.% of Cr exhibited a columnar top scale that had not prevent further oxidation of the metallic substrate although spallation was not observed for this composition. The alloys that have shown an external oxide scale composed of fine grains, 17.5 and 20 at.% of Cr, are those that have better resisted to oxidation after 42 days.

5.2 Mass gains per unit area

In this study, the oxide thickness, internal damage and mass gains per unit area were measured as a function of time. From these data it is possible to examine the correlations that exist between these quantities for the alloys studied. The thickness of the oxide scale and the depth of the internal damage are presented as a function of mass change per unit area in Figure 5.1. Despite the differences in the stoichiometries of the oxide species that may have formed, the external oxide scale thicknesses vary approximately linearly with the mass change per unit area. However, this is not the case for the depth of internal damage, which shows little correlation. This indicates that mass change per unit area alone is not sufficient to serve as a proxy for all aspects of oxidation damage in these alloys and that microstructural characterisation is also important. For example, the alloy with 17.5 at.% Cr exhibited the smallest mass gain and one of the thinnest oxide scales, but suffered extensive internal oxide penetration. Critically, the internal oxidation in this alloy was only evident after ∼10 days of exposure at the test temperature. This is well beyond the duration of conventional in-situ thermogravimetric analysis and indicates that care must be taken when assessing oxidation behaviour using short–duration exposures.

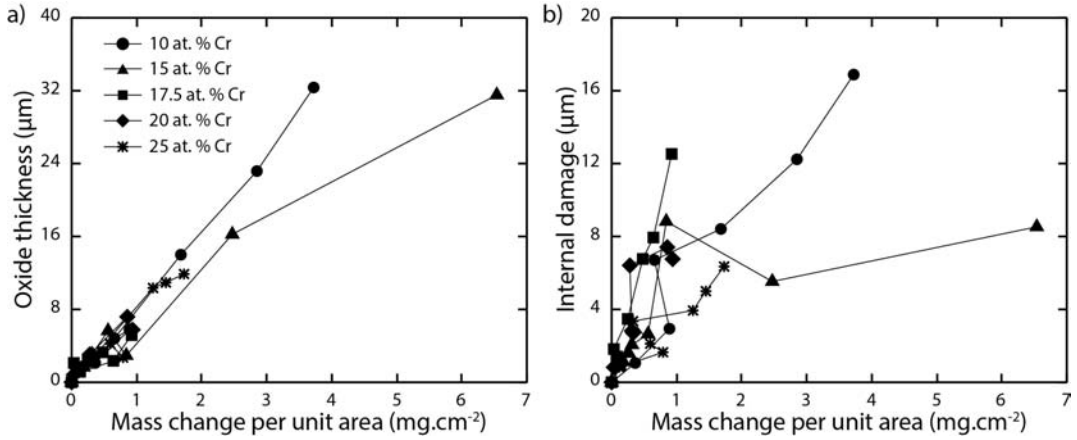

Figure 5.1: (a) The oxide scale thickness and (b) depth of internal damage as a function of mass change per unit area.

5.3 Classification of the alloys on the oxidation mechanism

The subdivision of oxidation mechanisms proposed by Giggins and Pettit [31] and Wallwork and Hed [32] can be used to describe the different oxidation behaviours exhibited by the five alloys investigated in this study. The alloys with 10 and 15 at.% Cr formed an external scale composed of Ni and Co oxide that is characteristic of Type I oxidation behaviour, with a discontinuous subscale of chromia and alumina fingers penetrating into the alloy. However, the alloys with 17.5 at.% Cr and above exhibit Type II oxidation behaviour, developing an external chromia scale accompanied by internal penetration of alumina into the substrate. It can therefore be seen that the transition between Type I and Type II oxidation behaviour lies between the alloys with 15 and 17.5 at.% Cr. An external Ni and Co oxide scale was observed on all the alloys showing Type II oxidation behaviour, but was considerably thicker on the alloy with 25 at.% Cr. Similarly, the thickness of the chromia layer was also greater in this alloy. These observations may be attributed to differences in the diffusional transport kinetics through the oxide layers in these alloys. Theories regarding ionic transport through oxide scales suggest that the incorporation of lower valence cations, such as Ni^{2+} in the present case, into a p-type metal-excess semiconductor oxide, such as chromia, would be expected to reduce the intrinsic defect concentration. This in turn reduces the rate of ionic transfer through the chromia layer and thereby also the rates at which both the chromia scale and the Ni and

Co over-scales can thicken. However, it is recognised that short-circuit diffusion through the oxide scale, vapourisation of chromia and diffusional supply of Cr from the substrate all complicate the oxidation kinetics of chromia forming alloys [46]. Previous studies of related, multi-component Ni-Cr containing alloys [36] have shown that minimum parabolic oxidation rates occur with concentrations of 15–20 wt.% Cr and approach the more rapid oxidation kinetics of pure chromium as the concentration is further increased. Therefore, the observation in the present work that the alloy with the highest Cr concentration does not exhibit the greatest oxidation resistance is in keeping with previous work and suggests that the oxidation kinetics of these precipitation hardened alloys behave in an analogous manner.

5.4 Internal damage

The evolution of the internal damage varies significantly between the five alloy compositions studied. The alloys with 10 and 15 at.% Cr showed deep internal oxidation of Al, Cr and Ti, leading to a large mixed oxide layer below the Ni and Co oxide, typical of Type I oxidation behaviour. The internal penetration of alumina fingers into the alloy with 17.5 at.% Cr was found to be very deep compared to the thickness of the external scale. The acicular morphology of the precipitates could be attributed to the disparity between the coarsening rate of the oxide particles and the speed of the reaction front into the substrate. This situation results in the preferential diffusion of O towards the tip of the oxide, promoting longitudinal growth over the nucleation of new particles [27, 26]. Alloys with higher Cr concentrations will have lower reaction front velocities, making the growth of acicular precipitates less likely. It should also be noted that the development of internally oxidised alumina may be influenced by the change in activity of Al associated with the differing concentrations of Cr. These effects can clearly be seen in the alloy with 25 at.% Cr, where a continuous film of alumina was observed beneath the external oxide scale. In contrast, long alumina fingers were found in the alloys with $\leq$ 17.5 at.% Cr. The alloy with 20 at.% Cr behaved in an intermediate manner as neither extensive acicular oxides nor a continuous alumina layer were observed, instead a band of Al–rich globular particles was seen beneath the chromia scale.

The presence of different Ti rich species in the five alloys studied can also be correlated

to the content of Cr in the alloy. The alloys with 10 and 15 at.% Cr showed extensive formation of titanium oxide, alumina fingers and chromia particles within the externally oxidised regions. This can be attributed to the unprotective nature of the outermost Ni and Co oxide, which did not sufficiently inhibit the ingress of O through the external scale. In contrast, the alloys with Cr concentrations $\geq$ 17.5 at.% showed only limited evidence of Ti oxides beneath the chromia scale as the chromia scale in these alloys reduced the transport of O through the oxide. This resulted in the preferential formation of Al oxides, which are known to form at lower O partial pressures than Ti oxides. However, in the oxidised alloys, regions rich in Ti were detected without the presence of oxygen and these were believed to be Ti nitrides. In a reversal of the behaviour with O, the Ti nitrides form preferentially to Al nitrides, due to its lower relative Gibbs energy of formation [26].

5.5 Chromium depletion layer

Beneath the internally oxidised layer, a region enriched in Ni and depleted in Cr can be observed, consistent with previous studies of the oxidation characteristics of nickel-base superalloys [47]. In the present case, the enrichment of Ni arises through the diffusion of Cr, Al and Ti to form different oxide species, depleting the substrate in these elements. The consumption of Al from the bulk, to form alumina, also resulted in the dissolution of the γ' phase in the vicinity of the oxide scale. Similarly, in the two high Cr containing alloys, the Cr and Mo rich intermetallic phases act as reservoirs for Cr. Hence, a second transition region exists beneath the γ' free zone in these alloys, which consists of only the γ and γ' phases, without the Cr–rich intermetallic phase that can be observed deeper in the substrate.

Chapter 6

Conclusions

The oxidation characteristics of a series of nickel-base superalloys with Cr contents of 10–25 at.% were studied using isothermal furnace exposures at 800℃for between 1 and 42 days. The alloys with 10 and 15 at.% Cr demonstrated Type I oxidation behaviour, forming continuous Ni and Co oxide layers and extensive internal oxidation. These alloys exhibited large mass gains per unit area and the oxides were prone to spallation, within the time-scale studied. The alloys with $\geq$ 17.5 at.% Cr produced continuous chromia scales, consistent with Type II oxidation behaviour. Whilst both the alloys containing 17.5 and 20 at.% Cr possessed thin chromia scales and the lowest mass gains of the alloys studied, more extensive internal oxidation was observed beneath the oxide on the alloy with 17.5 at.% Cr. The alloy with 25 at.% Cr produced a thicker oxide scale, accompanied by a larger mass gain per unit area than the alloys with 17.5 and 20 at.% Cr. This was associated with increased diffusional transport through the oxides similar to that seen in Ni–Cr binary alloys. From the data acquired in this study, a strong correlation was identified between the thickness of the oxide scale and the mass gains per unit area. In contrast, little to no correlation was seen with the depth of internal damage. These observations indicate that thermogravimetric analysis alone does not provide an effective measure of all oxidation damage in alloys of this type and that care should be taken to ensure that exposure times are sufficient to allow all oxidation related microstructural developments to take place.

In order to better understand the oxidation mechanism, future activities will focus on the characterization of the oxide scales developed in the alloys studied for this work.

Useful information on the oxides that have formed could be obtained by X-ray diffraction analysis.

Future research on this field will also include a more in-depth analysis of the TCP phase precipitation and how this affects the mechanical properties. In particular, a comparison between the alloys with 17.5 and 20 at.% of Cr in terms of yield properties, fatigue and creep resistance could be of great interest for the design of new gas turbine disc superalloys with better performances. A more accurate characterisation of the TCP phases precipitated after long exposure time is essential to understand the relation between isothermal oxidation and mechanical properties in these alloys.

Bibliography

[1] R. Schafrik and R.Sprague, The saga of gas turbine materials, *Advanced Materials and Processes*, vol. 162, 2004.

[2] R. C. Reed, *The Superalloys Fundamentals and Aplications*, 2006.

[3] M. McLean, *Directionally Solidified Materials for High Temperature Service*, 1983.

[4] J. H. Perepezko, The Hotter the Engine, the Better, *Science*, vol. 326, p1068–1069, 2009.

[5] H. J. Frost and M. F. Ashby, *Deformation-Mechanism Maps: The Plasticity and Creep of Metals and Ceramics*, 1982.

[6] A. M. Brown and M. F. Ashby, Correlations for diffusion coefficients, *Acta Metallurgica*, Vol.28, p1085-1101, 1980.

[7] M. Durand-Charre, *The Microstructure of Superalloys*, 1997.

[8] Alloy Phase Diagrams, *ASM International*, Vol.3, p49, 1992.

[9] S. Ochiai, Y. Oya and T. Suzuki, Alloying behaviour of Ni_3Al, *Acta Metallurgica*, Vol.32, p289-298, 1984.

[10] F. J. Bremer, M. Beyss and H. Wenzl, The order-disorder transition of the intermetallic phase Ni_3Al, *Physica Status Solidi*, Vol.110A, p77-82, 1988.

[11] S. V. Prikhodko and A. J. Ardell, Coarsening of gamma prime in Ni-Al alloys aged under uniaxial compression: III. Characterisation of the morphology, *Acta Materialia*, Vol.51, p5021-5036, 2003.

[12] R. A. Ricks, A. J. Porter and R. C. Ecob, The growth of gamma prime precipitates in nickel-base superalloys, *Acta Metallurgica*, Vol.31, p43-53, 1983.

[13] R. C. Reed, M. P. Jackson and Y. S. Na, Characterisation and modelling of the precipitation of the sigma phase in Udimet 720 and Udimet 720Li, *Metallurgical and Materials Transactions*, Vol.30A, p521-533, 1999.

[14] A. K. Sinha, Topologically close-packed structures of transition metal alloys, *Progress in Metal Science*, Vol.15, p79-185, 1972.

[15] J. Jones and D. J. C. Mackay, Neural network modelling of the mechanical properties of nickel base superalloys, in R. D. Kissinger, D. J. Deye, D. L. Anton *et al.*, *Superalloys 1996* (Warrendale, PA: The Minerals, Metals and Materials Society (TMS)), p417-424, 1996 .

[16] M. P. Jackson and R. C. Reed, Heat treatment of Udimet 720Li: the effect of microstructure on properties, *Materials Science and Engineering*, Vol.259A, p85-97, 1999.

[17] J. C. Williams and E. A. Starke, Progress in structural materials for aerospace systems, *Acta Materialia*, Vol.51, p5775-5799, 2003.

[18] K. R. Bain, M. L. Gambone, J. M. Hyzak and M. C. Thomas, Development of damage tolerant microstructures in Udimet 720, in S. Reichman, D. N. Duhl, G. Maurer, S. Antolovich and C. Lund, *Superalloys 1988* (Warrendale, PA: The Metallurgical Society), p13-22, 1988.

[19] D. P. Mourer and J. L. Williams, Dual heat treatment process development for advanced disk applications, in K. A. Green, T. M. Pollock, H. Harada *et al.*, *Superalloys 2004* (Warrendale, PA: The Minerals, Metals and Materials Society (TMS)), p401-408, 2004.

[20] F.E. Sczerzenie and G.E. Maurer, Development of Udimet 720 for High Strength Disk Applications, *TMS Superallovs 1984*, p573–582, 1984.

[21] D.J. Bryant and G. McIntosh, The Manufacture and Evaluation of a Large Turbine Disc in Cast and Wrought alloy 720Li, in R.D. Kissinger, D. J. Deye, D. L. Anton,

A.D. Cetel, M. V. Nathal, T. M. Pollock, and D. A. Woodford, *Superalloys 1996* (TMS, Warrendale, PA), pp. 713-22, 1996.

[22] D. Furrer and H. Fecht, Ni-Based Superalloys for Turbine Discs, *The Journal of The Minerals, Metals & Materials Society (TMS)*, Vol.51, p14-17, 1999.

[23] P. W. Keefe, S. O. Mancuso, and G. E. Maurer, Effects of Heat Treatment and Chemistry on the Long-Term Phase Stability of a High Strength Nickel-Based Superalloy, in S.D. Antolovich, R. W. Stusrud, R. A. Mackay, D. L. Anton, T. Khan, R. D. Kissinger, and D. L. Klarstrom, *Superalloys 1992* (TMS, Warrendale, PA), pp. 487-96, 1992.

[24] T. J. Garosshen, T. D. Tillman and G. P. McCarthy, Effects of B, C and Zr on the structure and properties of a P/M nickel-base superalloy, *Metallurgical Transactions*, Vol.18A, 69-77, 1987.

[25] N. Birks, G. H. Meier and F. S. Pettit, *Introduction to the High Temperature Oxidaiton of Metals (Second edition)*, 2006.

[26] D. L. Douglass, A critique of internal oxidation in alloys during the post-Wagner era, *Oxidation of metals*, vol.44, p81–111, 1995.

[27] J. Megusar and G. H. Meier, Internal oxidation of dilute Co-Ti alloys, *Metallurgical and Materials Transactions*, vol.7A, p1133–1140, 1976.

[28] G. C. Wood and B. Chattopadhyay, Transient Oxidation of Ni-base alloys, *Corrosion Science*, Vol.10, p471-480, 1970.

[29] T. Hodgkiess, G. C. Wood, D. P. Whittle and B. D. Bastow, Compositional Changes in the Underlying Alloy Produced by the Oxidation of Ni-Cr Alloys, *Oxidation of Metals*, Vol.12, p439-449, 1978.

[30] F. S. Pettit, *Transactions of the Metallurgical Society of AIME*, Vol.239, p1296, 1967.

[31] C. S. Giggins and F. S. Pettit, Oxidation of Ni-Cr-Al alloys between 1000℃and 1200℃, *Journal of the Electrochemical Society*, vol.118, p1782–1790, 1971.

[32] G.R. Wallwork and A.Z. Hed, Some limiting factors in the use of alloys at high temperatures, *Oxidation of Metals*, vol.3, p171–184, 1971.

[33] G.R. Wallwork, The oxidation of alloys, *Reports on Progress in Physics*, vol.39, p401–485, 1976.

[34] B. H. Kear, F. S. Pettit, D. E. Fornwalt and L. P. Lemaire, On the Transient Oxidation of a Ni-15Cr-6Al Alloy, *Oxidation of Metals*, Vol.3, p557-569, 1971.

[35] F. Hamdani, H. Abe, B. Ter-Ovanessian, B. Normand and Y. Watanabe, Effect of chromium content on the oxidation behavior of Ni-Cr model alloys in superheated steam, *Metallurgical and Materials Transaction A*, vol.46, p2285–2293, 2015.

[36] C. L. Angerman, Long-term oxidation of superalloys, *Oxidation of Metals*, vol.5, p149–167, 1972.

[37] G. C. Wood, *Oxidation of Metals and Alloys*, ASM, ch.11, 1971.

[38] J. R. Stephens and R.L. Dreshfield, Understanding the roles of the strategic element cobalt in nickel base superalloys, *Technical Memorandum 83475*, NASA Lewis Research Center, 1983.

[39] J. H. Chen, P. M. Rogers and J. A. Little, Oxidation behavior of several chromia-forming commercial nickel-base superalloys, *Oxidation of Metals*, vol.47, p381–410, 1997.

[40] D. Kim, C. Jang, and W. Ryu, Oxidation characteristics and oxide layer evolution of Alloy 617 and Haynes 230 at 900℃and 1100℃, *Oxidation of Metals*, vol.71, p271–293, 2009.

[41] S. Cruchley, H. E. Evans, M. P. Taylor, M.C. Hardy and S. Stekovic, Chromia layer growth on a Ni-based superalloy: Sub-parabolic kinetics and the role of titanium, *Corrosion Science*, vol.75, p58–66, 2013.

[42] H. Nagai and M. Obakayashi, Deleterious effect of Ti addition on the oxidation resistance of Ni-20Cr alloy, *Transactions of the Japan Institute of Metals*, vol.22, p691–698, 1981.

[43] R. Couturier, H. Burlet, S. Terzi, S. Dubiez, L. Guetaz and G. Raisson, Process development and mechanical properties of alloy U720Li for high temperature turbine disks, *Superalloys 2004* (Warrendale, PA: The Minerals, Metals and Materials Society (TMS)), p351–359, 2004.

[44] A. Oradei-Basile and J. F. Radavich, A current T-T-T diagram for wrought alloy 718, *Superalloys 718, 625 and Various Derivatives*, p325–33, 1991.

[45] R. J. Mitchell, C. M. F. Rae and S. Tin, Grain boundary transformations during isothermal exposure of powder metallurgy nickel base superalloys for turbine disc applications, *Materials Science and Technology*, vol.21, p125–132, 2005.

[46] G. M. Ecer and G. H. Meier, Oxidation of high-chromium Ni-Cr alloys, *Oxidation of Metals*, vol.13, p119–158, 1979.

[47] G. C. Wood and T. Hodgkiess, Characteristic scales on pure nickel-chromium alloys at 800℃-1200℃, *Journal of the Electrochemical Society*, vol.113, p.319–327, 1966.